U.S. Department of Transportation
Federal Highway Administration

Errata

Date:	April 17, 2019
Issuing Office:	Federal Highway Administration—Office of Research, Development, and Technology
Address:	Turner-Fairbank Highway Research Center, 6300 Georgetown Pike, McLean, VA 22101
Name of Document:	Analysis Procedures for Evaluating Superheavy Load Movement on Flexible Pavements, Volume II: Appendix A, Experimental Program
FHWA Publication No.:	FHWA-HRT-18-050

The following changes were made to the document after publication on the Federal Highway Administration website:

Location	Incorrect Values	Corrected Values
TECHNICAL REPORT DOCUMENTATION PAGE, Box 15	Nadarajah Sivaneswaran (HRDI-20; ORCID: 0000-0002-3525-9165), Office of Infrastructure Research and Development, Turner-Fairbank Highway Research Center, served as the Contracting Officer's Representative.	Nadarajah Sivaneswaran (HRDI-20; ORCID: 0000-0003-0287-664X), Office of Infrastructure Research and Development, Turner-Fairbank Highway Research Center, served as the Contracting Officer's Representative.

Analysis Procedures for Evaluating Superheavy Load Movement on Flexible Pavements, Volume II: Appendix A, Experimental Program

PUBLICATION NO. FHWA-HRT-18-050

NOVEMBER 2018

U.S. Department of Transportation
Federal Highway Administration

Research, Development, and Technology
Turner-Fairbank Highway Research Center
6300 Georgetown Pike
McLean, VA 22101-2296

FOREWORD

The movement of superheavy loads (SHLs) on the Nation's highways is an increasingly common, vital economic necessity for many important industries, such as chemical, oil, electrical, and defense. Many superheavy components are extremely large and heavy (gross vehicle weights in excess of a few million pounds), and they often require specialized trailers and hauling units. At times, SHL vehicles have been assembled to suit the load being transported, and therefore, the axle configurations have not been standard or consistent. Accommodating SHL movements without undue damage to highway infrastructure requires the determination of whether the pavement is structurally adequate to sustain the SHL movement and protect any underground utilities. Such determination involves analyzing the likelihood of instantaneous or rapid load-induced shear failure of the pavement structure.

The goal of this project was to develop a comprehensive analysis process for evaluating SHL movement on flexible pavements. As part of this project, a comprehensive mechanistic-based analysis approach consisting of several analysis procedures was developed for flexible pavement structures and documented in a 10-volume series of Federal Highway Administration reports—a final report and 9 appendices.[1–9] This is *Analysis Procedures for Evaluating Superheavy Load Movement on Flexible Pavements, Volume II: Appendix A, Experimental Program*, and it details the experimental program that was undertaken as a part of the development of a comprehensive analysis process for evaluating SHL movement on flexible pavements. This report is intended for use by highway agency pavement engineers responsible for assessing the structural adequacy of pavements in the proposed route and identifying mitigation strategies, where warranted, in support of the agency's response to SHL-movement permit requests.

Cheryl Allen Richter, Ph.D., P.E.
Director, Office of Infrastructure
Research and Development

TECHNICAL REPORT DOCUMENTATION PAGE

1. Report No. FHWA-HRT-18-050	2. Government Accession No.	3. Recipient's Catalog No.
4. Title and Subtitle Analysis Procedures for Evaluating Superheavy Load Movement on Flexible Pavements, Volume II: Appendix A, Experimental Program		5. Report Date November 2018 6. Performing Organization Code
7. Author(s) Mohamed Nimeri (ORCID: 0000-0002-3328-4367), Hadi Nabizadeh (ORCID: 0000-0001-8215-1299), Elie Y. Hajj (ORCID: 0000-0001-8568-6360), Raj V. Siddharthan (ORCID: 0000-0002-3847-7934), Sherif Elfass (ORCID: 0000-0003-3401-6513), and Murugaiyah Piratheepan (ORCID: 0000-0002-3302-4856)		8. Performing Organization Report No. WRSC-UNR-201710-01A
9. Performing Organization Name and Address Department of Civil and Environmental Engineering University of Nevada 1664 North Virginia Street Reno, NV 89557		10. Work Unit No. 11. Contract or Grant No. DTFH61-13-C-00014
12. Sponsoring Agency Name and Address Office of Infrastructure Research and Development Federal Highway Administration Turner-Fairbank Highway Research Center 6300 Georgetown Pike McLean, VA 22101		13. Type of Report and Period Covered Final Report; August 2013–July 2018 14. Sponsoring Agency Code HRDI-20
15. Supplementary Notes Nadarajah Sivaneswaran (HRDI-20; ORCID: 0000-0003-0287-664X*), Office of Infrastructure Research and Development, Turner-Fairbank Highway Research Center, served as the Contracting Officer's Representative.		
16. Abstract The movement of superheavy loads (SHLs) has become more common over the years since it is a vital necessity for many important industries, such as chemical, oil, electrical, and defense. SHL hauling units are much larger in size and weight compared to standard trucks. SHL vehicles' gross vehicle weights may be in excess of a few million pounds, so they often require specialized trailers and components with nonstandard spacing between tires and axles. Accommodating SHL movements requires the determination of whether the pavement is structurally adequate and involves the analysis of the likelihood of instantaneous or rapid load-induced shear failure. As part of the Federal Highway Administration project, Analysis Procedures for Evaluating Superheavy Load Movement on Flexible Pavements, a comprehensive experimental program was designed and conducted to verify and calibrate multiple theoretical approaches for the SHL analysis methodology. This experimental program included five different large-scale experiments with different objectives and characteristics using a large-scale box. The first two experiments consisted of a subgrade (SG) layer (experiment number (No.) 1) and an SG with a crushed-aggregate base layer on top (experiment No. 2). The subsequent three experiments consisted of a full pavement structure (experiment No. 3), a full pavement structure with a sloped shoulder (experiment No. 4), and a full pavement structure with a flexible and a rigid buried utility embedded in the SG layer (experiment No. 5). This report details each experiment's objectives, materials characterization, and construction techniques. It also presents the experimental measurements.		
17. Key Words Flexible pavement, superheavy load, large-scale box, instrumentation, dynamic loading	18. Distribution Statement No restrictions. This document is available to the public through the National Technical Information Service, Springfield, VA 22161. http://www.ntis.gov	

19. Security Classif. (of this report) Unclassified	20. Security Classif. (of this page) Unclassified	21. No. of Pages 110	22. Price N/A

Form DOT F 1700.7 (8-72) Reproduction of completed page authorized.

*Revised 4/17/19

SI* (MODERN METRIC) CONVERSION FACTORS

APPROXIMATE CONVERSIONS TO SI UNITS

Symbol	When You Know	Multiply By	To Find	Symbol
		LENGTH		
in	inches	25.4	millimeters	mm
ft	feet	0.305	meters	m
yd	yards	0.914	meters	m
mi	miles	1.61	kilometers	km
		AREA		
in^2	square inches	645.2	square millimeters	mm^2
ft^2	square feet	0.093	square meters	m^2
yd^2	square yard	0.836	square meters	m^2
ac	acres	0.405	hectares	ha
mi^2	square miles	2.59	square kilometers	km^2
		VOLUME		
fl oz	fluid ounces	29.57	milliliters	mL
gal	gallons	3.785	liters	L
ft^3	cubic feet	0.028	cubic meters	m^3
yd^3	cubic yards	0.765	cubic meters	m^3
		NOTE: volumes greater than 1000 L shall be shown in m^3		
		MASS		
oz	ounces	28.35	grams	g
lb	pounds	0.454	kilograms	kg
T	short tons (2000 lb)	0.907	megagrams (or "metric ton")	Mg (or "t")
		TEMPERATURE (exact degrees)		
^oF	Fahrenheit	5 (F-32)/9 or (F-32)/1.8	Celsius	^oC
		ILLUMINATION		
fc	foot-candles	10.76	lux	lx
fl	foot-Lamberts	3.426	$candela/m^2$	cd/m^2
		FORCE and PRESSURE or STRESS		
lbf	poundforce	4.45	newtons	N
lbf/in^2	poundforce per square inch	6.89	kilopascals	kPa

APPROXIMATE CONVERSIONS FROM SI UNITS

Symbol	When You Know	Multiply By	To Find	Symbol
		LENGTH		
mm	millimeters	0.039	inches	in
m	meters	3.28	feet	ft
m	meters	1.09	yards	yd
km	kilometers	0.621	miles	mi
		AREA		
mm^2	square millimeters	0.0016	square inches	in^2
m^2	square meters	10.764	square feet	ft^2
m^2	square meters	1.195	square yards	yd^2
ha	hectares	2.47	acres	ac
km^2	square kilometers	0.386	square miles	mi^2
		VOLUME		
mL	milliliters	0.034	fluid ounces	fl oz
L	liters	0.264	gallons	gal
m^3	cubic meters	35.314	cubic feet	ft^3
m^3	cubic meters	1.307	cubic yards	yd^3
		MASS		
g	grams	0.035	ounces	oz
kg	kilograms	2.202	pounds	lb
Mg (or "t")	megagrams (or "metric ton")	1.103	short tons (2000 lb)	T
		TEMPERATURE (exact degrees)		
^oC	Celsius	1.8C+32	Fahrenheit	^oF
		ILLUMINATION		
lx	lux	0.0929	foot-candles	fc
cd/m^2	$candela/m^2$	0.2919	foot-Lamberts	fl
		FORCE and PRESSURE or STRESS		
N	newtons	0.225	poundforce	lbf
kPa	kilopascals	0.145	poundforce per square inch	lbf/in^2

ANALYSIS PROCEDURES FOR EVALUATING SUPERHEAVY LOAD MOVEMENT ON FLEXIBLE PAVEMENTS PROJECT REPORT SERIES

This volume is the second of 10 volumes in this research report series. Volume I is the final report, and Volume II through Volume X consist of Appendix A through Appendix I. Any reference to a volume in this series will be referenced in the text as "Volume II: Appendix A," "Volume III: Appendix B," and so forth. The following list contains the volumes:

Volume	Title	Report Number
I	Analysis Procedures for Evaluating Superheavy Load Movement on Flexible Pavements, Volume I: Final Report	FHWA-HRT-18-049
II	Analysis Procedures for Evaluating Superheavy Load Movement on Flexible Pavements, Volume II: Appendix A, Experimental Program	FHWA-HRT-18-050
III	Analysis Procedures for Evaluating Superheavy Load Movement on Flexible Pavements, Volume III: Appendix B, Superheavy Load Configurations and Nucleus of Analysis Vehicle	FHWA-HRT-18-051
IV	Analysis Procedures for Evaluating Superheavy Load Movement on Flexible Pavements, Volume IV: Appendix C, Material Characterization for Superheavy Load Movement Analysis	FHWA-HRT-18-052
V	Analysis Procedures for Evaluating Superheavy Load Movement on Flexible Pavements, Volume V: Appendix D, Estimation of Subgrade Shear Strength Parameters Using Falling Weight Deflectometer	FHWA-HRT-18-053
VI	Analysis Procedures for Evaluating Superheavy Load Movement on Flexible Pavements, Volume VI: Appendix E, Ultimate and Service Limit Analyses	FHWA-HRT-18-054
VII	Analysis Procedures for Evaluating Superheavy Load Movement on Flexible Pavements, Volume VII: Appendix F, Failure Analysis of Sloped Pavement Shoulders	FHWA-HRT-18-055
VIII	Analysis Procedures for Evaluating Superheavy Load Movement on Flexible Pavements, Volume VIII: Appendix G, Risk Analysis of Buried Utilities Under Superheavy Load Vehicle Movements	FHWA-HRT-18-056
IX	Analysis Procedures for Evaluating Superheavy Load Movement on Flexible Pavements, Volume IX: Appendix H, Analysis of Cost Allocation Associated with Pavement Damage Under a Superheavy Load Vehicle Movement	FHWA-HRT-18-057
X	Analysis Procedures for Evaluating Superheavy Load Movement on Flexible Pavements, Volume X: Appendix I, Analysis Package for Superheavy Load Vehicle Movement on Flexible Pavement (SuperPACK)	FHWA-HRT-18-058

TABLE OF CONTENTS

LIST OF FIGURES

LIST OF TABLES

LIST OF ACRONYMS AND SYMBOLS

Abbreviations and Acronyms

AASHTO	American Association of State Highway and Transportation Officials
AC	asphalt concrete
ACC	accelerometer
CAB	crushed aggregate base
DCP	Dynamic Cone Penetrometer
FHWA	Federal Highway Administration
FWD	falling weight deflectometer
GI	group index
HMA	hot-mix asphalt
LVDT	linear variable differential transformer
NI	National Instruments™
No.	number
PVC	polyvinyl chloride
SCC	self-consolidating concrete
SG	subgrade
SHL	superheavy load
TEPC	total earth pressure cell

Symbols

c	cohesion
K	regression constant of resilient modulus model
m	deviator stress exponent
M_R	resilient modulus
n	bulk stress exponent
P_{200}	percentage passing through the No. 200 sieve
$P_{(Max)Dyn}$	maximum applied dynamic load
PI	plasticity index
W_{opt}	optimum moisture content
γ_{dmax}	maximum dry density
ε_a	axial strain
θ	bulk stress
σ_d	deviator stress
σ_{df}	deviator stress at failure
σ_f	normal stress at failure
τ_f	shear strength at failure
ϕ	angle of internal friction

CHAPTER 1. INTRODUCTION

As part of the Federal Highway Administration (FHWA) project, Analysis Procedures for Evaluating Superheavy Load Movement on Flexible Pavements, a comprehensive experimental program was carried out to verify and calibrate multiple theoretical approaches. This program utilized a large-scale pavement/soil-testing facility (a large-scale box). A total of five large-scale-box experiments were performed, and specific characteristics of the experiments are presented in table 1. All experiments had, whenever applicable, the same layer thicknesses for asphalt concrete (AC), crushed aggregate base (CAB), and subgrade (SG). Each experiment's objectives, materials characterization, and construction techniques are discussed in this report.

Table 1. Large-scale-box experiments.

Experiment No.	Description	Loading Protocol
1	• SG only (no AC or CAB). • Apply loads on top of SG.	• Apply dynamic loads of different amplitudes using 11.9-inch circular flexible plate, simulating the FWD loading duration for low number of cycles. • Apply increasing static load until failure using 11.9-inch circular steel plate.
2	• Unbound materials only (CAB and SG). • Apply loads on top of CAB.	• Apply dynamic loads of different amplitudes using 11.9-inch circular flexible plate, simulating the FWD loading duration for low number of cycles. • Apply increasing static load until failure using 11.9-inch circular steel plate.
3	• Control section (full pavement structure: AC, CAB, and SG). • Apply loads on top of AC layer.	• Apply dynamic loads of different amplitudes using 11.9-inch circular flexible plate, simulating the FWD loading duration for low number of cycles. • Apply increasing static load until failure using 11.9-inch circular steel plate.
4	• Impact of sloped shoulder (full pavement structure: AC, CAB, and SG with 1:1.5 side slope). • Apply loads on top of AC layer.	• Apply dynamic loads of different amplitudes using 11.9-inch circular flexible plate, simulating the FWD loading at three locations: 12, 24, and 36 inches from the edge of the slope. • Apply increasing static load until failure using 11.9-inch circular steel plate.
5	• Impact of loading on two buried utilities (full pavement structure: AC, CAB, and SG). • Apply loads on top of AC layer at three different locations.	• Apply dynamic loads of different amplitudes using 11.9-inch circular flexible plate, simulating the FWD loading duration for low number of cycles. • Apply increasing static load until failure using 11.9-inch circular steel plate.

No. = number; FWD = falling weight deflectometer.

This report (Volume II: Appendix A) is the second of 10 volumes and presents a summary of the comprehensive experimental program designed and conducted to verify and calibrate multiple theoretical approaches for the superheavy load (SHL)–analysis methodology.[1–9] The analysis procedures developed and associated objectives (including related volume number) are summarized in table 2.

Table 2. Developed analysis procedures to evaluate SHL movements on flexible pavements.

Procedure	Objective
SHL analysis vehicle	Identify segment(s) of the SHL-vehicle configuration that can be regarded as representative of the entire SHL vehicle (Volume III: Appendix B)[2]
Flexible pavement structure	Characterize representative material properties for existing pavement layers (Volume IV: Appendix C and Volume V: Appendix D)[3,4]
SG bearing failure analysis	Investigate instantaneous ultimate shear failure in pavement SG (Volume VI: Appendix E)[5]
Sloped-shoulder failure analysis	Examine the stability of sloped pavement shoulder under an SHL-vehicle movement (Volume VII: Appendix F)[6]
Buried utility risk analysis	Perform risk analysis of existing buried utilities (Volume VIII: Appendix G)[7]
Localized shear failure analysis	Inspect the likelihood of localized failure (yield) in the pavement SG (Volume VI: Appendix E)[5]
Deflection-based service limit analysis	Investigate the development of premature surface distresses (Volume VI: Appendix E)[5]
Cost allocation analysis	Determine pavement damage associated cost attributable to SHL-vehicle movement (Volume IX: Appendix H)[8]

The comprehensive experimental program included five large-scale-box experiments (table 1) that were conducted to achieve the following objectives:

- Verify the soil-strength parameters (cohesion (c) and angle of internal friction (ϕ)) as estimated by the proposed falling-weight-deflectometer (FWD)-based methodology developed in this project.
- Verify the applicability of the proposed bearing capacity approach for SHL-vehicle loading.
- Investigate the influence of a sloped shoulder on edge shear failure under FWD-type loading as well as slower loading conditions.
- Assess the influence of loading on flexible and rigid buried utilities.

Each experiment was extensively instrumented to provide a comprehensive database of the system response. In all cases, the vehicular loading was simulated using an 11.9-inch circular

plate. Linear variable differential transformers (LVDTs) were used to record surface pavement deformations up to 60 inches from the center of the surface load. Surface and embedded accelerometers (ACCs) were installed to measure accelerations at various locations that, in turn, can be used to estimate the displacements at the same locations. Total earth pressure cells (TEPCs) were used to capture the stresses induced in the CAB and SG layers due to surface loading. Strain gauges were attached to the AC layer as well as the utility pipe to provide the strain distribution resulting from the surface loading.

CHAPTER 2. ELEMENTS OF EXPERIMENTAL PROGRAM

2.1. DESCRIPTION OF LARGE-SCALE BOX

To achieve this experimental program's objectives, a large container was requited. Thus, the research team designed, fabricated, and built a large-scale box with internal dimensions of 124 by 124 by 72 inches. The large-scale box consisted of a steel base plate, H-shaped steel columns infilled with 4- by 6- by 30-inch wood beams and braced at two levels with steel beams and tension rods to act as a lateral bracing system. Figure 1 and figure 2 show drawings of the large-scale box.

The steel base plate was grouted to the laboratory floor, and 20 steel columns were appropriately aligned and welded to the base plate. After the assembly of the steel columns, a total of 224 4- by 6- by 30-inch wood beams of were fitted between the columns. Polyvinyl chloride (PVC) foamboards were used as filler between the gap inside the web of the columns and the wood beams. A screw/nut fastening method was used to install the bracing system, which consisted of eight steel beams and four tension rods.

2.2. EXPERIMENTAL SETUP

Since the experimental program included dynamic loading applied to a pavement structure contained within the large-scale box, there was a concern about introducing measurement errors in the data collected from the sensors due to reflection of the waves at the boundary. A common technique to minimize such error is to install wave-absorbing material on the inside walls of the large-scale box. A field experiment was performed to determine the best commercially available wave-absorbing material.

The following four damping materials were tested: insulation foam, cushion pad, fiberglass, and bubble wrap. It was concluded that fiberglass provided the best absorbing mechanism, and thus, it was selected for this project. Accordingly, the floor and the inner walls of the large-scale box were covered by a fiberglass material (with paper-vapor-retarder side facing inside) that is commercially available for use as insulation. The PVC foamboards acted as an additional wave absorber at the boundaries during the dynamic tests.

A plastic sheet was placed all around the inside of the completed large-scale box. This sheet was intended to provide a frictionless boundary for vertical deformation similar to what is expected in the field. The detailed experimental setup is explained in section 2.7 of this report.

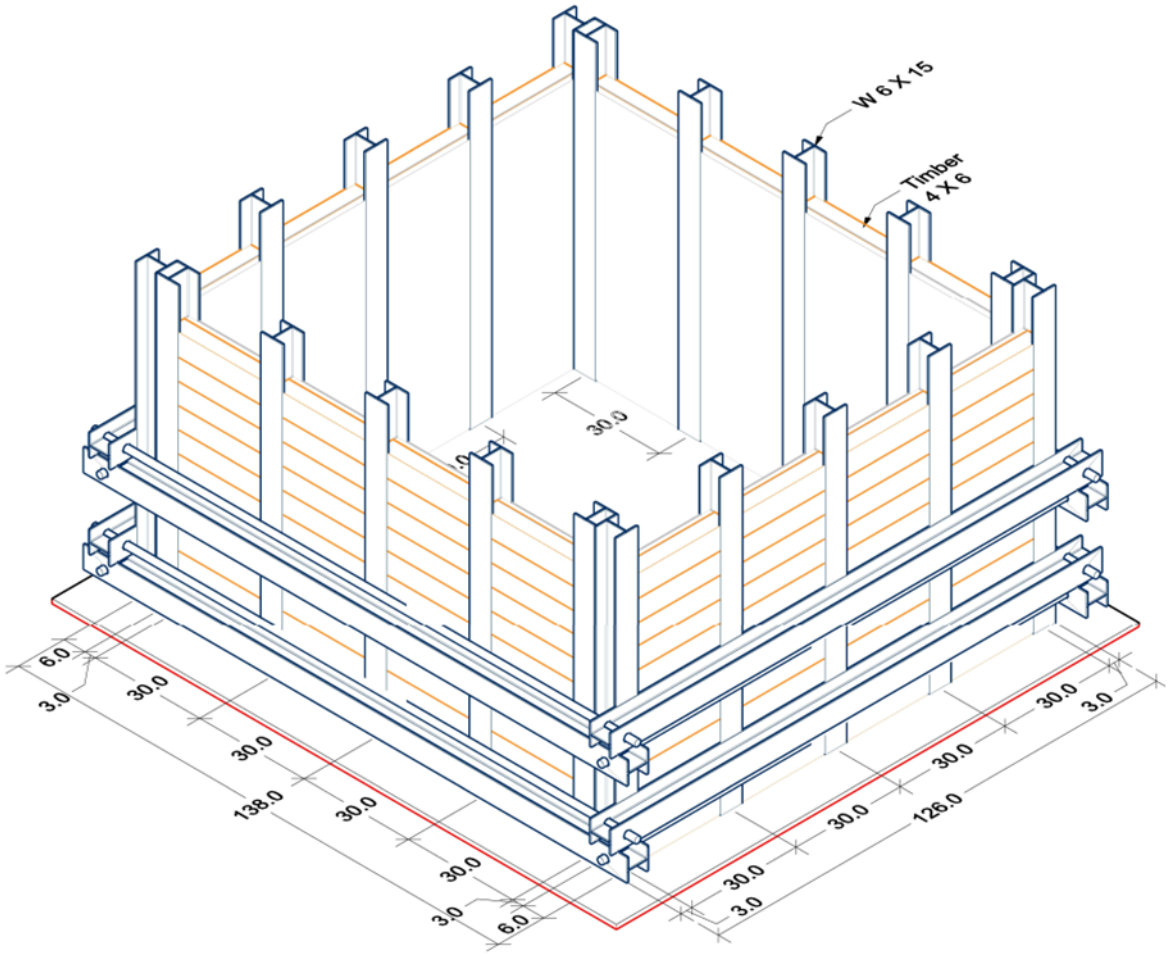

Note: All dimensions are in inches.

Figure 1. Illustration. Three-dimensional schematic of the large-scale box.

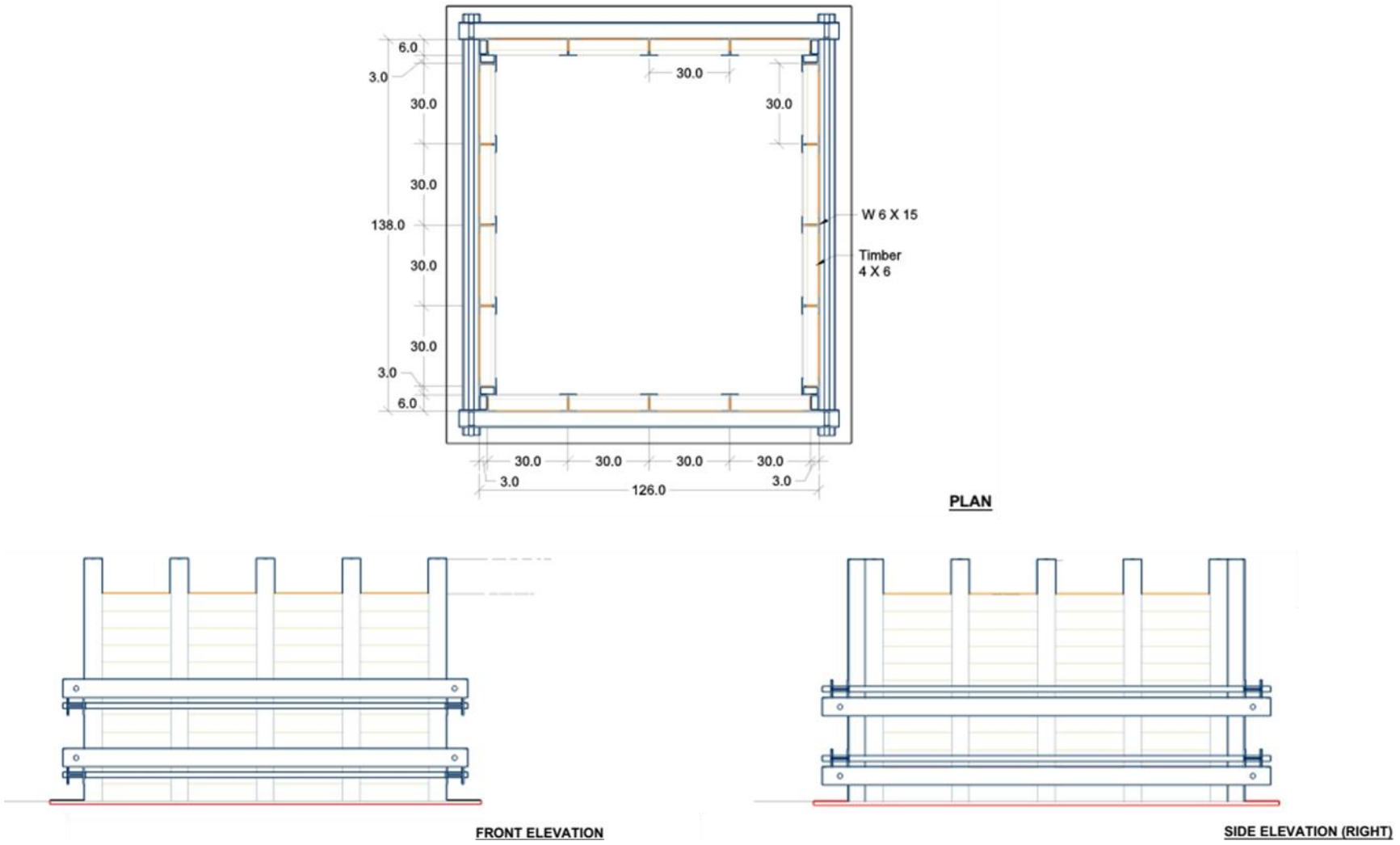

Note: All dimensions are in inches.

Figure 2. Illustration. Plan view and front and side elevations of the large-scale box.

2.3. CHARACTERISTICS OF SG MATERIAL

The SG in a pavement structure is routinely a natural material. The SG material in the large-scale-box experiments was procured from a local source, and this section provides details of its characterization.

2.3.1. Soil Classification

The results of the sieve-analysis test, undertaken in accordance with American Association of State Highway and Transportation Officials (AASHTO) T 11 and AASHTO T 27, are shown in figure 3.[10,11] The Atterberg limits were determined in accordance with AASHTO T 89 and AASHTO T 90, and the results are summarized in table 3.[12,13] The SG soil was classified as A-2-7 according to the AASHTO system (AASHTO M 145) and as "clayey sand with gravel" (group symbol: SC) according to the Unified Soil Classification System (ASTM D2487).[14,15]

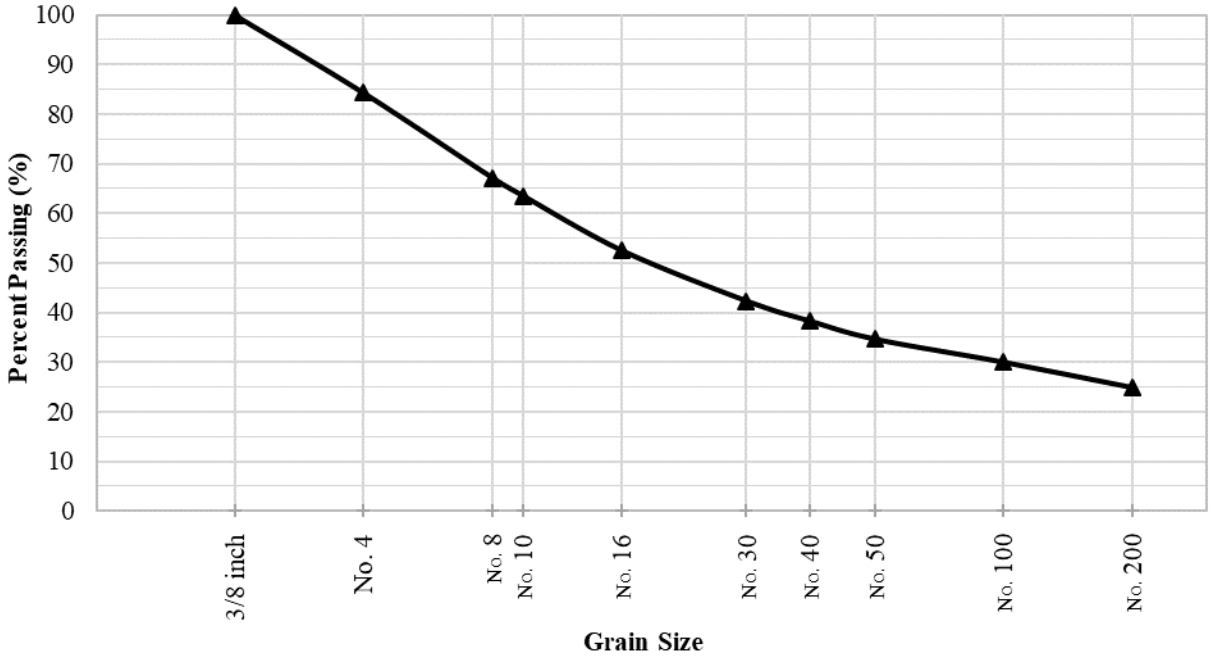

Figure 3. Graph. Gradation of SG material.

Table 3. Atterberg limits of SG material.

Atterberg Limits	Value (%)
Liquid Limit	43
Plastic Limit	23
Plasticity Index	20

The quality of a soil as a highway SG material is typically estimated based on the group index (GI). In general, the quality of performance of a soil as an SG material is inversely proportional to the GI. The GI is calculated for A-2-7 material using the equation shown in figure 4, where P_{200} is the percentage passing through the number (No.) 200 sieve and *PI* is plasticity index. A GI of 1 was calculated for the tested SG material, and the SG was classified as A-2-7(1).

$$GI = 0.01 \times (P_{200} - 15)(PI - 10)$$

Figure 4. Equation. GI for A-2-7 soils.

2.3.2. Resilient Modulus

The resilient modulus (M_R) represents the stiffness of a material under control confinement condition and repeated vertical loading. The M_R test aims at simulating stress conditions that occur in the pavement structure. The M_R test for the SG material used in the large-scale-box experiments was conducted in accordance with AASHTO T 307.[16] The moisture–density relation (compaction curve) for the SG material was developed in accordance with AASHTO T 99 (figure 5).[17] A maximum dry density (γ_{dmax}) of 125.5 pcf swas achieved at an optimum moisture content (W_{opt}) of 11.8 percent. A summary of specimen preparation, testing, and test results for M_R is presented next.

The required amount of water based on the moisture–density curve was added to the dry SG material to bring it to W_{opt}. The SG material and water were mechanically mixed until the soil became uniform in color and consistency (approximately 4 min). To cure the soil, it was placed in buckets and sealed with thick plastic covers for a period of 16 to 24 h.

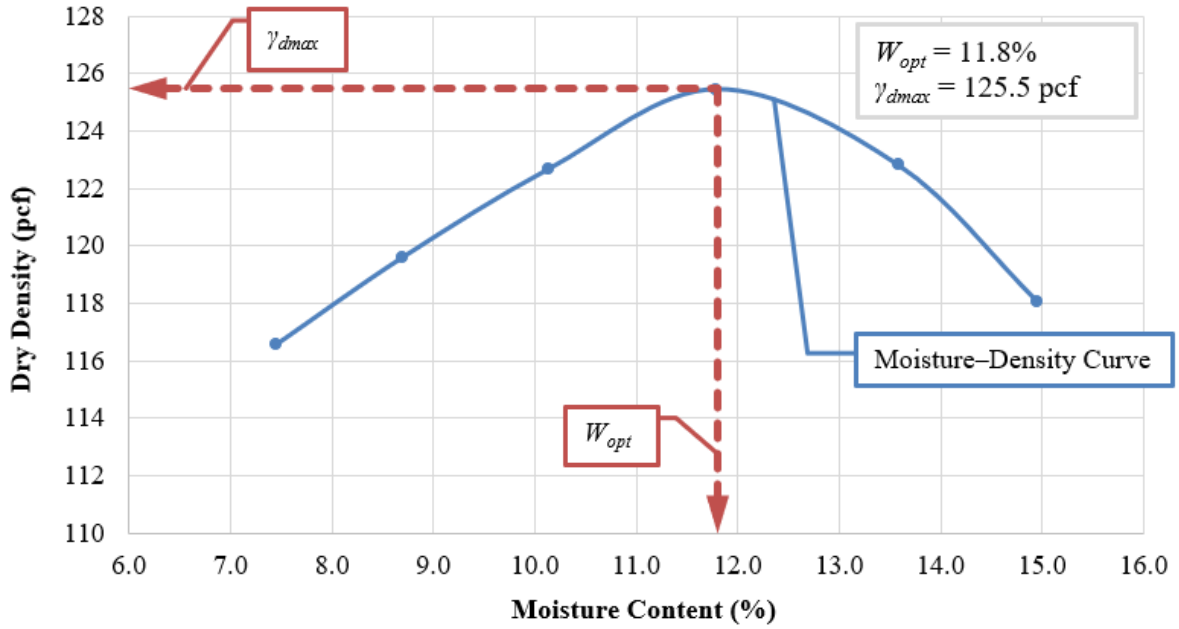

Figure 5. Graph. Moisture–density curve of the A-2-7(1) SG material.

After curing, the specimens were fabricated to be 12 inches in height with a 6-inch diameter (figure 6). For the purpose of compaction, a heavy-duty mechanical drill with a 6-inch cap was employed (figure 7). The specimen was compacted in 15 lifts that resulted in a relative compaction of about 91 percent. It should be noted that the surface of each compacted lift was scarified to a depth of about 0.125 inch to avoid debonding between the lifts (figure 8).

Figure 6. Photo. Cylindrical mold for the preparation of M_R test specimens.

Figure 7. Photo. Drill hammer for the preparation of M_R test specimens.

Figure 8. Photo. Scarifying tool for the preparation of M_R test specimens.

The test specimen, surrounded by a latex membrane, was secured with top and bottom porous stone caps with moist paper filters placed between the porous stone and specimen. The membrane was carefully sealed with caps by using O-rings (figure 9). The specimen assembly secured within the triaxial cell is shown in figure 10. The load sequences, in accordance with AASHTO T 307, were applied.[16] Axial deformation and rebound of the specimen were monitored using LVDTs. M_R for each sequence was calculated from the average of the last 5 loading cycles from the applied 100 cycles. After completion of the M_R test, the testing program continued with a quick shear test. Figure 11 and figure 12 display an SG specimen before the M_R test and after the quick shear test, respectively.

Figure 9. Photo. M_R test specimen surrounded by a latex membrane.

Figure 10. Photo. M_R test specimen assembled in a triaxial cell.

Figure 11. Photo. Compacted SG specimen before M_R test.

Figure 12. Photo. Compacted SG specimen after quick shear test.

It is well accepted that an increase in M_R resulting from an increase in bulk stress (θ) is commonly referred to as stress-hardening behavior. On the other hand, stress-softening behavior exhibits a decrease in M_R with an increase in deviator stress (σ_d). Constitutive models are generally used to estimate M_R of the material as a function of stress state. Three constitutive models that represent hardening behavior (referred to as the Theta model or K-θ), softening behavior (referred to as the log-log model or K-σ_d), and hardening–softening behavior (referred to as the Uzan model) were considered to describe the behavior of the tested SG material under the M_R testing condition (figure 13 through figure 15), where K is the regression constant of M_R model. In these models, the exponents of θ and σ_d, n and m, are expected to have a positive and a negative value, respectively.

$$M_R = K\theta^n$$

Figure 13. Equation. Theta model for hardening material.

$$M_R = K\sigma_d^m$$

Figure 14. Equation. Log-log model for softening material.

$$M_R = K\theta^n\sigma_d^m$$

Figure 15. Equation. Uzan model for hardening–softening material.

In order to identify the parameters of the models, the method of least squares in Microsoft® Excel™ Solver was employed. The calculated parameters for the evaluated models are presented in table 4. These parameters are for M_R, θ, and σ_d and are given in pounds per square inch. Figure 16 through figure 18 depict the comparison between the measured and calculated M_R using the constitutive models and associated model parameters. It can be seen that the M_R values calculated using the Uzan model, which considers both hardening and softening behaviors, show the best agreement to the measured values. The results of M_R tests on the SG material revealed that the increase in σ_d at a constant confining pressure resulted in the increase in the M_R value. The log-log model reflects the softening characteristics of an unbound material. Such a model did not properly capture the behavior of the tested SG material indicated by a positive value for the *m* parameter.

Table 4. Calculated parameters of SG constitutive models.

Model	Stress-Dependent Behavior	*K* Parameter	*n* Parameter	*m* Parameter
Theta model	Hardening	1,140.40	0.704	—
Log-log model	Softening	4,677.35	—	0.483
Uzan model	Hardening–softening	1,011.28	0.808	−0.106

—Not applicable.

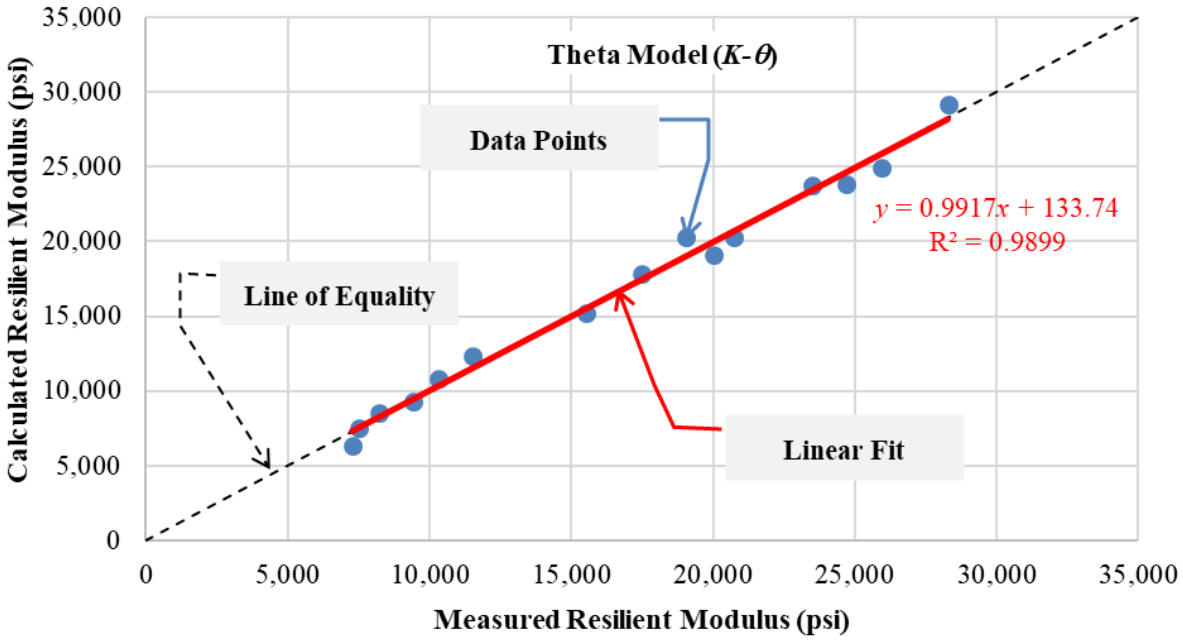

Figure 16. Graph. Measured versus calculated SG M_R using the Theta model.

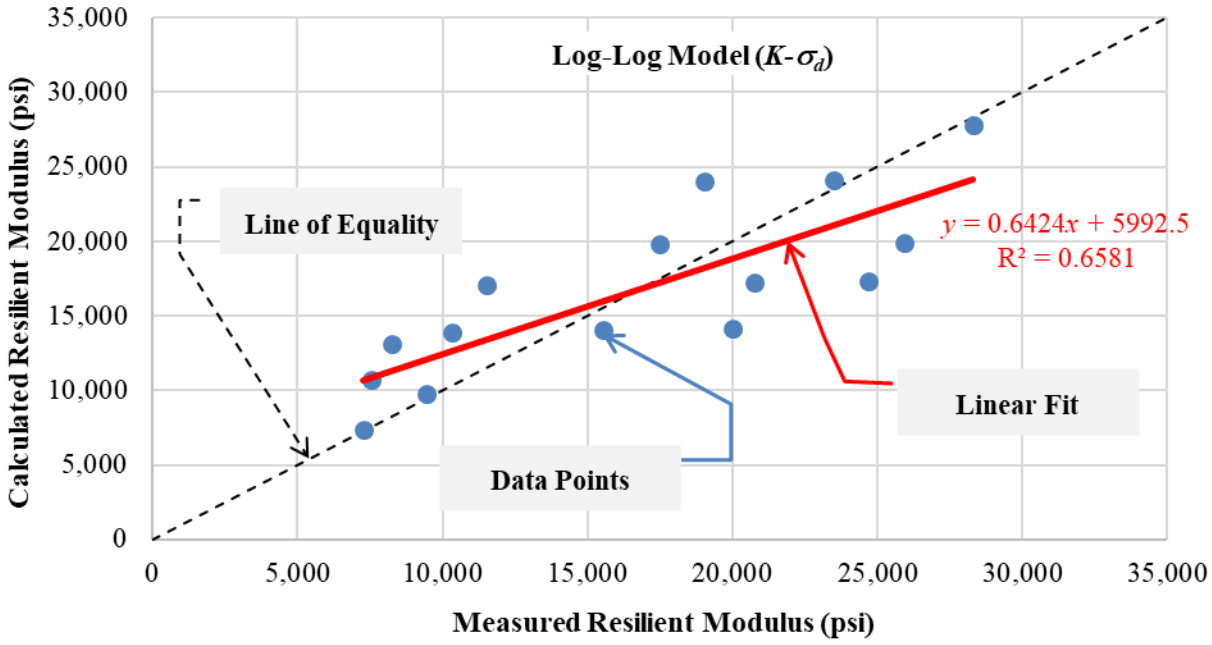

Figure 17. Graph. Measured versus calculated SG M_R using the log-log model.

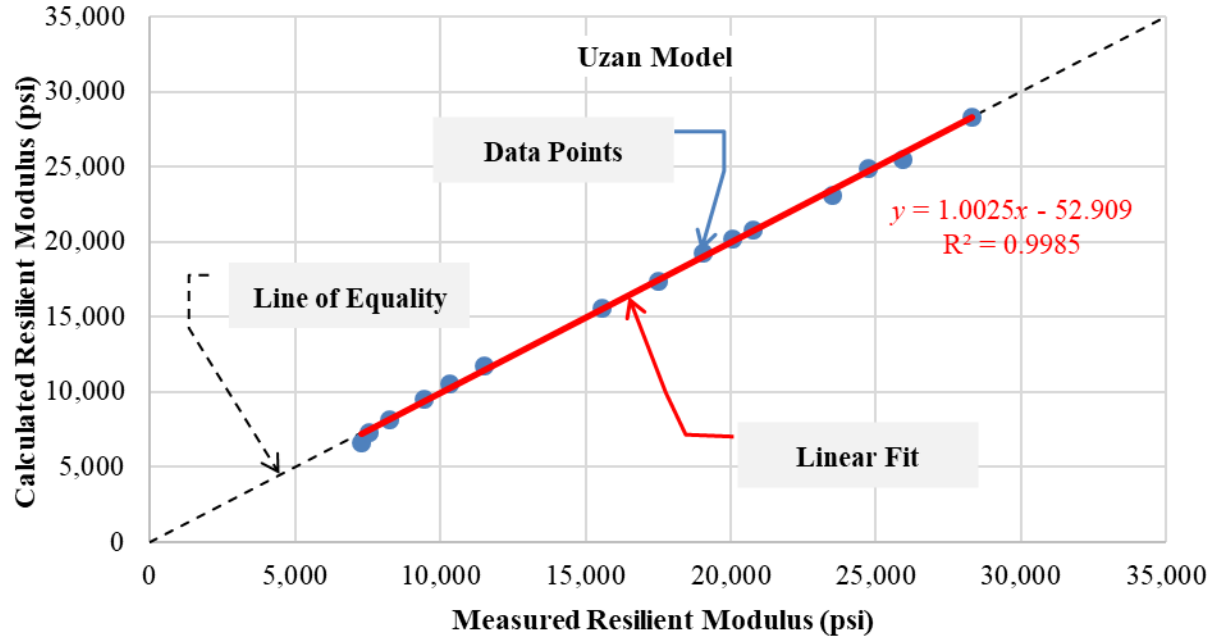

Figure 18. Graph. Measured versus calculated SG M_R using the Uzan model.

2.3.3. Shear Strength Parameters

The shear strength of a soil mass is the internal resistance offered by the soil along a failure plane. The shear strength, which is a function of normal stress on the failure plane, can be expressed by the following equation (figure 19), which is referred to as the Mohr–Coulomb failure criterion.

$$\tau_f = c + \sigma_f . tan\emptyset$$

Figure 19. Equation. Mohr–Coulomb failure criterion.

Where:

τ_f = shear strength at failure.
σ_f = normal stress at failure.

c and ϕ are widely used strength parameters in geotechnical designs. Different laboratory techniques have been employed to determine these parameters. Triaxial compression testing is one of the well-accepted methods for this purpose.

In accordance with ASTM D7181, the triaxial testing was carried out to determine the shear strength parameters of the SG material.[(18)] The test was conducted in unsaturated conditions (i.e., no saturation phase and without any pore-water pressure measurements). It is believed that the test condition represented the actual SG condition in the large-scale-box experiments. A summary of specimen preparation, testing, as well as test results is presented next.

First, the required amount of water was added to the dried soil sample to bring it to W_{opt}. Next, the soil sample and water were mechanically mixed until the SG became uniform in color and consistency (approximately 4 min). The mixture was then placed in buckets and sealed with thick plastic covers. The sealed mixture was cured for a period of 16 to 24 h.

A split mold with a 2.8-inch internal diameter and a static compactor load frame were used to compact the sample into cylindrical test specimens. Each test specimen was compacted in five lifts of equal weight under static load applied from a hydraulic load frame. The final height of the compacted specimen (i.e., 6 inches) was marked on the pusher rod with five equal divisions. These marks show the targeted compacted height of each layer. The split mold and the pusher rod with marks are shown in figure 20.

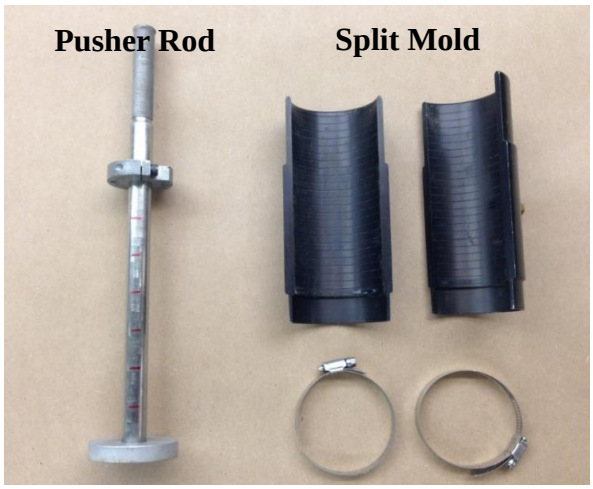

Figure 20. Photo. Pusher rod and split mold used to prepare specimens for the triaxial test.

The portion of wet soil for one lift was placed in the split mold. With the use of a spatula, the soil sample was drawn away from the edge of the mold to form a slight mound in the center. Static compressive load with a slow rate of movement (about 0.2 inch per min) was applied. The application of the ram movement was stopped when the lift height passed the respective mark on the pusher rod. The load was maintained for about 1 min to reduce the excessive rebound. The load was retrieved, and the rod used to push the sample was removed from the mold. The top surface of the compacted specimen was scarified to a depth of about 0.12 inch in order to give a good bonding with the next lift. The wet mass of soil for the next lift was placed over it, and the same procedure was followed until the completion of the compaction of the fifth lift. Specimen preparation with a static compactor is shown in figure 21. The compacted specimen was taken out of the mold by splitting the mold. After measuring the height, the latex membrane was immediately secured to the cylindrical specimen to prevent further moisture loss to air.

Figure 21. Photo. Static compaction of triaxial test specimen.

In order to conduct the test, an automated triaxial apparatus was utilized. This system is operated by the software that automates the initialization, consolidation, and deviator load application (figure 22).

Figure 22. Photo. Automated triaxial apparatus.

The triaxial tests at two different confining pressures of 5 and 10 psi were performed. Figure 23 depicts σ_d versus axial strain (ε_a) of the SG in these two tests. Consequently, σ_d at failure (σ_{df}) of 23.0 and 39.1 psi were obtained for the two respective confining pressures. Accordingly, as shown in figure 24, ϕ of 38 degrees and c of 2 psi were calculated.

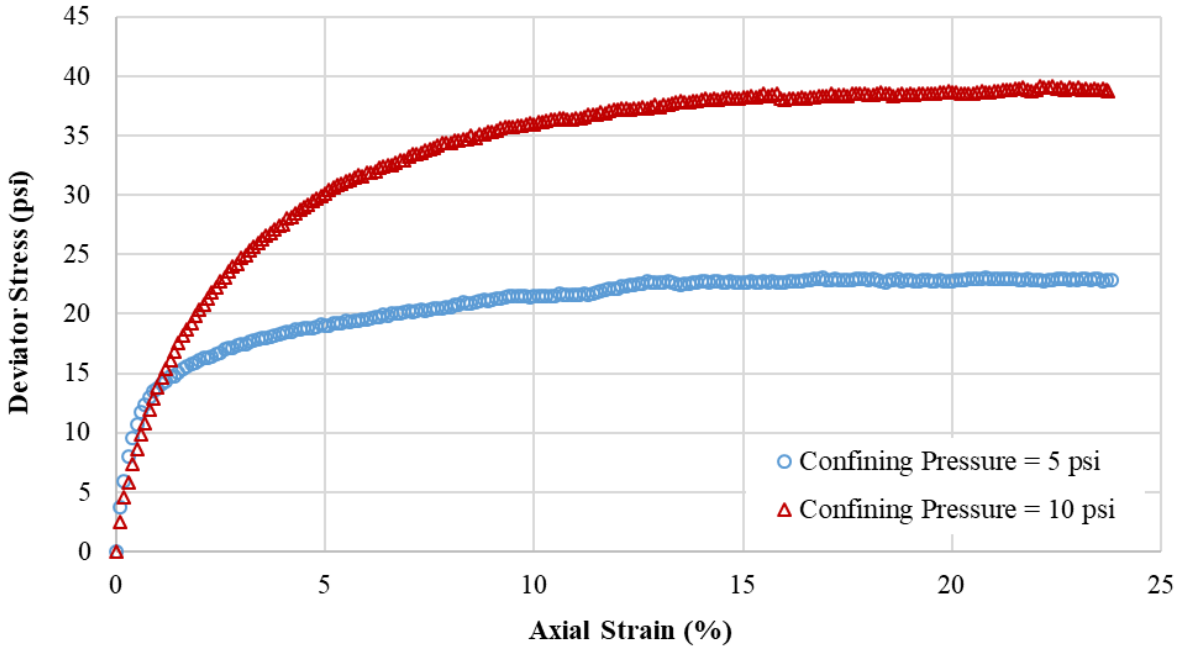

Figure 23. Graph. σ_d versus ε_a for SG material at two different confining pressures.

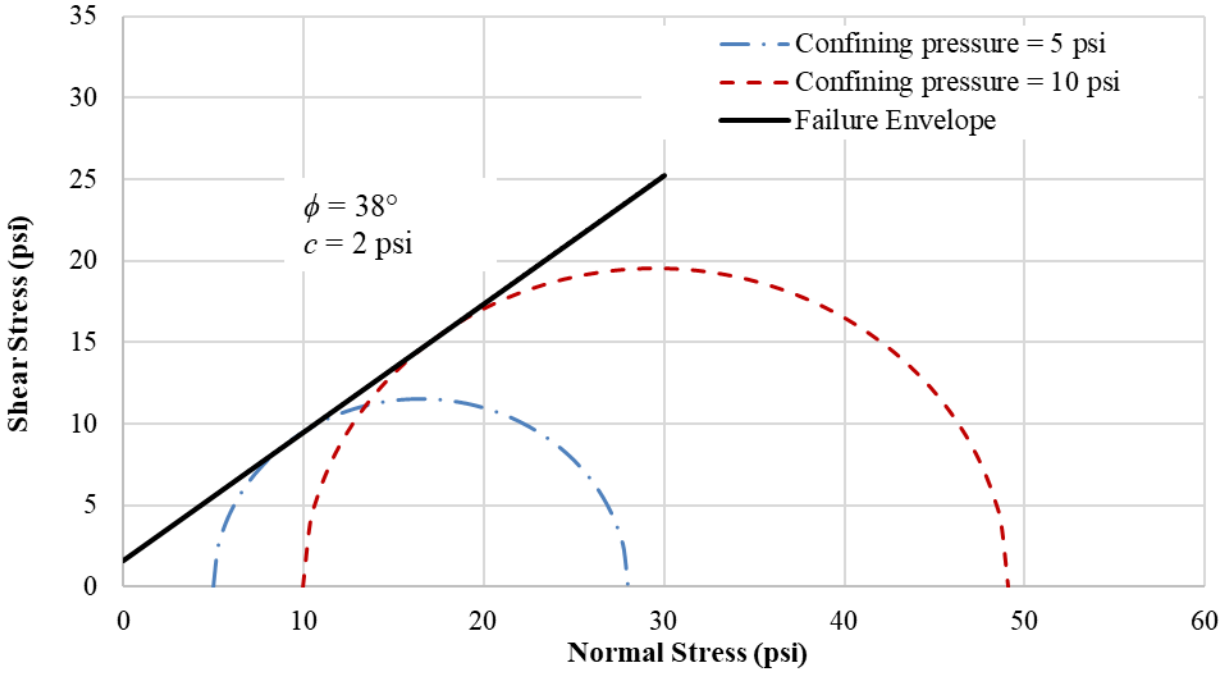

Figure 24. Graph. Mohr–Coulomb failure criterion for SG material.

2.4. CHARACTERISTICS OF BASE MATERIAL

A typical CAB was used in the large-scale-box experiments. The CAB material was selected following the Nevada Department of Transportation materials' specification for dense-graded CAB (Type 2, Class B).[19] The CAB material, from a supplier in northern Nevada, was sampled according to the AASHTO T 2 protocol and brought for testing.[20] Using AASHTO T 248 splitting methods, the sample was reduced in size and blended until an adequate sample size and mix were achieved.[21] From the blended sample, the AASHTO T 27 and AASHTO T 180 protocols were followed to determine the gradation, γ_{dmax}, and W_{opt}.[11,22] γ_{dmax} for the evaluated CAB was 138.2 pcf, the maximum wet density was 149.7 pcf, and W_{opt} was 8.3 percent.

2.5. CHARACTERISTICS OF ASPHALT CONCRETE MATERIAL

A typical dense-graded hot-mix asphalt (HMA) with a PG64-22 unmodified asphalt binder and a nominal maximum aggregate size of 0.75 inch was used in the large-scale experiments. Summaries of aggregate gradation and mixture properties of HMA materials are presented in table 5 and table 6.

Table 5. Aggregate gradation of HMA used in experiments.

Sieve	Percent Passing	Specification
1 inch	100	100
3/4 inch	100	93–100
1/2 inch	90	—
3/8 inch	78	71–85
No. 4	51	45–48
No. 8	38	—
No. 10	35	31–39
No. 16	29	—
No. 30	22	—
No. 40	19	15–23
No. 50	14	—
No. 100	9	—
No. 200	6.6	4.6–8

—No data.

Table 6. Mixture properties of HMA used in experiments.

Property	Value
Binder content	4.6%
Air void	4%
Voids in mineral aggregate	13.7%
Voids filled with asphalt	71.1%
Theoretical maximum specific gravity	2.478
Marshall stability	3,618 lb
Marshall flow	14 hundredths of an inch

2.6. DATA ACQUISITION SYSTEM

A National Instruments™ (NI) data acquisition system that comprises 2 12-slot SCXI-1001 chassis populated with 18 NI SCXI-1320 conditioners was used to acquire the sensor data in the large-scale-box experiments. This 72 data-channel system is capable of sampling data at frequencies that range from 1 to 3,000 Hz. Such a system is useful for acquiring data from a wide range of sensors, including strain gauges, displacement transducers, load cells, pressure cells, and ACCs. Data from experiments involving dynamic loading were acquired at 1,024 Hz to accommodate the requirements of the double integration algorithm for assessing the displacements. Data from experiments with static loading were acquired at 32 Hz. Once the data were acquired, they were stored locally on the computer hard drive in comma-separated values files that could be imported and utilized by most software packages for data analysis.

2.7. LARGE-SCALE BOX TEST PREPARATION

This section summarizes the procedure followed in the erection of SG, base, and AC layers within the large-scale box.

2.7.1. SG Deposition in Large-Scale Box

The goal was to place the SG material at 11-percent moisture content and at 90-percent γ_{dmax} to a depth of 5.5 ft. The process of placing the SG material was labor intensive but straightforward. The material was shoveled from the stockpile into 5-gal buckets, placed in a concrete mixer, and mixed for less than 1 min. In some experiments, the SG material was preconditioned to W_{opt} to reduce construction time. The wet SG was mixed for approximately 10 to 30 s to maintain an even blend. The moist SG material was then transported and placed via a laboratory-fabricated chute and distributed within the large-scale-box area.

Among many compaction techniques (rollers, tampers, vibratory plates, etc.), a gasoline-powered vibratory-plate compactor proved to be the best option to achieve the required compaction. Three to four passes lasting approximately 5 to 8 min each were needed to arrive at a 4-inch compacted lift. Nuclear density gauge readings were taken after each lift in the large-scale box to confirm the required compaction had been reached (90-percent γ_{dmax}). Figure 25 through figure 29 show the various construction stages of placing the SG material in the large-scale box.

While a nuclear density gauge was used to ensure the target density was reached during the installation of the SG, Dynamic Cone Penetrometer (DCP) testing was also used to assess the density of the SG layer. For experiment No. 1, two DCP tests that were performed in two different locations were conducted on the surface of the finished SG after placement of all the SG lifts. Figure 30 shows the readings of the two DCP tests. In general, the results showed similar densities for the SG layer in both locations.

Figure 25. Photo. SG soil mixing in the mechanical mixer to form a uniform mix.

Figure 26. Photo. Placement of conditioned SG soil into the large-scale box via a material discharge chute in 4-inch lifts.

Figure 27. Photo. Compaction of SG soil to target density using a vibratory-plate compactor.

Figure 28. Photo. Nuclear density gauge instruments on top of a compacted lift of SG soil.

Figure 29. Photo. Scarification of the SG lift surface using a pickaxe to ensure strong bond between lifts of SG soil.

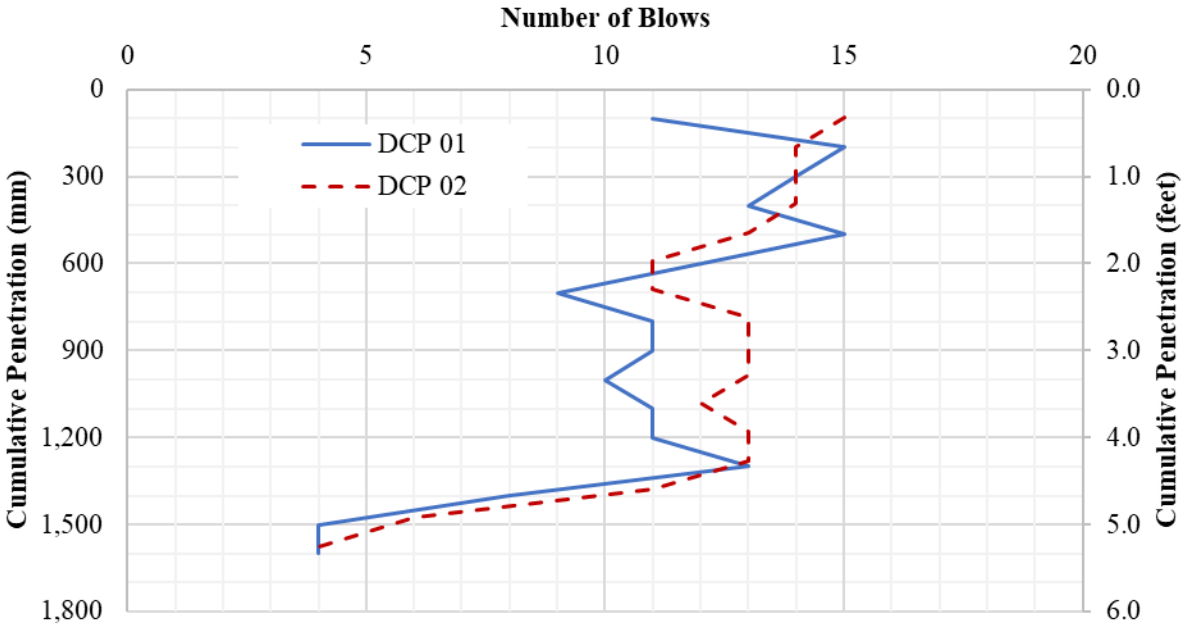

Figure 30. Graph. DCP test results for the SG layer in the large-scale box from experiment No. 1.

2.7.2. Base Deposition in Large-Scale Box

The target in-place moisture content of the CAB material was 8.3 percent with a target in-place density of 92 to 95 percent compaction (of γ_{dmax}). The total CAB-layer thickness was 6 inches, and the layer was constructed in two 3-inch lifts in a manner similar to the SG-material deposition process described in section 2.7.1. However, the CAB required more compaction effort to arrive at a 3-inch compacted lift. Nuclear density gauge readings were taken after each lift in the large-scale box to confirm the required compaction had been reached.

2.7.3. AC Deposition in Large-Scale Box

The asphalt mixture was placed using two 2.5-inch lifts. The lifts were compacted for the required duration using the vibratory-plate compactor to achieve a target in-place density of 92 to 96 percent. The asphalt mixture was delivered using a dump truck from a supplier of local hot-mix plants. The plant mix was dumped directly in front of the large-scale box and shoveled into the box. It was swiftly spread and leveled until 3 inches of uncompacted material were in place. A vibratory-plate was then driven from the outside edge to the center of the large-scale box to achieve good compaction of the lift. Upon achieving good compaction on the first AC-layer lift, the same process was repeated for the second 2.5-inch lift. A thin lift nuclear density gauge was used at several locations around the surface of the box to measure the in-place density of the compacted AC surface layer.

Plant-produced loose mixtures were sampled during placement of the material in the large-scale box and were tested for theoretical maximum specific gravity in accordance with AASHTO T 209.[(23)] The dynamic modulus was also measured on the sampled plant-produced mixture.

Loading of the pavement structure was conducted at least 7 d after the placement of the AC layer. This was done to eliminate additional uncertainties due to variability in the asphalts' material properties because of oxidative aging. Cores were taken immediately after the completion of each of the experiments to measure the thickness and verify the in-place asphalt-layer density. For experiments No. 3, No. 4, and No. 5, 10 cores were taken at various locations in the AC layer. Half of the cores were extracted from predetermined locations matching the nuclear gauge density tests.

2.7.4. Special Considerations in Experiments No. 4 and No. 5

Building the Slope (Experiment No. 4)

Construction of SG material below the slope level continued as mentioned in section 2.7.1. However, to build the side slope in experiment No. 4, a simple technique requiring wooden forms was used. A 6- by 4-inch wooden piece was installed along the side of the large-scale box at the starting level of the slope. The wooden piece was placed so that the height of the piece matched the construction lifts' height (4 inches), and its width matched the 1:1.5 slope requirement (figure 31). With each additional layer of SG soil, an additional step of wood plank was added (figure 32). Upon completion of the construction, the wooden frames were removed (figure 33), leaving steps in the compacted materials. These steps were then reshaped to a smooth slope using hand tools (figure 34). Finally, the surface of the slope was compacted using a vibratory-plate compactor (figure 35).

© 2018 UNR.

Figure 31. Photo. Slope construction in experiment No. 4: SG preparation below the slope level.

© 2018 UNR.

Figure 32. Photo. Slope construction in experiment No. 4: construction using wood planks.

© 2018 UNR.

Figure 33. Photo. Slope construction in experiment No. 4: building the slope and removing wood planks.

Figure 34. Photo. Slope construction in experiment No. 4: shaping the slope.

Figure 35. Photo. Slope construction in experiment No. 4: finished slope.

Buried Utilities—Cast-In-Place Concrete Box Culvert (Experiment No. 5)

While the steel pipe was purchased from a local hardware store, the researchers decided to cast a concrete box culvert that was 9 ft long with a 12- by 12-inch square section and a 1-inch wall thickness. The concrete box culvert was constructed inside the large-scale box at the designated testing location using self-consolidating concrete (SCC). The selection of the proper size for the flexible pipe as well as the concrete box culvert are discussed in detail in section 2.8.5.

At the bottom of the concrete box culvert, the SG soil was properly compacted, and levels were verified using self-leveling rotary laser level. The outer formwork was built using timber and plywood (the inner length between the outer forms was 12 inches), while the inner formwork was built using 2-inch-thick, extruded polystyrene, closed-cell foam panels. A welded steel-wire-mesh sheet (6- by 6-inch spacing with 1/8-inch thickness) was used to reinforce the walls of the concrete box culvert.

The SCC mix was composed of factory-blended coarse aggregates, silica fume, and other products. The advantage of using SCC was that it was easy to pour into the 1-inch-thick culvert walls and that it resulted in the mix getting excellent consolidation without the need for

vibration. Figure 36 through figure 38 show the construction process of the concrete box culvert. Cylindrical concrete specimens were obtained according to ASTM C39/C39M to measure the compressive strength of the SCC.[24]

Figure 36. Photo. Construction of the concrete box culvert formwork in the large-scale box.

Figure 37. Photo. Mixing of SCC in a bucket.

Figure 38. Photo. Pouring of SCC in the box-culvert formwork.

The outer wooden formwork was removed 1 d after the completion of the SCC work, and the inner foam formwork was removed when the SCC aged 3 d. Figure 39 shows the final concrete box culvert upon removal of formworks.

Figure 39. Photo. Concrete box culvert in the large-scale box upon removal of formwork.

The compressive strength of the SCC was measured using the sampled cylindrical specimens in accordance with ASTM C39/C39M at 1, 7, 14, 28 d, and test day.[24] Figure 40 shows the measured compressive strength at the various dates. The compressive strength on test day was 8,348 psi.

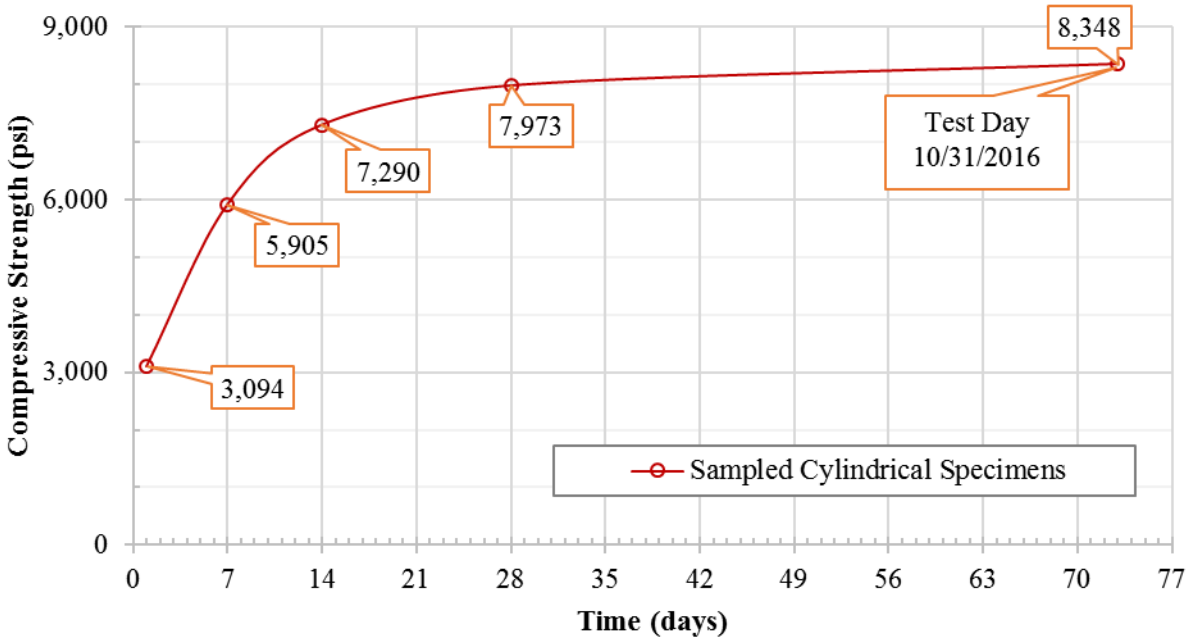

Figure 40. Graph. Unconfined compressive strength of SCC-mix cores at various dates.

Construction of SG soil below the concrete box culvert was undertaken as mentioned in section 2.7.1. However, the SG in the zone directly adjacent to the utilities required special attention during placement. Each lift of SG (4-inch lifts) within this zone was manually compacted using wood and mallets as shown in figure 41. The remaining area (a few inches away from the utilities) was compacted as usual using the vibratory-plate compactor.

Figure 41. Photo. Manually compacting SG soil around the steel pipe.

2.8. LOADING PROTOCOL AND INSTRUMENTATION PLANS

A hydraulic ram capable of delivering 60,000 lb of force was used to apply the surface loads. The ram was modified by attaching a spool valve that could be electronically controlled to provide the required flow to the ram to achieve the target dynamic load with the target pulse duration. This control mechanism also allowed the static load to be applied in a controlled manner. The system was connected to a hydraulic pump and accumulators to ensure the necessary flow of hydraulic fluid for the repeated cycles of loading. The ram was mounted onto a stiff horizontal steel beam connected between two vertical steel columns that comprised the reaction frame.

A computer running a real-time operating system was connected to an NI four-slot SCXI-1001 chassis populated with two NI SCXI-1320 conditioners that were used to control the servo valve. A 100,000 lb interface pancake-type load cell along with a string pot were attached to the ram and were electronically connected to the controller. The controller design was a proportional-integral-derivative controller. This control loop-feedback mechanism was used to control the ram in either force- or displacement-control mode depending on the mode selected for testing. Careful calibration of the gain was essential to ensure the proper operation of the entire loading system.

An FWD loading plate with an 11.9-inch diameter was used to apply the dynamic loads on top of the pavement structure to better simulate actual tire loading conditions (figure 42 and figure 43). The ratio of the large-scale box's dimensions to the diameter of the loading plate was deemed sufficient to minimize the interference from the large-scale box's boundaries. In contrast, an 11.9-inch diameter by 1-inch-thick steel loading plate was used to apply the static loads on top of the AC layer (figure 44 and figure 45).

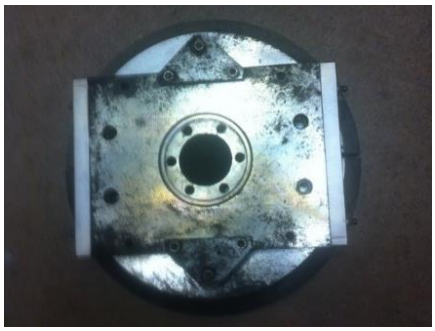

Figure 42. Photo. Top view of the FWD loading plate used for dynamic loading in the large-scale-box experiments.

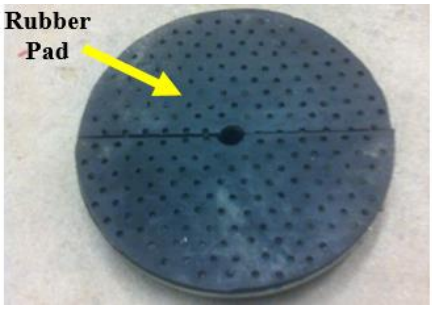

Figure 43. Photo. Bottom view of the FWD loading plate used for dynamic loading in the large-scale-box experiments.

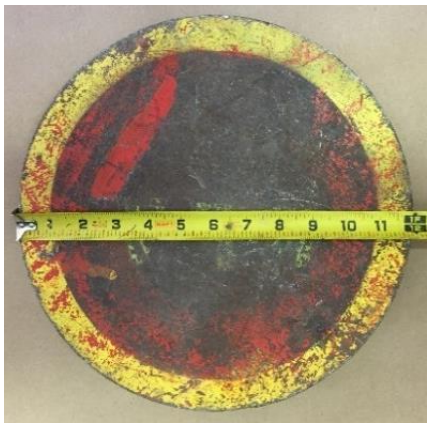

Figure 44. Photo. Top view of the circular steel plate (12-inch diameter) used for static loading in the large-scale-box experiments.

Figure 45. Photo. Side view of the circular steel plate (1-inch thickness) used for static loading in the large-scale-box experiments.

Various sensors were used in the experiments to capture the responses of the pavement structure and buried utilities to surface loading. Nonvibrating wire TEPCs were used to measure the total vertical stresses at different locations within the domain. These cells were 4 inches in diameter with capacities that ranged between 36 and 362 psi. LVDTs with ranges from 0 to 4 inches were used to capture surface deflection of the pavement and monitor deflections inside the buried utilities. ACCs capable of measuring acceleration up to 5 g in three directions were used in the various experiments. Embedded strain gauges for AC were also used to capture the response of the entire pavement under dynamic and static loading and provide a comprehensive picture of the pavement responses (stress, strain, and deformation) at interior locations along with surface deformation data. Three-element rosette strain gauges (45 and 90 degrees) were used to capture the strain in the buried steel pipe.

2.8.1. Experiment No. 1 (SG Layer Only)

In experiment No. 1, the loads were applied on top of the SG layer directly; no AC or base layers were present. The thickness of the SG was 66 inches. Two types of loadings were applied: dynamic and static. The testing was initially dynamic with increasing amplitudes, up to a maximum applied dynamic load ($P_{(Max)Dyn}$) that was about 10 percent of the anticipated bearing capacity load level. The intention was to apply the loads that would not impart failure and development of failure (or slip) planes in the SG. The structure was subjected to a series of five loading levels with sequentially higher load amplitudes until the $P_{(Max)Dyn}$ load level was reached. The pavement structure was subjected to multiple dynamic load pulses at each of the selected load level increments, simulating repeated loading and allowing for the resilient-type behavior of the SG. Each load pulse consisted of a pulse duration of 0.1 s followed by a rest period of 0.9 s.

At the end of the dynamic load testing, the pavement structure was allowed to recover for 30 min. An increasing static load was then applied up to failure with a constant vertical settlement rate of 0.4 inch/min. The procedures that deal with nonrepetitive static plate load tests of soils are outlined in ASTM D1196/D1196M in which the loading rate is not specified, rather a "moderately rapid" rate of loading is suggested.[25] A preliminary analysis was undertaken using 3D-Move Analysis software to estimate the vertical displacement rate for SHL vehicles moving at 10 mph.[26] This exercise revealed that the rate was in the range of 2.2 to 3.8 inches/min, which depended on the stiffness properties and layer thicknesses in the pavement structure. However, application of such a fast loading rate could cause several issues related to technical limitations in the loading ram and supporting frame. Hence, the researchers decided to apply the static load at a slower rate of 0.4 inch/min, which was consistent with the application of the σ_d rate in the triaxial test conducted for the SG material (i.e., 0.2 inch/min).

Table 7 summarizes the loading protocol for experiment No. 1. All loads were applied on the loading plate, positioned directly at the top of the SG layer and at the center of the large-scale box.

Table 7. Loading protocol for experiment No. 1 (SG layer only).

Load Type	Target Load Amplitude (lb)	Loading Cycles or Loading Rate	Load Plate Diameter (Inch)	Rest Period Between Load Levels (min)
Dynamic load (0.1-s loading plus 0.9-s rest period)	250	25 cycles	11.9 (FWD loading plate)	2
Dynamic load (0.1-s loading plus 0.9-s rest period)	500	25 cycles	11.9 (FWD loading plate)	2
Dynamic load (0.1-s loading plus 0.9-s rest period)	1,000	25 cycles	11.9 (FWD loading plate)	2
Dynamic load (0.1-s loading plus 0.9-s rest period)	1,500	25 cycles	11.9 (FWD loading plate)	2
Dynamic load (0.1-s loading plus 0.9-s rest period)	2,000	25 cycles	11.9 (FWD loading plate)	2
Static load	22,000	0.4 inch/min	11.9 (steel plate)	Constant loading rate

The details of experiment No. 1 regarding instrumentation in the SG layer are summarized in figure 46 through figure 49 and table 8. Surface LVDTs were installed diagonally to measure surface deflections at various radial distances (0, 8, 12, 24, 36, 48, and 60 inches). The LVDTs were attached to an external aluminum stationary beam that acted as a reference frame. This reference frame, in turn, was mounted to an independent concrete platform to avoid noises and vibrations from the large-scale box. The moving tip of the surface LVDTs rested on top of the SG layer.

Eight 4-inch TEPCs were also placed at three depth levels of 10, 20, and 26 inches below the SG surface. These cells were located directly under the center of the loading plate and laterally at each of the above depth levels at various locations. At the first level (10 inches from the SG surface), there were four sensors while at the second level (20 inches from the SG surface) there were three. At the bottom level (26 inches from the SG surface), there was one sensor directly under the center of the loading plate.

The sensors were installed after compacting the SG to the level of the instruments. The pressure cells were then placed carefully on a leveled surface created by a thin layer of compacted, fine material to ensure full contact with the cell and to facilitate a better bearing surface. After placement of the sensor, additional SG material was placed carefully on top of the cell and compacted by hand using a steel tamper plate. Figure 50 and figure 51 show the placement of a pressure cell in the SG layer, while figure 52 shows the completed test setup of the large-scale box for experiment No. 1.

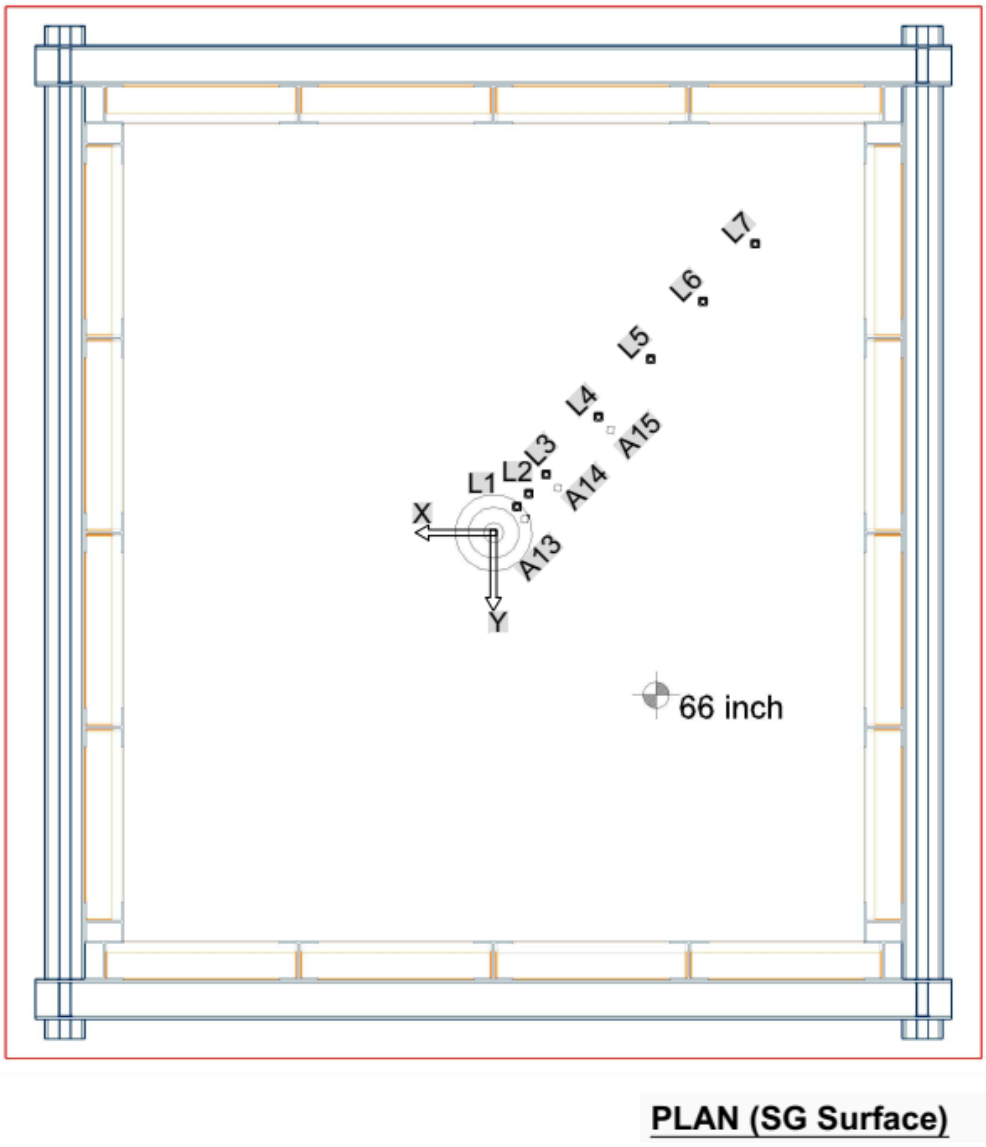

L = LVDT; A = ACC.

Figure 46. Illustration. Plan view for large-scale-box instrumentations in experiment No. 1.

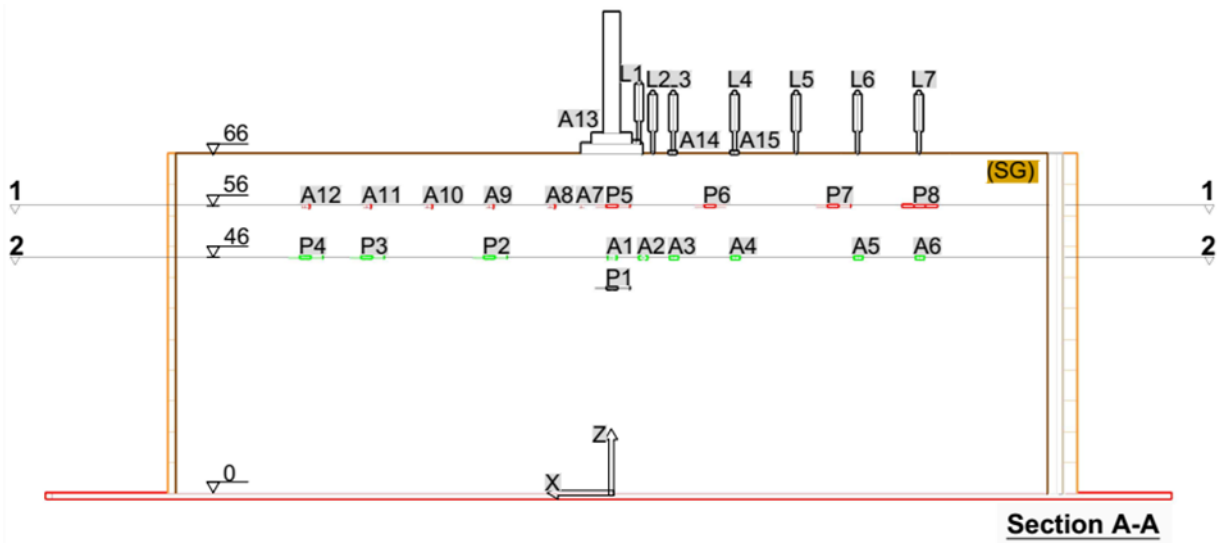

Note: All elevations are in inches.
L = LVDT; P = TEPC; A = ACC.

Figure 47. Illustration. Section A-A view for large-scale-box instrumentations in experiment No. 1.

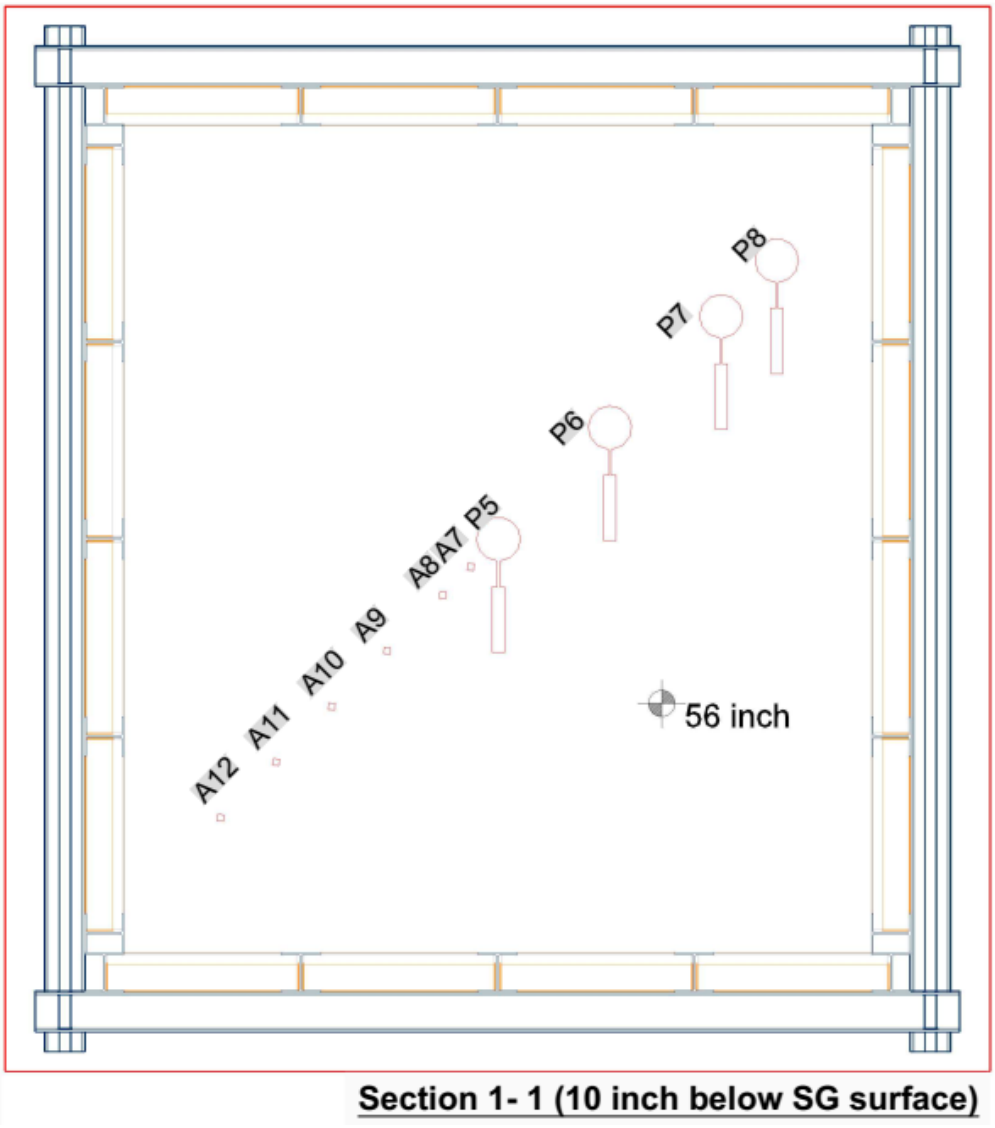

P = TEPC; A = ACC.

Figure 48. Illustration. Section 1-1 view for large-scale-box instrumentations in experiment No. 1.

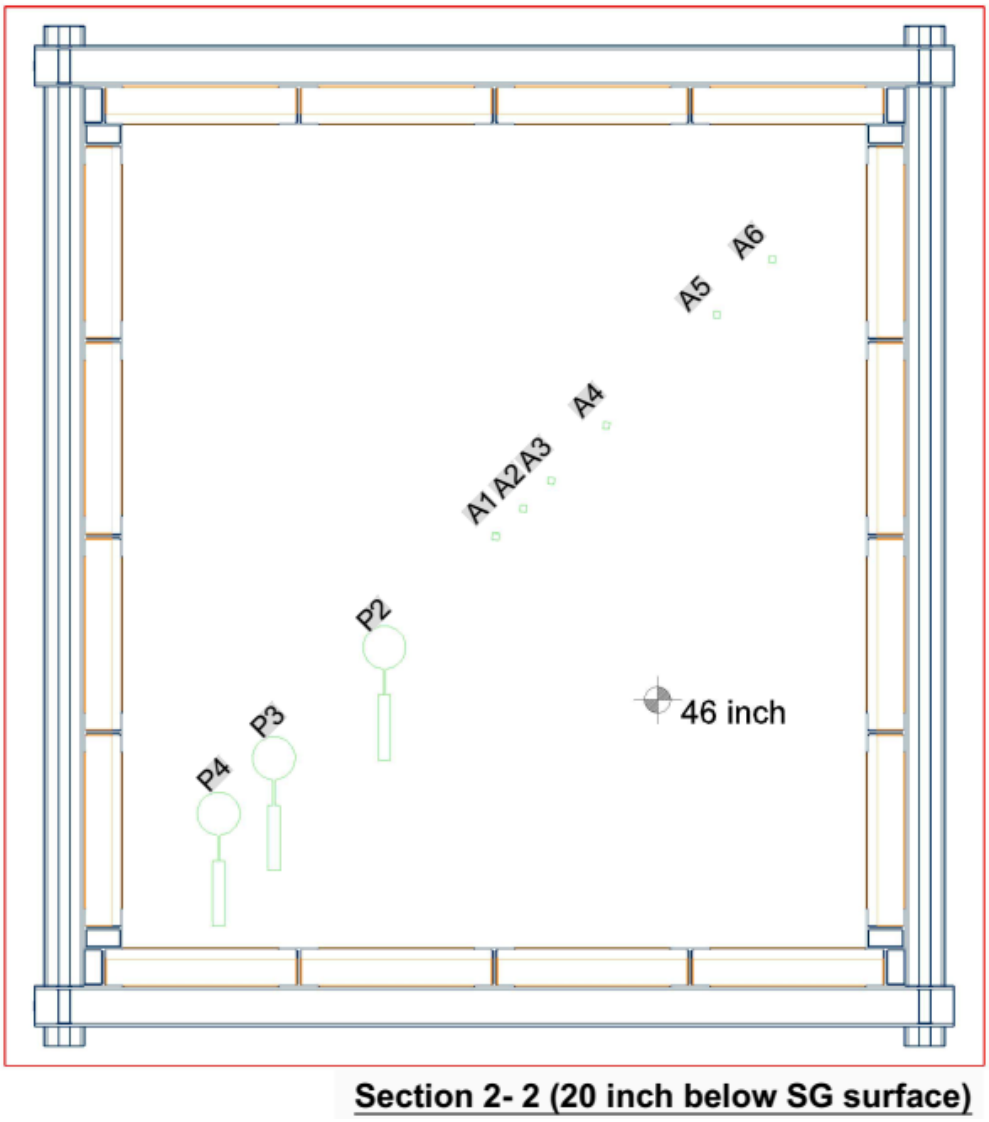

P = TEPC; A = ACC.

Figure 49. Illustration. Section 2-2 view for large-scale-box instrumentations in experiment No. 1.

Table 8. Details of the instrumentation plan for experiment No. 1 (SG layer only).

No.	Tag	Sensor Name	Capacity	Specification	Radius (Inch)	Angle (°)	Depth (Inch)	X (Inch)	Y (Inch)	Z (Inch)	ID/SN	No. of Channels	Notes
1	L1	LVDT01	4 inch	TR-0100	0	48	0	0	0	66	—	1	LVDT
2	L2	LVDT02	4 inch	TR-0100	8	48	0	−5.3	−6.0	66	—	1	LVDT
3	L3	LVDT03	4 inch	TR-0100	12	48	0	−8.0	−9.0	66	—	1	LVDT
4	L4	LVDT04	4 inch	TR-0100	24	48	0	−15.9	−17.9	66	—	1	LVDT
5	L5	LVDT05	4 inch	TR-0100	36	48	0	−23.9	−26.9	66	—	1	LVDT
6	L6	LVDT06	4 inch	TR-0100	48	48	0	−31.9	−35.9	66	—	1	LVDT
7	L7	LVDT07	4 inch	TR-0100	60	48	0	−39.9	−44.8	66	—	1	LVDT
8	P1	P01	87 psi	4-inch cell	0	228	26	0	0	40	1404682	1	Pressure cell (vertical)
9	P2	P02	36 psi	4-inch cell	24	228	20	15.9	17.9	46	1330825	1	Pressure cell (vertical)
10	P3	P03	36 psi	4-inch cell	48	228	20	31.9	35.9	46	1330822	1	Pressure cell (vertical)
11	P4	P04	36 psi	4-inch cell	60	228	20	39.9	44.8	46	1330827	1	Pressure cell (vertical)
12	P5	P05	362 psi	4-inch cell	0	48	10	0	0	56	1533652	1	Pressure cell (vertical)
13	P6	P06	87 psi	4-inch cell	24	48	10	−15.9	−17.9	56	1427206	1	Pressure cell (vertical)
14	P7	P07	87 psi	4-inch cell	48	48	10	−31.9	−35.9	56	1427204	1	Pressure cell (vertical)
15	P8	P08	87 psi	4-inch cell	60	48	10	−39.9	−44.8	56	1427205	1	Pressure cell (vertical)
16	A1	ACC01	±5 g	3-axis	0	48	20	0	0	46	—	1	ACC
17	A2	ACC02	±5 g	3-axis	6	48	20	−4.0	−4.5	46	—	1	ACC
18	A3	ACC03	±5 g	3-axis	12	48	20	−8.0	−9.0	46	—	1	ACC
19	A4	ACC04	±5 g	3-axis	24	48	20	−15.9	−17.9	46	—	1	ACC
20	A5	ACC05	±5 g	3-axis	48	48	20	−31.9	−35.9	46	—	1	ACC
21	A6	ACC06	±5 g	3-axis	60	48	20	−39.9	−44.8	46	—	1	ACC
22	A7	ACC07	±5 g	3-axis	6	228	10	4.0	4.5	56	—	1	ACC
23	A8	ACC08	±5 g	3-axis	12	228	10	8.0	9.0	56	—	1	ACC
24	A9	ACC09	±5 g	3-axis	24	228	10	15.9	17.9	56	—	1	ACC
25	A10	ACC10	±5 g	3-axis	36	228	10	23.9	26.9	56	—	1	ACC
26	A11	ACC11	±5 g	3-axis	48	228	10	31.9	35.9	56	—	1	ACC
27	A12	ACC12	±5 g	3-axis	60	228	10	39.9	44.8	56	—	1	ACC
28	A13	ACC13	±5 g	3-axis	0	0	0	0	0	66	—	1	ACC
29	A14	ACC14	±5 g	3-axis	12	48	0	−8.0	−9.0	66	—	1	ACC
30	A15	ACC15	±5 g	3-axis	24	48	0	−15.9	−17.9	66	—	1	ACC
31	A16	ACC16	±5 g	3-axis	—	—	—	—	—	—	—	1	Frame ACC
32	—	LCST01	—	—	—	—	—	—	—	—	—	1	Applied load-string pod
33	—	LC01	—	—	—	—	—	—	—	—	—	1	Applied load-load cell

—Not applicable.

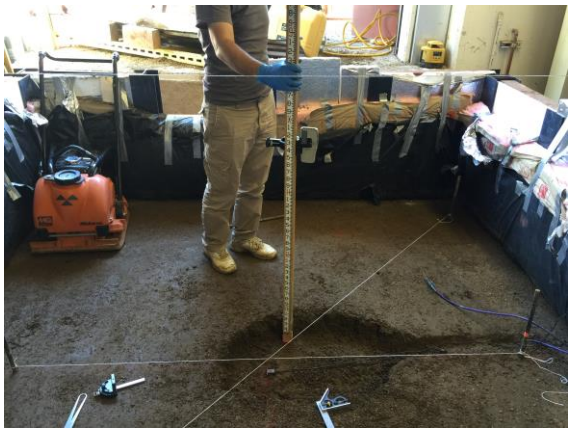

Figure 50. Photo. Instrumentation of SG layer in experiment No. 1, proper levels and locations are verified using automatic laser level and measuring tape.

Figure 51. Photo. Instrumentation of SG layer in experiment No. 1, placing instruments in proper locations and checking level and alignment.

Figure 52. Photo. Completed large-scale-box test setup for experiment No. 1.

2.8.2. Experiment No. 2 (SG and CAB Layers)

This experiment utilized unbound materials only (no AC) with a total pavement thickness of 72 inches. Figure 53 through figure 56 show drawings of the experiment No. 2 setup. The pavement structure consisted of 6 inches of CAB on top of 66 inches of SG soil. The entire pavement consisting of SG and CAB was constructed as outlined in section 2.7. The loads were applied on top of the CAB layer (at the surface).

In experiment No. 2, the pavement structure was subjected to repeated dynamic loads with amplitudes between 1,000 and 7,000 lb in 1,000 lb increments. Twenty-five cycles were applied at each incremental dynamic load with a pulse duration of 0.1 s followed by a rest period of 0.9 s in each loading cycle. The researchers subjected the structure to a series of seven loading levels, each with higher and higher load amplitudes. At the end of the dynamic load testing, the pavement structure was allowed to recover for 30 min. Similar to experiment No. 1, an increasing static load was then applied up to failure with a constant settlement rate of 0.4 inch/min. Table 9 summarizes the loading protocol for experiment No. 2. All loads were applied on the loading plate positioned directly at the top of the CAB layer and at the center of the large-scale box.

Table 9. Loading protocol for experiment No. 1 (SG and CAB layers).

Load Type	Target Load Amplitude (lb)	Loading Cycles or Loading Rate	Load Plate Diameter (Inch)	Rest Period Between Load Levels (min)
Dynamic load (0.1-s loading plus 0.9-s rest period)	1,000	25 cycles	11.9 (FWD loading plate)	2
Dynamic load (0.1-s loading plus 0.9-s rest period)	2,000	25 cycles	11.9 (FWD loading plate)	2
Dynamic Load (0.1-s loading plus 0.9-s rest period)	3,000	25 cycles	11.9 (FWD loading plate)	2
Dynamic load (0.1-s loading plus 0.9-s rest period)	4,000	25 cycles	11.9 (FWD loading plate)	2
Dynamic load (0.1-s loading plus 0.9-s rest period)	5,000	25 cycles	11.9 (FWD loading plate)	2
Dynamic load (0.1-s loading plus 0.9-s rest period)	6,000	25 cycles	11.9 (FWD loading plate)	2
Dynamic load (0.1-s loading plus 0.9-s rest period)	7,000	25 cycles	11.9 (FWD loading plate)	2
Static load	Up to failure	0.4 inch/min	11.9 (steel plate)	Constant loading rate

The instrumentation for the pavement structure consisted of surface LVDTs installed diagonally to measure surface deflections at various radial distances (0, 8, 12, 24, 36, 48, and 60 inches). The LVDT attachment system was similar to the one used in experiment No. 1 except that the moving tip of the surface LVDTs rested on top of the CAB layer. Nine 4-inch TEPCs were also placed at three locations: in the middle of the CAB and 6 and 20 inches below the SG surface. These cells were located directly under the center of the loading plate and laterally at each of the depth levels at various locations. At the first level (middle of the CAB), there were three sensors, and at the second level (6 inches below SG the surface), there were five. At the bottom level (20 inches below the SG surface), there was one sensor directly under the center of the loading plate. More details on the TEPCs locations can be inferred from figure 53 through figure 56 and table 10.

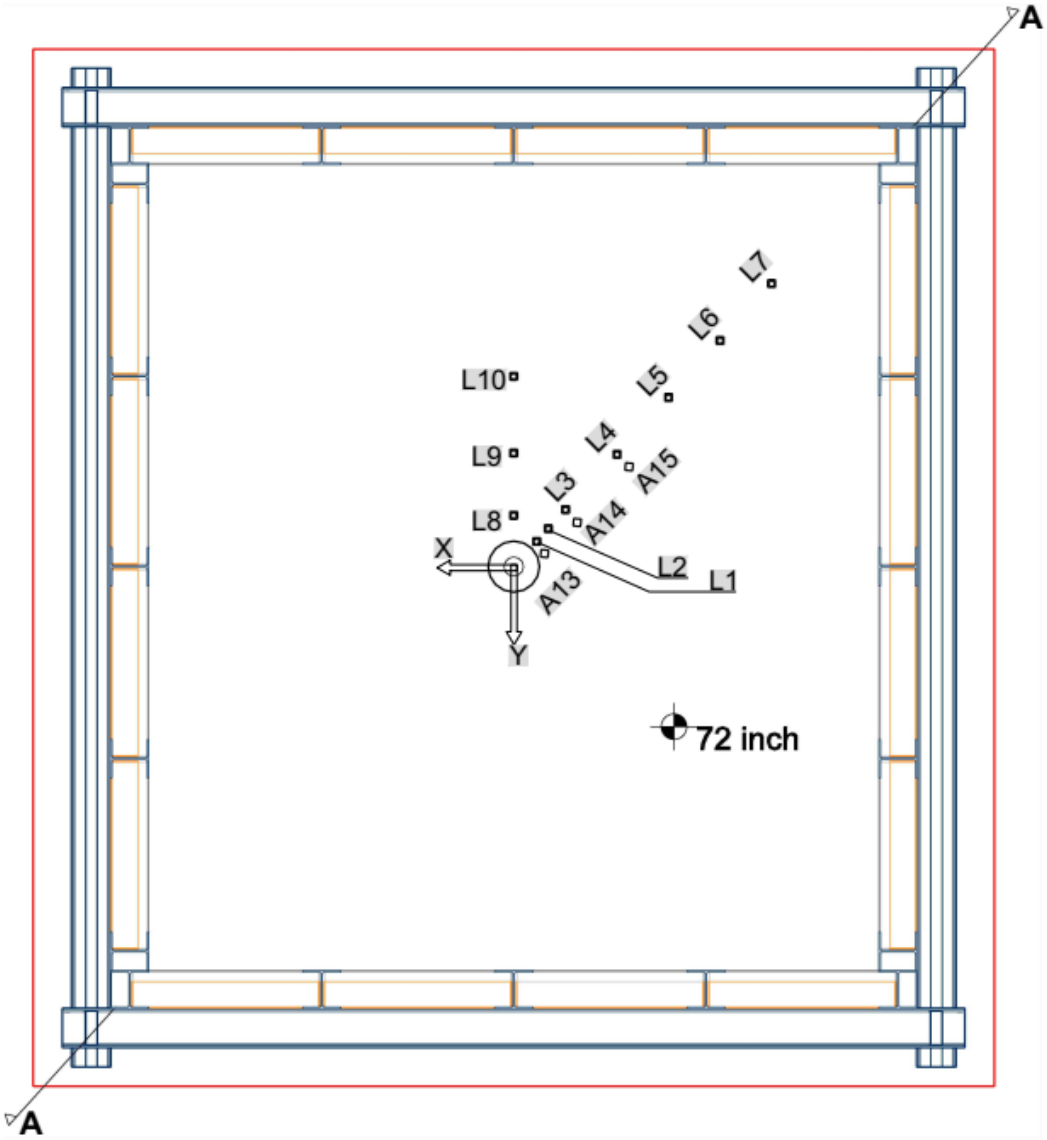

L= LVDT; P = TEPC; A = ACC.

Figure 53. Illustration. Plan view for large-scale-box instrumentations in experiment No. 2.

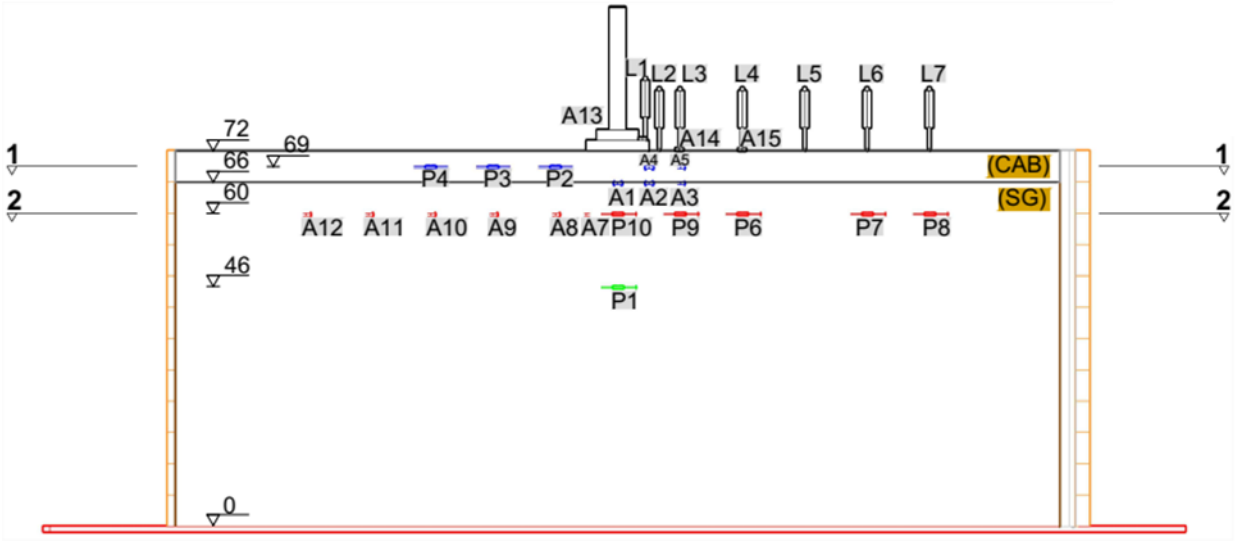

© 2018 UNR.
Note: All elevations are in inches.
L = LVDT; P = TEPC; A = ACC.

Figure 54. Illustration. Section A-A view for large-scale-box instrumentations in experiment No. 2.

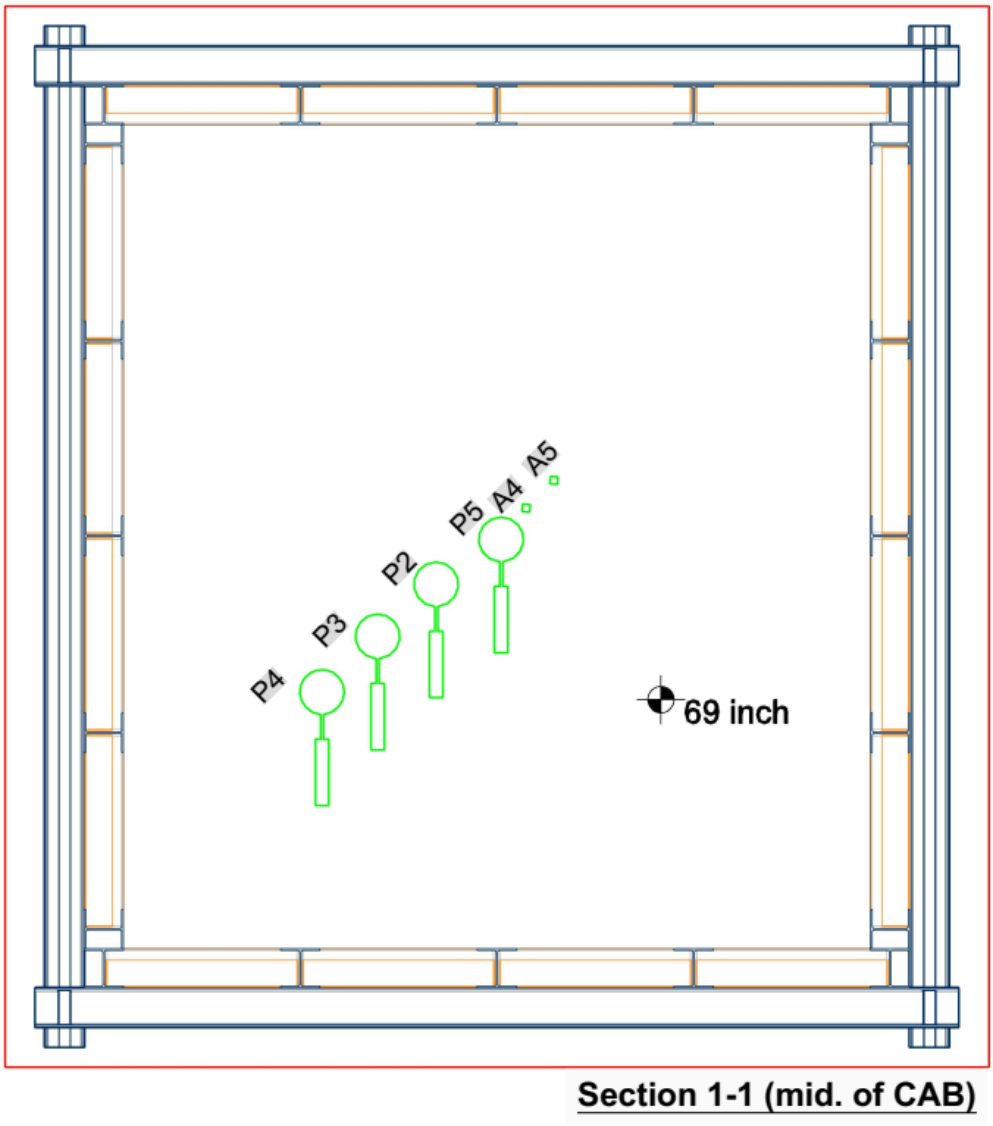

P = TEPC; A = ACC.

Figure 55. Illustration. Section 1-1 view for large-scale-box instrumentations in experiment No. 2.

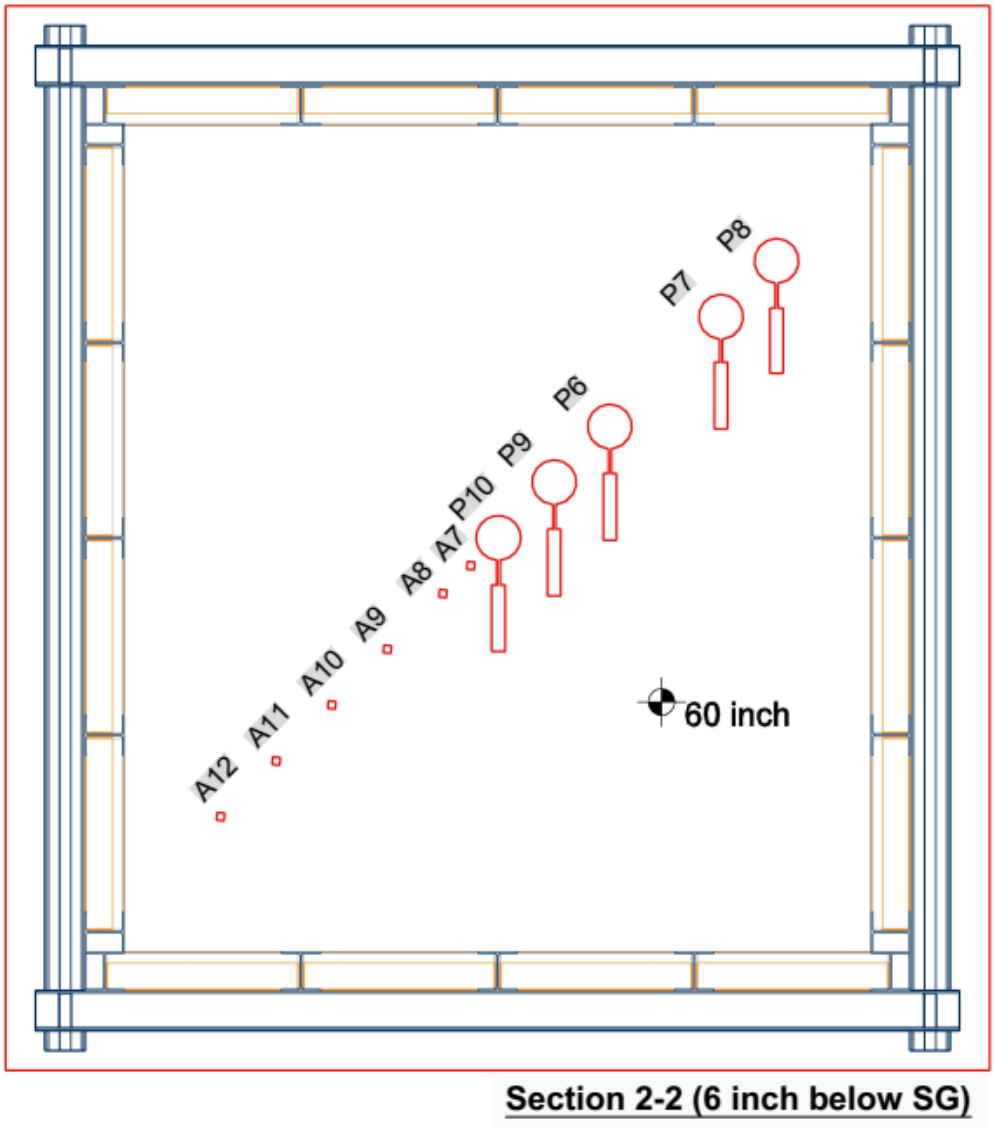

P = TEPC; A = ACC.

Figure 56. Illustration. Section 2-2 view for large-scale-box instrumentations in experiment No. 2.

Table 10. Details of instrumentation plan for experiment No. 2 (SG and CAB layers).

No.	Tag	Sensor Name	Capacity	Specification	Radius (Inch)	Angle (°)	Depth (Inch)	X (Inch)	Y (Inch)	Z (Inch)	Serial Number	No. of Channels	Notes
1	L1	LVDT01	4 inch	TR-0100	0	48	0	0	0	72	—	1	LVDT
2	L2	LVDT02	4 inch	TR-0100	8	48	0	−5.3	−6.0	72	—	1	LVDT
3	L3	LVDT03	4 inch	TR-0100	12	48	0	−8.0	−9.0	72	—	1	LVDT
4	L4	LVDT04	4 inch	TR-0100	24	48	0	−15.9	−17.9	72	—	1	LVDT
5	L5	LVDT05	4 inch	TR-0100	36	48	0	−23.9	−26.9	72	—	1	LVDT
6	L6	LVDT06	4 inch	TR-0100	48	48	0	−31.9	−35.9	72	—	1	LVDT
7	L7	LVDT07	4 inch	TR-0100	60	48	0	−39.9	−44.8	72	—	1	LVDT
8	P1	P01	87 psi	4-inch cell	0	0	26	0	0	46	1404682	1	Pressure cell (vertical)
9	P2	P02	36 psi	4-inch cell	12	228	3	8.0	9.0	69	1330825	1	Pressure cell (vertical)
10	P3	P03	36 psi	4-inch cell	24	228	3	15.9	17.9	69	1330822	1	Pressure cell (vertical)
11	P4	P04	36 psi	4-inch cell	36	228	3	23.9	26.9	69	1330827	1	Pressure cell (vertical)
12	P6	P06	87 psi	4-inch cell	24	48	12	−15.9	−17.9	60	1427206	1	Pressure cell (vertical)
13	P7	P07	87 psi	4-inch cell	48	48	12	−31.9	−35.9	60	1427204	1	Pressure cell (vertical)
14	P8	P08	87 psi	4-inch cell	60	48	12	−39.9	−44.8	60	1427205	1	Pressure cell (vertical)
15	P9	P09	87 psi	4-inch cell	12	48	12	−8.0	−9.0	60	1404681	1	Pressure cell (vertical)
16	P10	P10	145 psi	4-inch cell	0	0	12	0	0	60	1533651	1	Pressure cell (vertical)
17	A1	ACC01	±5 g	3-axis	0	48	6	0	0	66	—	1	ACC
18	A2	ACC02	±5 g	3-axis	6	48	6	−4.0	−4.5	66	—	1	ACC
19	A3	ACC03	±5 g	3-axis	12	48	6	−8.0	−9.0	66	—	1	ACC
20	A4	ACC04	±5 g	3-axis	6	48	3	−4.0	−4.5	69	—	1	ACC
21	A5	ACC05	±5 g	3-axis	12	48	3	−8.0	−9.0	69	—	1	ACC
22	A7	ACC07	±5 g	3-axis	6	228	12	4.0	4.5	60	—	1	ACC
23	A8	ACC08	±5 g	3-axis	12	228	12	8.0	9.0	60	—	1	ACC
24	A9	ACC09	±5 g	3-axis	24	228	12	15.9	17.9	60	—	1	ACC
25	A10	ACC10	±5 g	3-axis	36	228	12	23.9	26.9	60	—	1	ACC
26	A11	ACC11	±5 g	3-axis	48	228	12	31.9	35.9	60	—	1	ACC
27	A12	ACC12	±5 g	3-axis	60	228	12	39.9	44.8	60	—	1	ACC
28	A13	ACC13	±5 g	3-axis	0	0	0	0	0	72	—	1	ACC
29	A14	ACC14	±5 g	3-axis	12	48	0	−8.0	−9.0	72	—	1	ACC
30	A15	ACC15	±5 g	3-axis	24	48	0	−15.9	−17.9	72	—	1	ACC
31	A16	ACC16	±5 g	3-axis	—	—	—	—	—	—	—	1	Frame ACC
32	—	LCST01	—	—	—	—	—	—	—	—	—	1	Applied load-string pod
33	—	LC01	—	—	—	—	—	—	—	—	—	1	Applied load-load cell

—Not applicable.

The sensors were installed after compacting the SG and CAB to the level of the instruments. As outlined in experiment No. 1, the pressure cells were then placed carefully on a leveled surface created by a thin layer of compacted, fine material to ensure full contact with the cell and to facilitate a better bearing surface. After placement of the sensor, additional material was placed carefully on top of the cell and compacted by hand using a steel tamper plate. Figure 57 shows a picture after placement of all pavement layers and instruments.

Figure 57. Photo. Completed large-scale-box test setup for experiment No. 2.

2.8.3. Experiment No. 3 (Full Pavement)

In this experiment, a full pavement structure was constructed with a total thickness of 77 inches. Figure 58 through figure 61 show the drawings of the experiment No. 3 setup. The pavement structure consisted of 5 inches of AC on top of 6 inches of CAB and 66 inches of SG soil. The loads were applied on top of the AC layer.

In experiment No. 3, the full pavement structure was subjected to repeated dynamic loads with amplitudes between 9,000 and 27,000 lb. Twenty-five cycles were applied at each incremental dynamic load with a pulse duration of 0.1 s followed by a rest period of 0.9 s in each loading cycle. The researchers subjected the structure to a series of five loading levels with sequentially higher load amplitudes. No static loading was applied in this experiment. Table 11 summarizes the loading protocol for experiment No. 3. All loads were applied on the loading plate positioned directly at the top of the AC layer and at the center of the large-scale box.

The instrumentation for the pavement structure consisted of surface LVDTs installed diagonally to measure surface deflections at various radial distances (0, 8, 12, 24, 36, 48, and 60 inches). The LVDT attachment system was similar to the one used in experiment No. 1. The moving tip of the surface LVDTs rested on top of the AC layer. In this experiment, three additional LVDTs were used to measure the top deflection of the CAB material through a hole, which was drilled through the AC layer, to provide data that can be used in assessing the deformation of the AC layer only.

Ten 4-inch TEPCs were placed at three locations: in the middle of the CAB and at 6 and 20 inches below the SG surface. These cells were located directly under the center of the loading plate and laterally at each of the depth levels at various locations. At the first level (middle of the CAB), there were four sensors, and at the second level (6 inches below the SG surface), there were five. At the bottom level (20 inches below the SG surface), there was one sensor directly under the center of the loading plate. More details on the TEPCs can be inferred from figure 58 through figure 61 and table 12. The sensors were installed after compacting the SG and CAB to the level of the instruments. As noted in experiments No. 1 and No. 2, the TEPCs were placed carefully on a leveled surface created by a thin layer of compacted, fine material to ensure full contact with the cell and to facilitate a better bearing surface. After placement of the sensor, additional material was placed carefully on top of the cell and compacted by hand using a steel tamper plate.

AC strain gauges were also placed at the bottom of the AC layer to capture the strains of the pavement under the dynamic and static loading. A small amount of a fine-graded asphalt mixture was placed over the CAB to ensure a proper support for the strain gauge and a good bond between the strain gauge and the AC layer. Once the strain gauge was placed, a steel plate was placed on top, and static pressure was used to compact the gauge into the asphalt patch. The asphalt mixture was then placed directly over the strain gauge. Figure 62 shows the asphalt strain gauges on top of the compacted CAB layer prior to adding the fine-graded asphalt mixture. Figure 63 shows a picture after placement of all pavement layers and instruments.

Table 11. Loading protocol for experiment No. 3 (full pavement structure).

Load Type	Target Load Amplitude (lb)	Loading Cycles	Load Plate Diameter (Inch)	Rest Period Between Load Levels (min)
Dynamic load (0.1-s loading plus 0.9-s rest period)	9,000	25	11.9 (FWD loading plate)	2
Dynamic load (0.1-s loading plus 0.9-s rest period)	12,000	25	11.9 (FWD loading plate)	2
Dynamic load (0.1-s loading plus 0.9-s rest period)	16,000	25	11.9 (FWD loading plate)	2
Dynamic load (0.1-s loading plus 0.9-s rest period)	21,000	25	11.9 (FWD loading plate)	2
Dynamic load (0.1-s loading plus 0.9-s rest period)	27,000	25	11.9 (FWD loading plate)	2

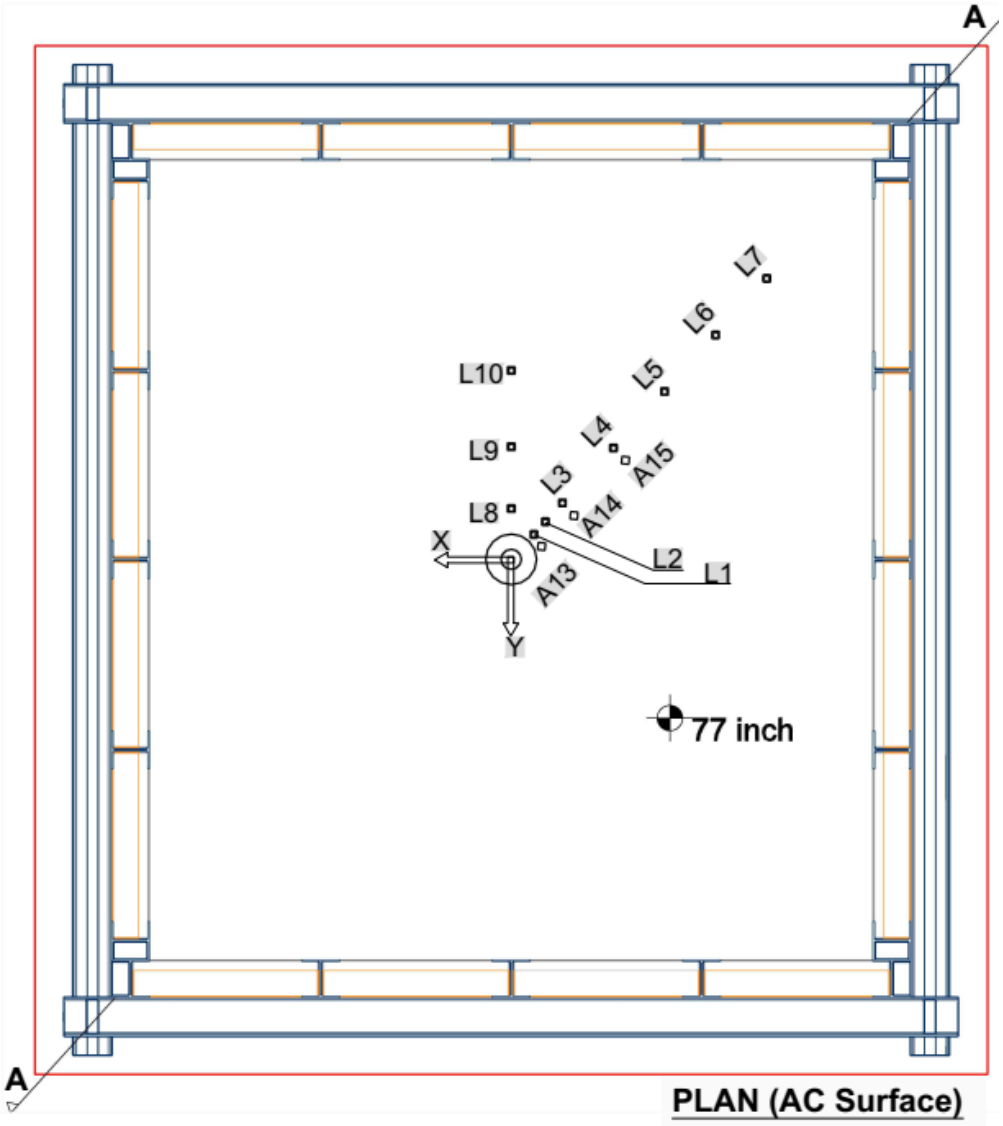

L = LVDT; A = ACC.

Figure 58. Illustration. Plan view for large-scale-box instrumentations in experiment No. 3.

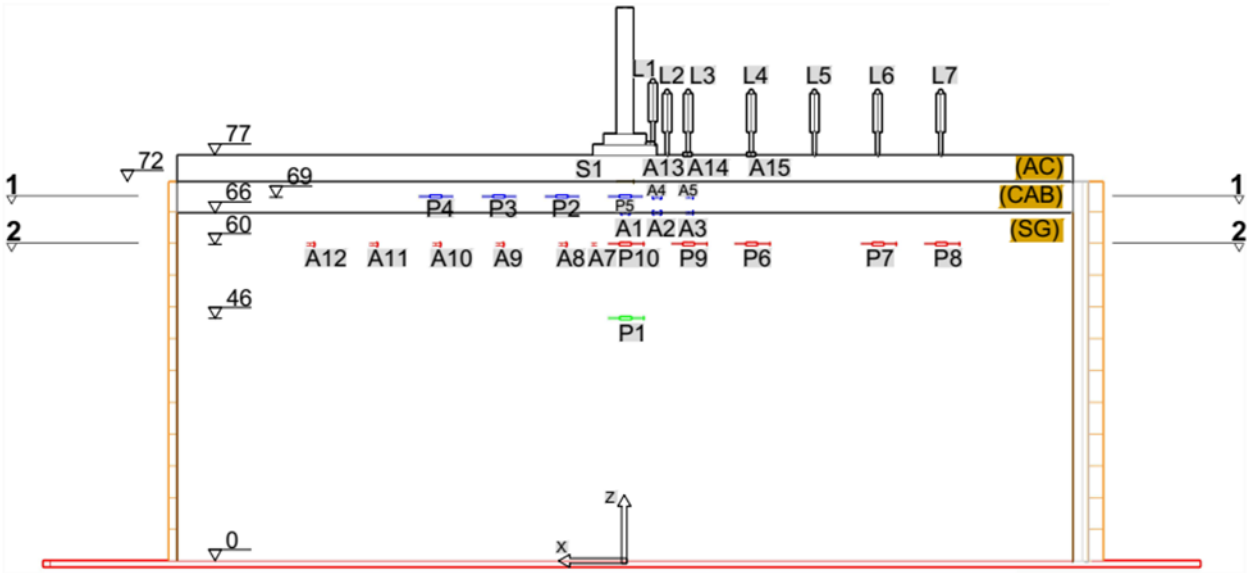

Note: All elevations are in inches.
L = LVDT; P = TEPC; A = ACC.

Figure 59. Illustration. Section A-A view for large-scale-box instrumentations in experiment No. 3.

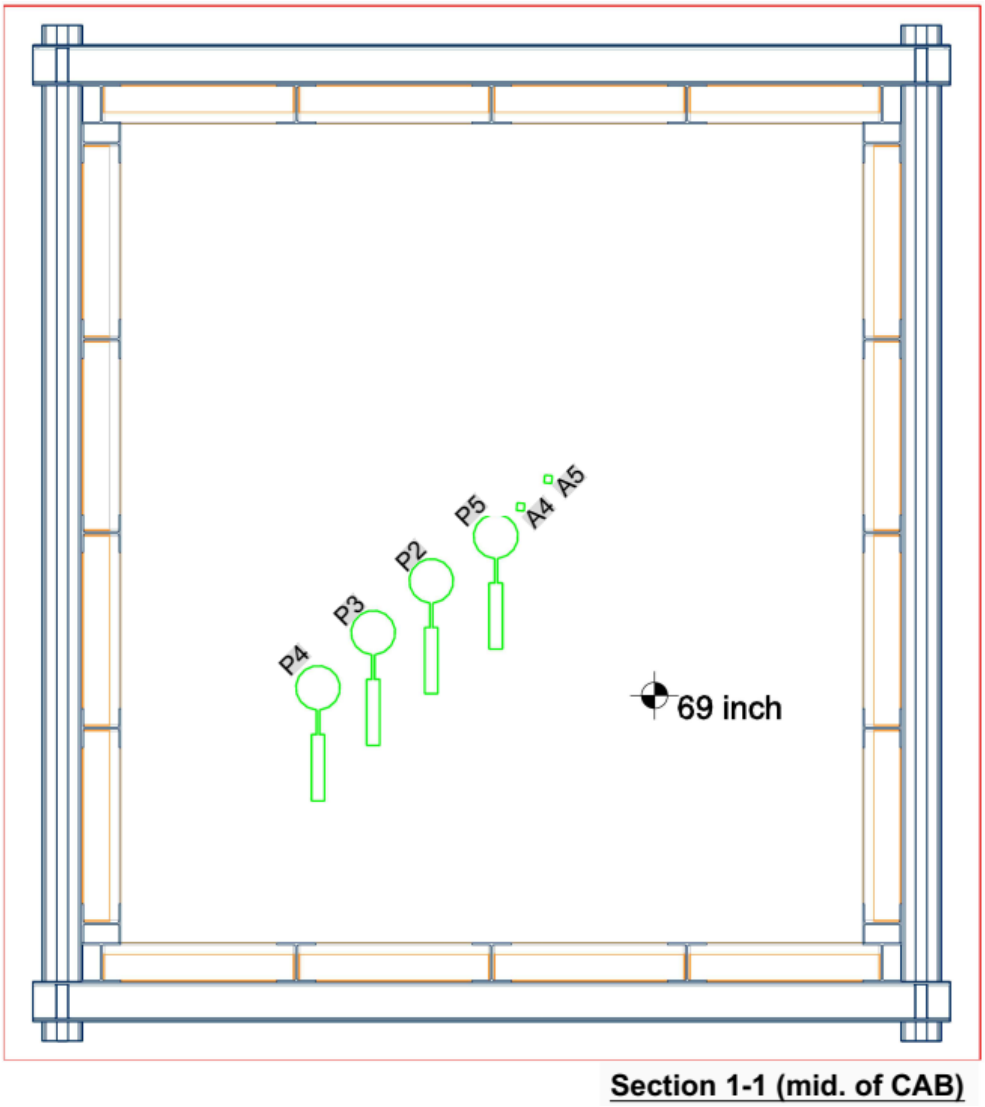

P = TEPC; A = ACC.

Figure 60. Illustration. Section 1-1 view for large-scale-box instrumentations in experiment No. 3.

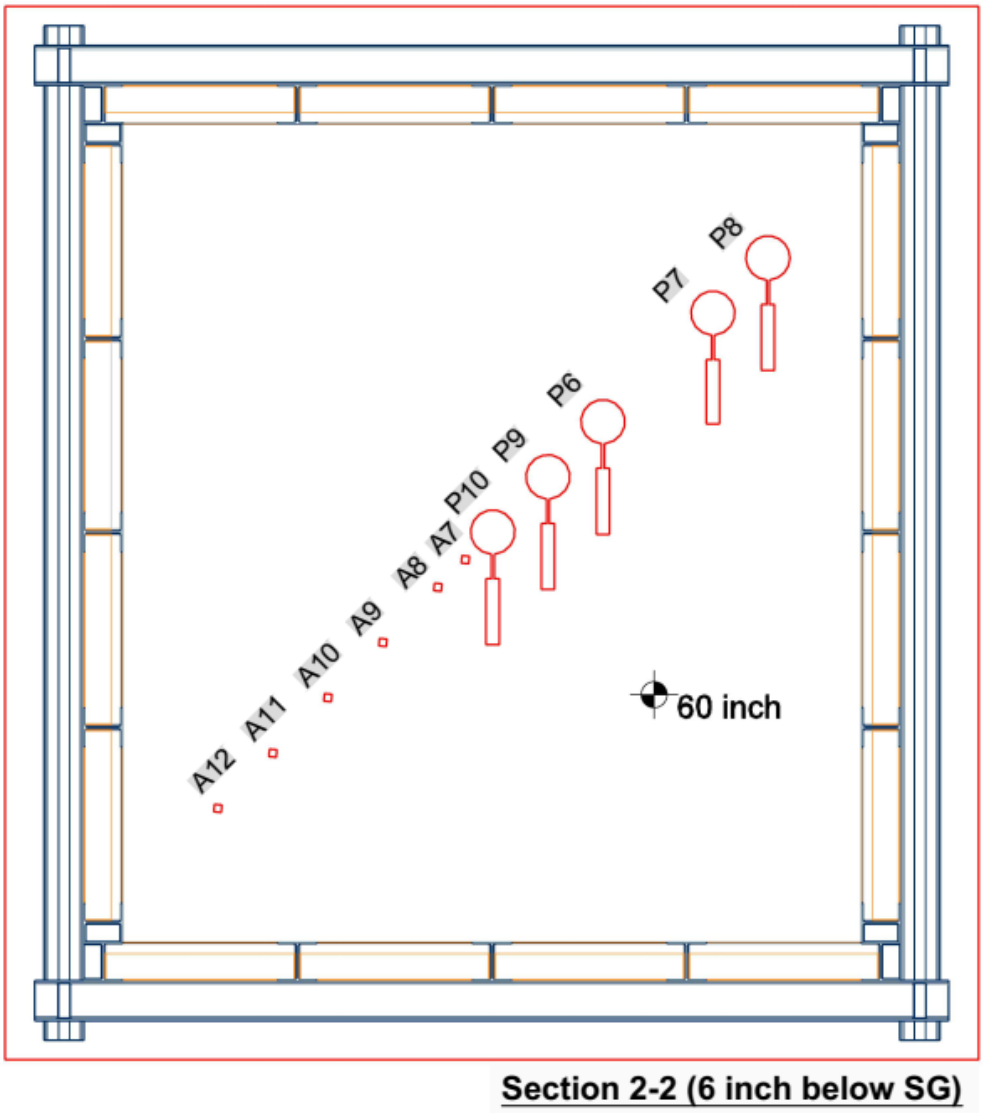

P = TEPC; A = ACC.

Figure 61. Illustration. Section 2-2 view for large-scale-box instrumentations in experiment No. 3.

Table 12. Details of instrumentation plan for experiment No. 3 (full pavement structure).

No.	Tag	Sensor Name	Capacity	Specification	Radius (Inch)	Angle (°)	Depth (Inch)	X (Inch)	Y (Inch)	Z (Inch)	ID/SN	No. of Channels	Notes
1	L1	LVDT01	4 inch	TR-0100	0	48	0	0	0	77	—	1	LVDT
2	L2	LVDT02	4 inch	TR-0100	8	48	0	−5.3	−6.0	77	—	1	LVDT
3	L3	LVDT03	4 inch	TR-0100	12	48	0	−8.0	−9.0	77	—	1	LVDT
4	L4	LVDT04	4 inch	TR-0100	24	48	0	−15.9	−17.9	77	—	1	LVDT
5	L5	LVDT05	4 inch	TR-0100	36	48	0	−23.9	−26.9	77	—	1	LVDT
6	L6	LVDT06	4 inch	TR-0100	48	48	0	−31.9	−35.9	77	—	1	LVDT
7	L7	LVDT07	4 inch	TR-0100	60	48	0	−39.9	−44.8	77	—	1	LVDT
8	L8	LVDT08	4 inch	TR-0100	8	90	5	0	−8.0	72	—	1	LVDT
9	L9	LVDT09	4 inch	TR-0100	12	90	5	0	−12.0	72	—	1	LVDT
10	L10	LVDT010	4 inch	TR-0100	24	90	5	0	−24.0	72	—	1	LVDT
11	P1	P01	87 psi	4-inch cell	0	0	31	0	0	46	1404682	1	TEPC (vertical)
12	P2	P02	36 psi	4-inch cell	12	228	8	8.0	9.0	69	1330825	1	TEPC (vertical)
13	P3	P03	36 psi	4-inch cell	24	228	8	15.9	17.9	69	1330822	1	TEPC (vertical)
14	P4	P04	36 psi	4-inch cell	36	228	8	23.9	26.9	69	1330827	1	TEPC (vertical)
15	P5	P05	362 psi	4-inch cell	0	0	8	0	0	69	1533652	1	TEPC (vertical)
16	P6	P06	87 psi	4-inch cell	24	48	17	−15.9	−17.9	60	1427206	1	TEPC (vertical)
17	P7	P07	87 psi	4-inch cell	48	48	17	−31.9	−35.9	60	1427204	1	TEPC (vertical)
18	P8	P08	87 psi	4-inch cell	60	48	17	−39.9	−44.8	60	1427205	1	TEPC (vertical)
19	P9	P09	87 psi	4-inch cell	12	48	17	−8.0	−9.0	60	1404681	1	TEPC (vertical)
20	P10	P10	145 psi	4-inch cell	0	0	17	0	0	60	1533651	1	TEPC (vertical)
21	A1	ACC01	±5 g	3-axis	0	48	11	0	0	66	—	1	ACC
22	A2	ACC02	±5 g	3-axis	6	48	11	−4.0	−4.5	66	—	1	ACC
23	A3	ACC03	±5 g	3-axis	12	48	11	−8.0	−9.0	66	—	1	ACC
24	A4	ACC04	±5 g	3-axis	6	48	8	−4.0	−4.5	69	—	1	ACC
25	A5	ACC05	±5 g	3-axis	12	48	8	−8.0	−9.0	69	—	1	ACC
26	A7	ACC07	±5 g	3-axis	6	228	17	4.0	4.5	60	—	1	ACC
27	A8	ACC08	±5 g	3-axis	12	228	17	8.0	9.0	60	—	1	ACC
28	A9	ACC09	±5 g	3-axis	24	228	17	15.9	17.9	60	—	1	ACC
29	A10	ACC10	±5 g	3-axis	36	228	17	23.9	26.9	60	—	1	ACC
30	A11	ACC11	±5 g	3-axis	48	228	17	31.9	35.9	60	—	1	ACC
31	A12	ACC12	±5 g	3-axis	60	228	17	39.9	44.8	60	—	1	ACC
32	A13	ACC13	±5 g	3-axis	0	0	0	0	0	77	—	1	ACC
33	A14	ACC14	±5 g	3-axis	12	48	0	−8.0	−9.0	77	—	1	ACC
34	A15	ACC15	±5 g	3-axis	24	48	0	−15.9	−17.9	77	—	1	ACC
35	A16	ACC16	±5 g	3-axis	—	—	—	—	—	—	—	1	Frame ACC
36	—	LCST01	—	—	—	—	—	—	—	—	—	1	Applied load-string pod
37	—	LC01	—	—	—	—	—	—	—	—	—	1	Applied load-load cell
38	S1	S1	—	—	0	0	5	0	0	72	—	1	AC strain gauge

—Not applicable.

Figure 62. Photo. Asphalt strain gauges placed on top of the CAB.

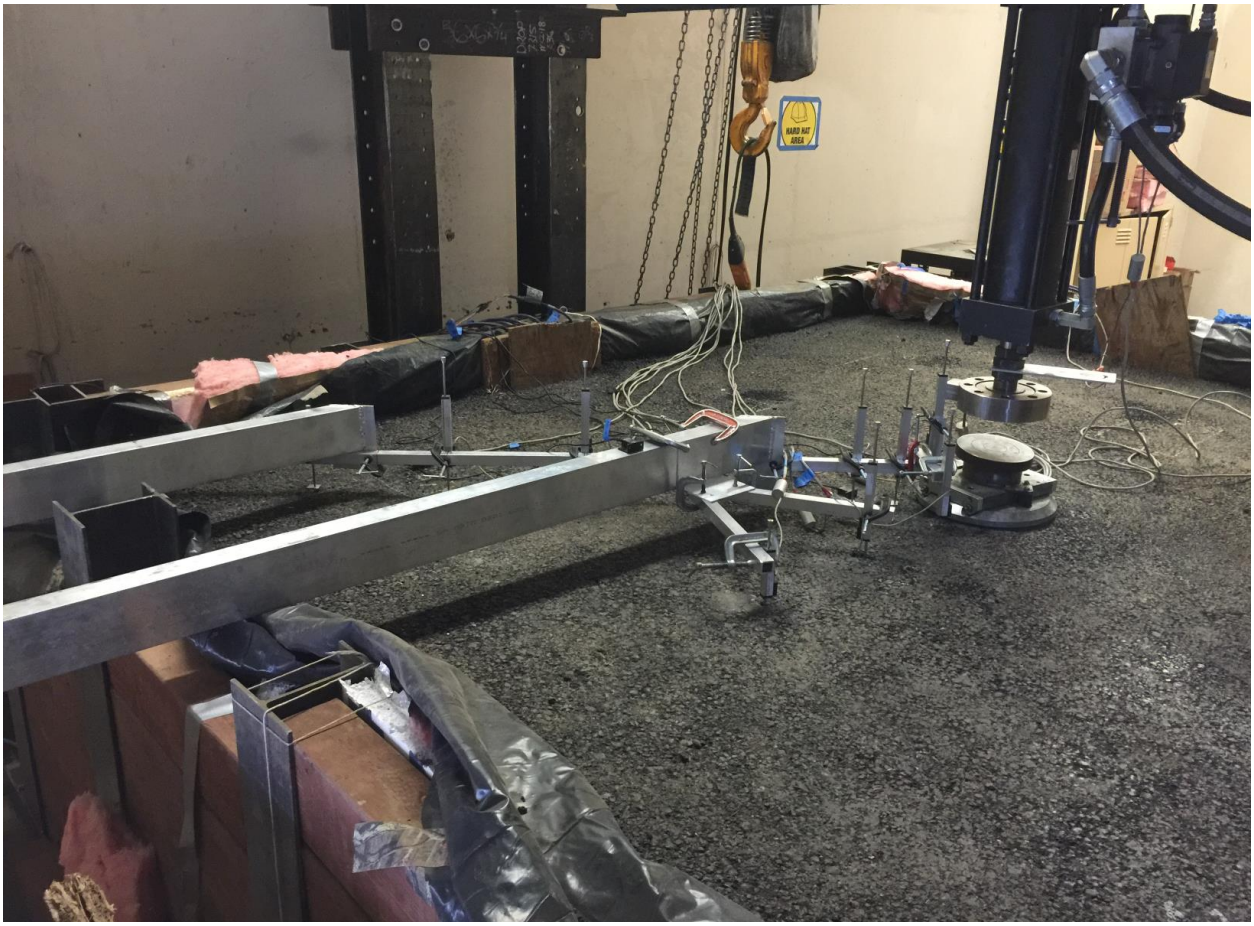

Figure 63. Photo. Completed large-scale-box test setup for experiment No. 3.

2.8.4. Experiment No. 4 (Full Pavement With Sloping Edge)

In this experiment, a full pavement structure with a total thickness of 77 inches was constructed with a side slope of 1:1.5 (33.7 degrees with the ground). Figure 64 through figure 70 show drawings of the experiment No. 4 setup. The pavement structure consisted of 5 inches of AC on top of 6 inches of CAB and 66 inches of SG soil. The loads were applied on top of the AC layer at three locations: 12, 24, and 36 inches from the edge of the slope.

In experiment No. 4, the full pavement structure with sloping edge was subjected to repeated dynamic loads with amplitudes between 9,000 and 27,000 lb at different load increments. Twenty-five cycles were applied at each incremental dynamic load with a pulse duration of 0.1 s followed by a rest period of 0.9 s in each loading cycle. The researchers subjected the structure to a series of five loading levels with sequentially higher load amplitudes. Table 13 summarizes the loading protocol for experiment No. 4. All loads were applied on the loading plate positioned directly at the top of the AC layer but at three different locations along the centerline of the large-scale box: 12, 24, and 36 inches offset from the edge of the slope. The test series started from the third location, which is the farthest away from the slope and progressively moved closer to the edge.

Table 13. Loading protocol for experiment No. 4 (full pavement with sloping edge).

Load Type	Target Load Amplitude (lb)	Loading Cycles or Loading Rate	Load Plate Diameter (Inch)	Rest Period Between Load Levels (min)
Dynamic load (0.1-s loading plus 0.9-s rest period)	9,000	25 cycles	11.9 (FWD loading plate)	2
Dynamic load (0.1-s loading plus 0.9-s rest period)	12,000	25 cycles	11.9 (FWD loading plate)	2
Dynamic load (0.1-s loading plus 0.9-s rest period)	16,000	25 cycles	11.9 (FWD loading plate)	2
Dynamic load (0.1-s loading plus 0.9-s rest period)	21,000	25 cycles	11.9 (FWD loading plate)	2
Dynamic load (0.1-s loading plus 0.9-s rest period)	27,000	25 cycles	11.9 (FWD loading plate)	2
Static load	Up to failure	0.4 inch/min	11.9 (steel plate)	Constant loading rate

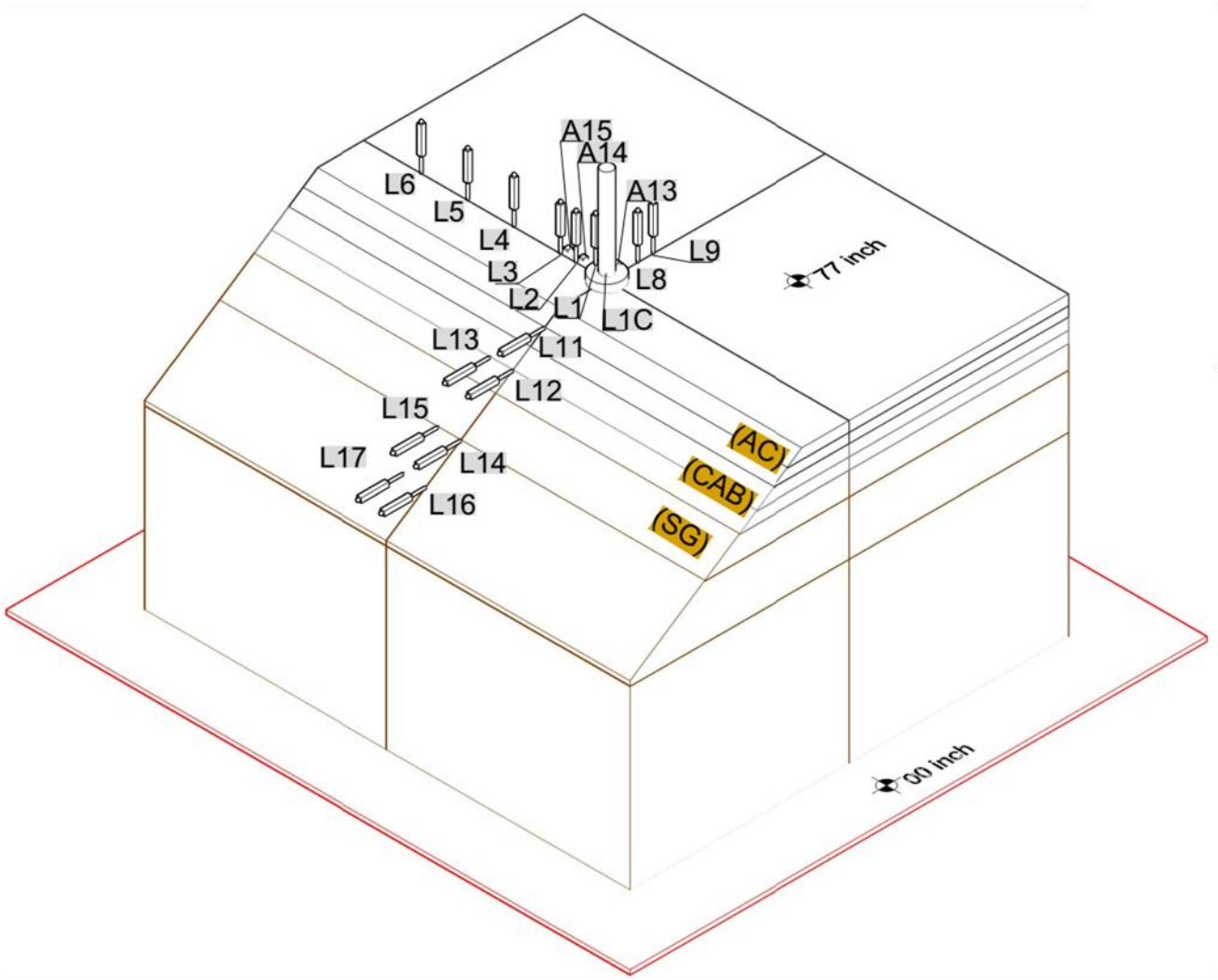

L = LVDT; A = ACC.

Figure 64. Illustration. Three-dimensional view of large-scale-box instrumentations in experiment No. 4 (elevation of 77 inches).

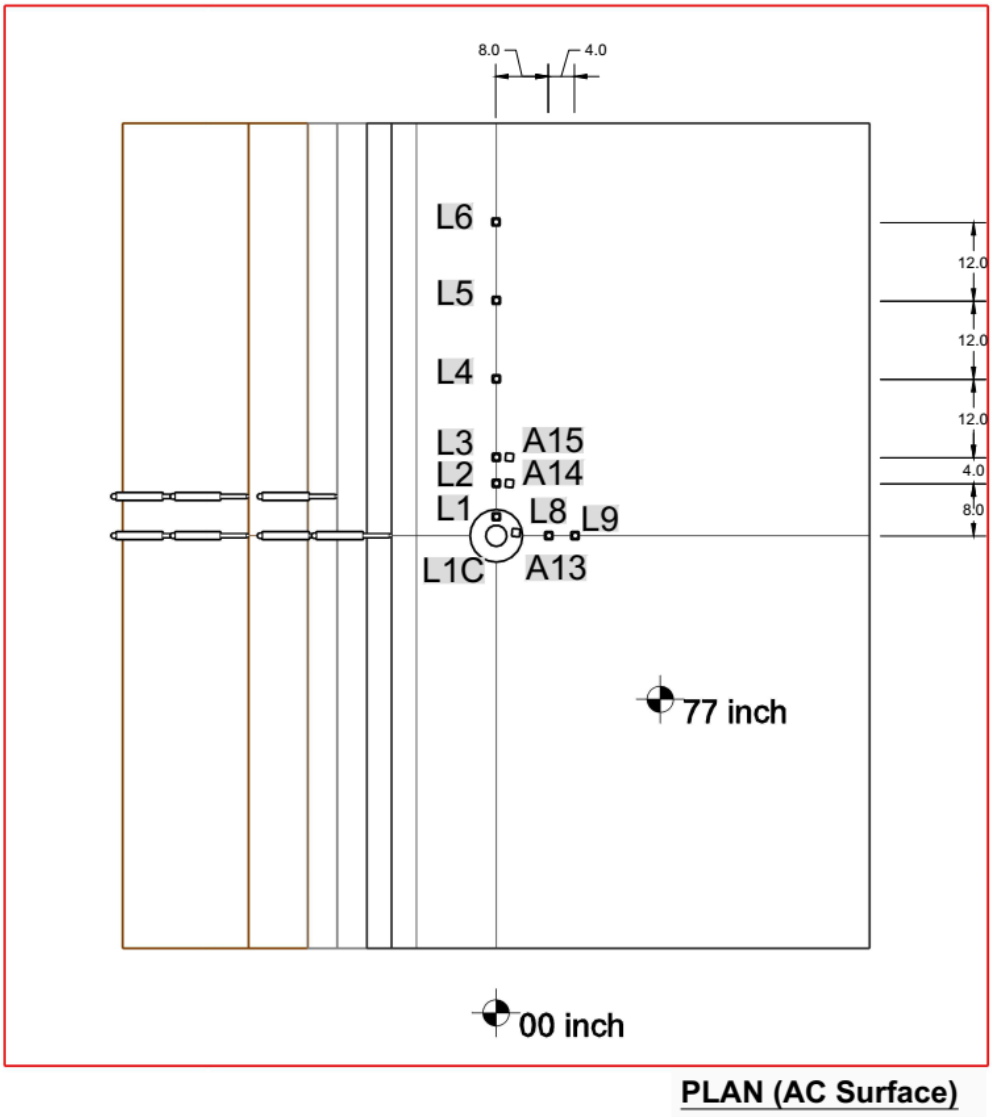

Note: All dimensions are in inches.
L = LVDT; A = ACC.

Figure 65. Illustration. Plan view for large-scale-box instrumentations in experiment No. 4 (elevation of 77 inches).

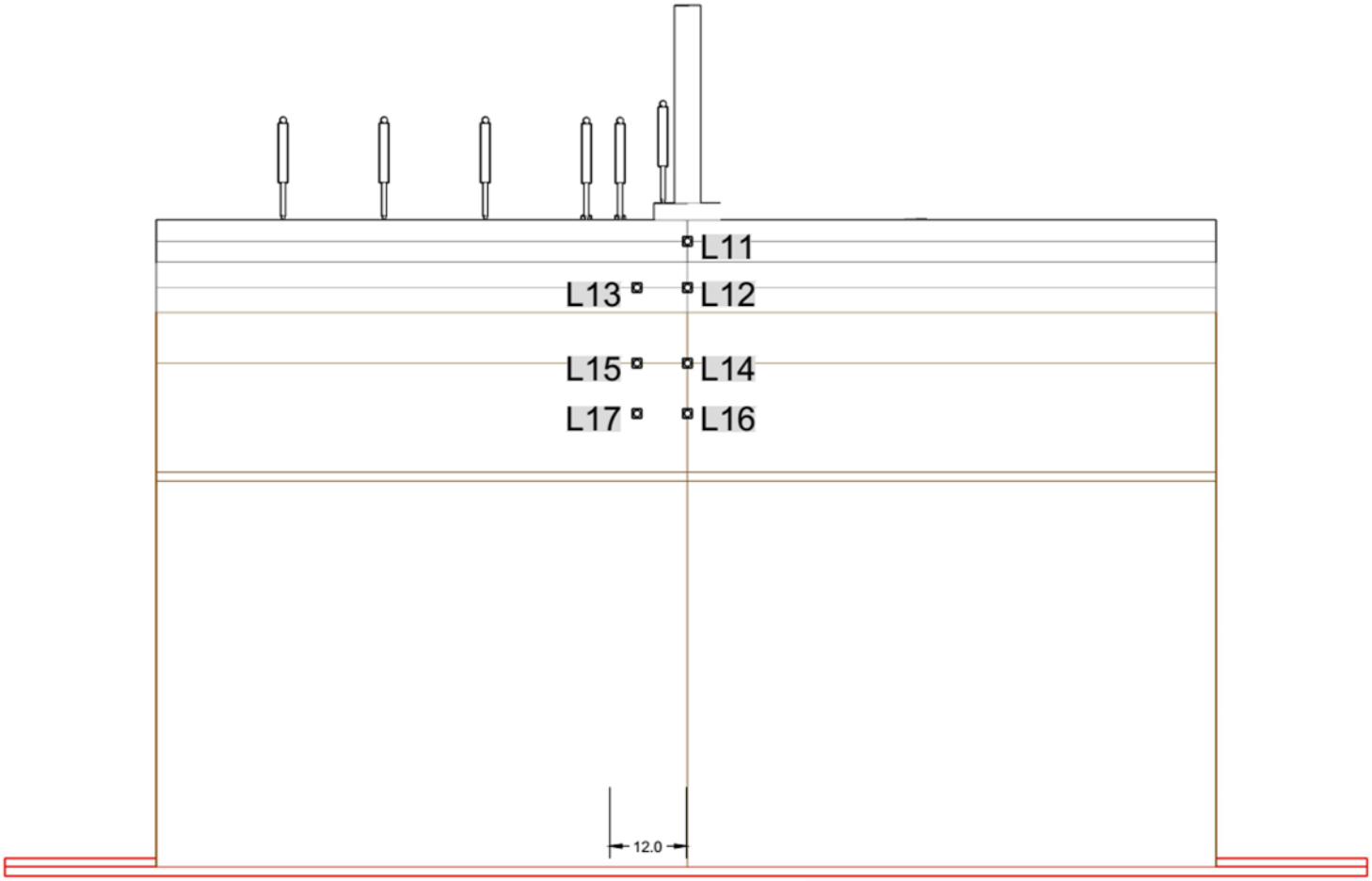

Note: All dimensions are in inches.
L = LVDT.

Figure 66. Illustration. Front elevation of large-scale-box instrumentations in experiment No. 4 (elevation of 77 inches).

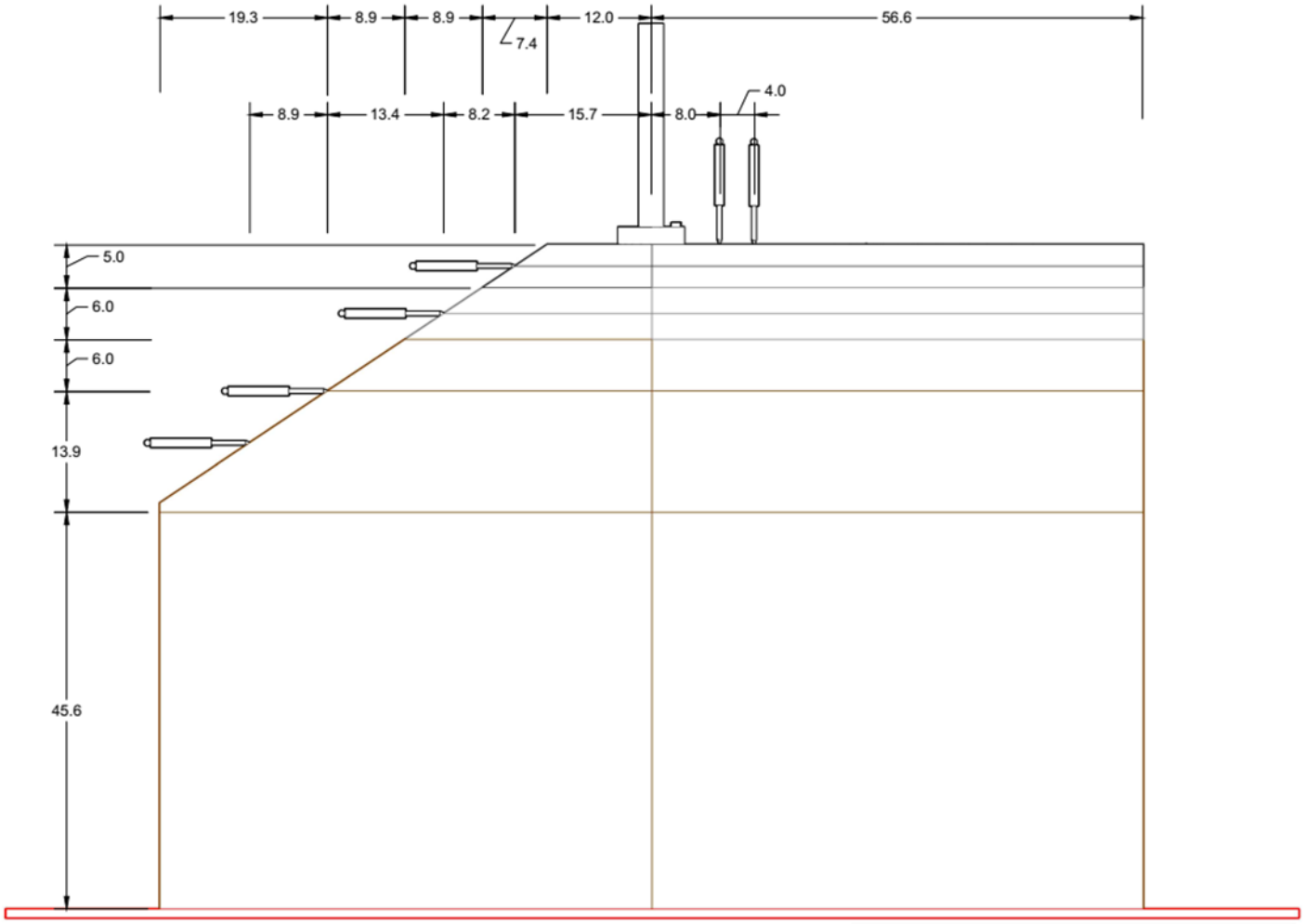

Note: All dimensions are in inches.

Figure 67. Illustration. Side elevation of large-scale-box instrumentations in experiment No. 4 (elevation of 77 inches).

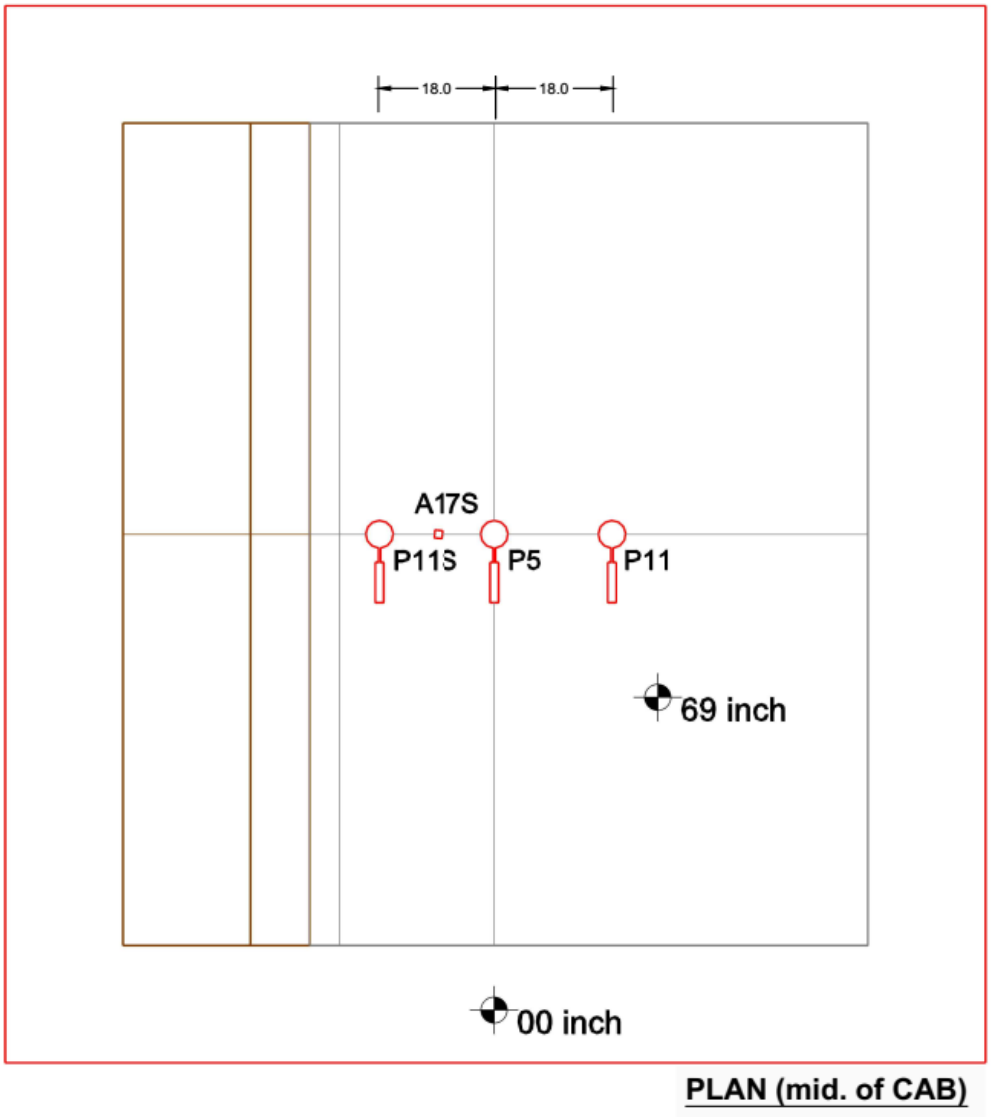

Note: All dimensions are in inches.
P = TEPC; A = ACC.

Figure 68. Illustration. Plan view of large-scale-box instrumentations in experiment No. 4 (elevation of 69 inches).

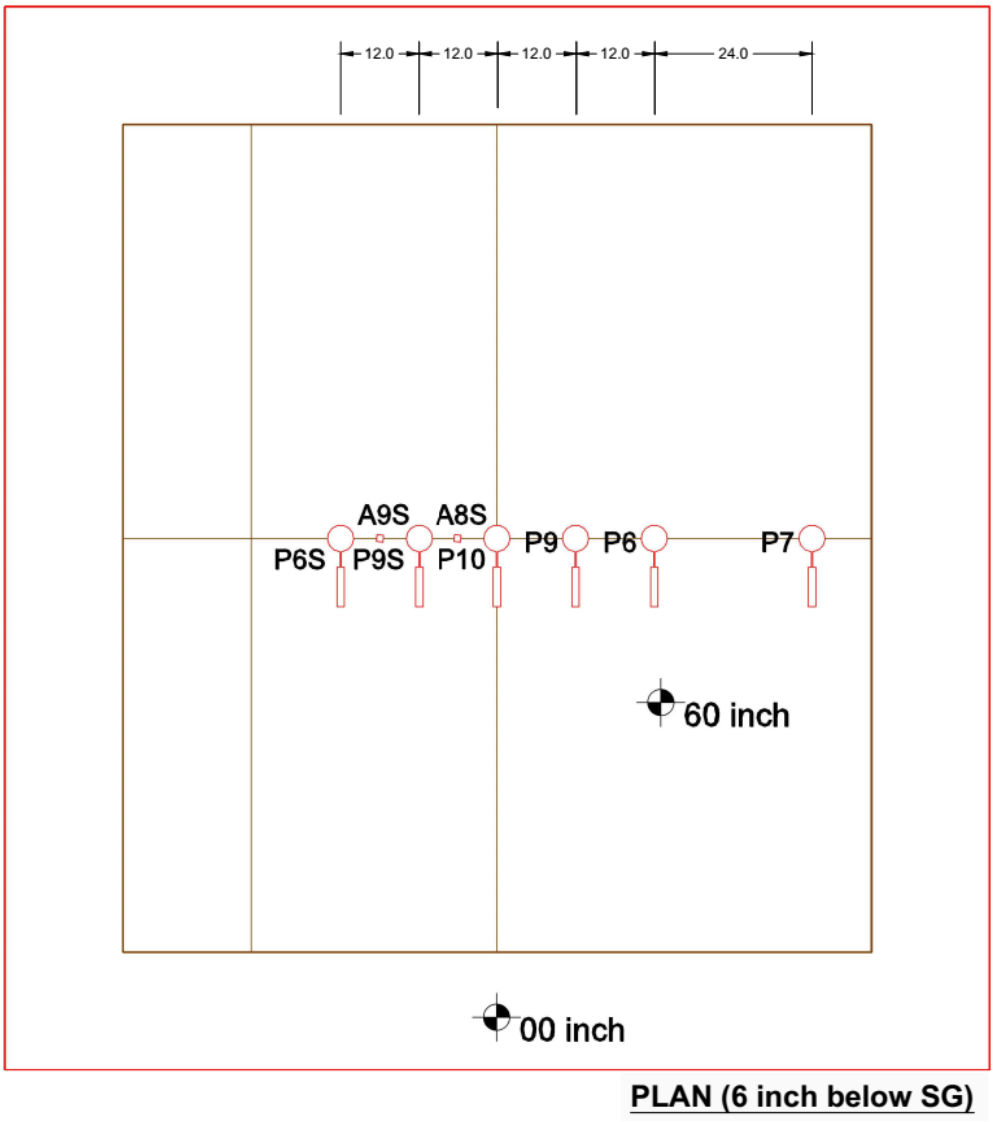

Note: All dimensions are in inches.
P = TEPC; A = ACC.

Figure 69. Illustration. Plan view of large-scale-box instrumentations in experiment No. 4 (elevation of 60 inches).

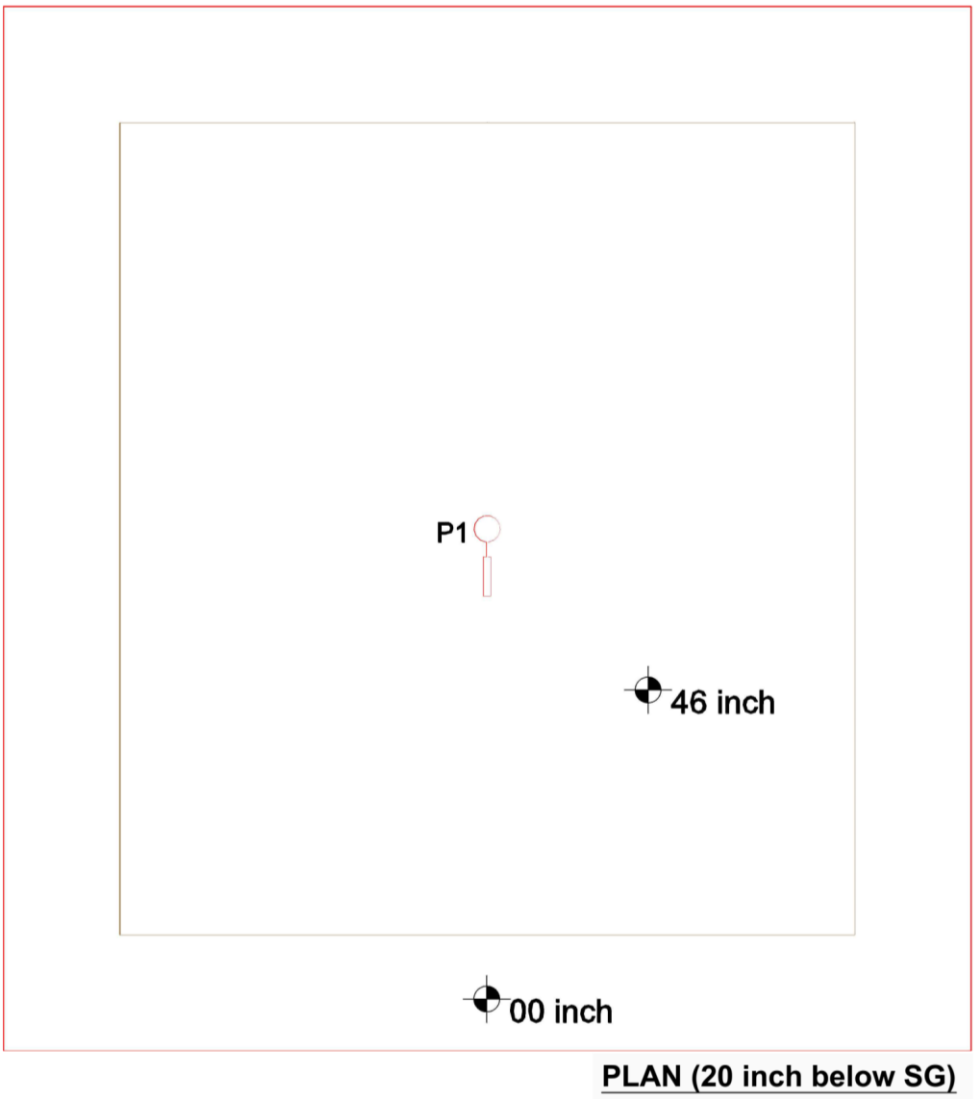

P = TEPC.

Figure 70. Illustration. Plan view of large-scale-box instrumentations in experiment No. 4 (elevation of 46 inches).

Table 14. Details of the instrumentation plan for experiment No. 4 (full pavement with sloping edge).

No.	Tag	Sensor Name	Capacity	Specification	Radius (Inch)	Angle (°)	Depth (Inch)	X (Inch)	Y (Inch)	Z (Inch)	Serial Number	No. of Channels	Notes
1	L1C	LVDT1C	1 inch	TR-0025	0	0	0	0	0	77	—	1	Center LVDT
2	L1	LVDT01	4 inch	TR-0100	0	0	0	0	0	77	—	1	LVDT
3	L2	LVDT02	4 inch	TR-0100	8	90	0	0	−8.0	77	—	1	LVDT
4	L3	LVDT03	4 inch	TR-0100	12	90	0	0	−12.0	77	—	1	LVDT
5	L4	LVDT04	4 inch	TR-0100	24	90	0	0	−24.0	77	—	1	LVDT
6	L5	LVDT05	4 inch	TR-0100	36	90	0	0	−36.0	77	—	1	LVDT
7	L6	LVDT06	4 inch	TR-0100	48	90	0	0	−48.0	77	—	1	LVDT
8	L8	LVDT08	4 inch	TR-0100	8	0	0	−8.0	0	77	—	1	LVDT
9	L9	LVDT09	4 inch	TR-0100	12	0	0	−12.0	0	77	—	1	LVDT
10	L11	LVDT11	4 inch	TR-0100	—	—	2.5	15.7	0	74.5	—	1	Slope LVDT (lateral)
11	L12	LVDT12	4 inch	TR-0100	—	—	8	23.9	0	69	—	1	Slope LVDT (lateral)
12	L13	LVDT13	4 inch	TR-0100	—	—	8	23.9	12.0	69	—	1	Slope LVDT (lateral)
13	L14	LVDT14	4 inch	TR-0100	—	—	17	37.3	0	60	—	1	Slope LVDT (lateral)
14	L15	LVDT15	4 inch	TR-0100	—	—	17	37.3	12.0	60	—	1	Slope LVDT (lateral)
15	L16	LVDT16	4 inch	TR-0100	—	—	23	46.2	0	54	—	1	Slope LVDT (lateral)
16	L17	LVDT17	4 inch	TR-0100	—	—	23	46.2	12.0	54	—	1	Slope LVDT (lateral)
17	P5	P05	362 psi	4-inch cell	0	0	8	0	0	69	1533652	1	Pressure cell (vertical)
18	P6	P06	87 psi	4-inch cell	24	0	17	−24.0	0	60	1427206	1	Pressure cell (vertical)
19	P7	P07	87 psi	4-inch cell	48	0	17	−48.0	0	60	1427204	1	Pressure cell (vertical)
20	P9	P09	87 psi	4-inch cell	12	0	17	−12.0	0	60	1404681	1	Pressure cell (vertical)
21	P10	P10	145 psi	4-inch cell	0	0	17	0	0	60	1533651	1	Pressure cell (vertical)
22	P6S	P06S	87 psi	4-inch cell	24	180	17	24.0	0	60	1427206	1	Pressure cell (slope)
23	P9S	P09S	87 psi	4-inch cell	12	180	17	12.0	0	60	1404681	1	Pressure cell (slope)
24	P11	P11	87 psi	4-inch cell	18	0	8	−18.0	0	69	—	1	Pressure cell (vertical)
25	P11S	P11S	87 psi	4-inch cell	18	180	8	18.0	0	69	—	1	Pressure cell (slope)
26	A8S	ACC08S	±5 g	3-axis	6	0	17	6.0	0	60	—	1	ACC (slope)
27	A9S	ACC09S	±5 g	3-axis	18	0	17	18.0	0	60	—	1	ACC (slope)
28	A13	ACC13	±5 g	3-axis	0	0	0	0	0	77	—	1	ACC
29	A14	ACC14	±5 g	3-axis	12	90	0	0	−12.0	77	—	1	ACC
30	A15	ACC15	±5 g	3-axis	24	90	0	0	−24.0	77	—	1	ACC
31	A16	ACC16	±5 g	3-axis	—	—	—	—	—	—	—	1	Frame ACC
32	A17S	ACC17S	±5 g	3-axis	9	0	17	9.0	0	60	—	1	ACC (slope)
33	—	LCST01	—	—	—	—	—	—	—	—	—	1	Applied load-string pod
34	—	LC01	—	—	—	—	—	—	—	—	—	1	Applied load-load cell
35	S1	S1	—	—	0	0	5	0	0	72	—	1	AC strain gauge

—Not applicable.

At the end of the dynamic load testing, the pavement structure was allowed to recover for 30 min. An increasing static load was then applied up to failure with a constant settlement rate of 0.4 inch/min. The static load was applied on the loading plate positioned directly at the top of the AC layer and 12 inches from the edge of the slope.

The instrumentation for the pavement structure consisted of surface LVDTs installed along the edge of the pavement to measure surface deflections at various radial distances (0, 8, 12, 24, 36, and 48 inches). Two additional LVDTs were used to measure the top deflection of the AC material in the direction perpendicular to the pavement edge (figure 64 and figure 65). Seven other LVDTs were placed laterally to measure the slope horizontal deflections. These LVDTs were placed at the middle of the AC layer, middle of the CAB layer, and 6 and 12 inches below the SG surface.

Ten 4-inch TEPCs were placed at three locations: the middle of the CAB and 6 and 20 inches below the SG surface. These cells were located directly under the center of the loading plate and laterally at each of the depth levels at various locations. At the first level (middle of the CAB), there were three sensors, and at the second level (6 inches below the SG surface), there were six. At the bottom level (20 inches below the SG surface), there was one sensor directly under the center of the loading plate. More details on the TEPCs locations can be inferred from figure 64 through figure 70 and table 14.

The sensors were installed after compacting the SG and CAB to the level of the instruments. As noted in the previous experiments, the pressure cells were then placed carefully on a leveled surface created by a thin layer of compacted, fine material to ensure full contact with the cell and to facilitate a better bearing surface. After placement of the sensor, additional material was placed carefully on top of the cell and compacted by hand using a steel tamper plate. Figure 71 shows a picture after placement of all pavement layers and instruments.

Figure 71. Photo. Completed large-scale-box test setup for experiment No. 4.

2.8.5. Experiment No. 5 (Full Pavement With Buried Utilities)

In experiment No. 5, a full pavement structure with a total thickness of 77 inches was constructed with two types of buried utilities in the SG layer: a steel pipe and a concrete box culvert. The steel pipe and the concrete box culvert represent a flexible and a rigid buried utility, respectively. Figure 72 through figure 79 show drawings of the setup and instrumentations for experiment No. 5. The pavement structure consisted of 5 inches of AC on top of 6 inches of CAB and 66 inches of SG soil. The loads were applied on top of the AC layer at two locations along the centerline of each of the buried utilities. The centerlines of both buried utilities (i.e., steel pipe and concrete box culvert) were located at 24 inches from the center of the large-scale box in the opposite directions. The following sections discuss the steps involved in selecting the buried utilities

Selection of Flexible Pipe

By definition, a flexible pipe is able to withstand at least a 2-percent deflection ratio (normalized with respect to the size) without any significant structural distress. These pipes are typically made of steel, ductile iron, polyethylene, or PVC. The research team decided to utilize a steel pipe in the experiment and use industry-standard foil strain gauges to measure the strain induced in the pipe wall that was essential to the analysis. These gauges captured the longitudinal and transverse strains induced in the pipe wall.

To select the diameter and wall thickness, a series of analyses was undertaken. These analyses included calculating the pipe ovality, circumferential stress, ring buckling stress, and wall-crushing stress due to loading. These design parameters were assessed due to vertical stresses directly on top of the pipe. Five dynamic surface load levels were used in the analyses. These load levels ranged between 9,000 and 27,000 lb, and they were applied on top of an 11.9-inch circular plate located at the top of the AC layer. The 3D-Move Analysis software was used to calculate the vertical stresses at the pipe elevation (i.e., 6 inches below the top of the SG) using representative material properties of the pavement structure.[(26)] However, it should be noted that 3D-Move Analysis software does not account for the presence of the pipe when calculating the stresses at the specified depth.[(26)]

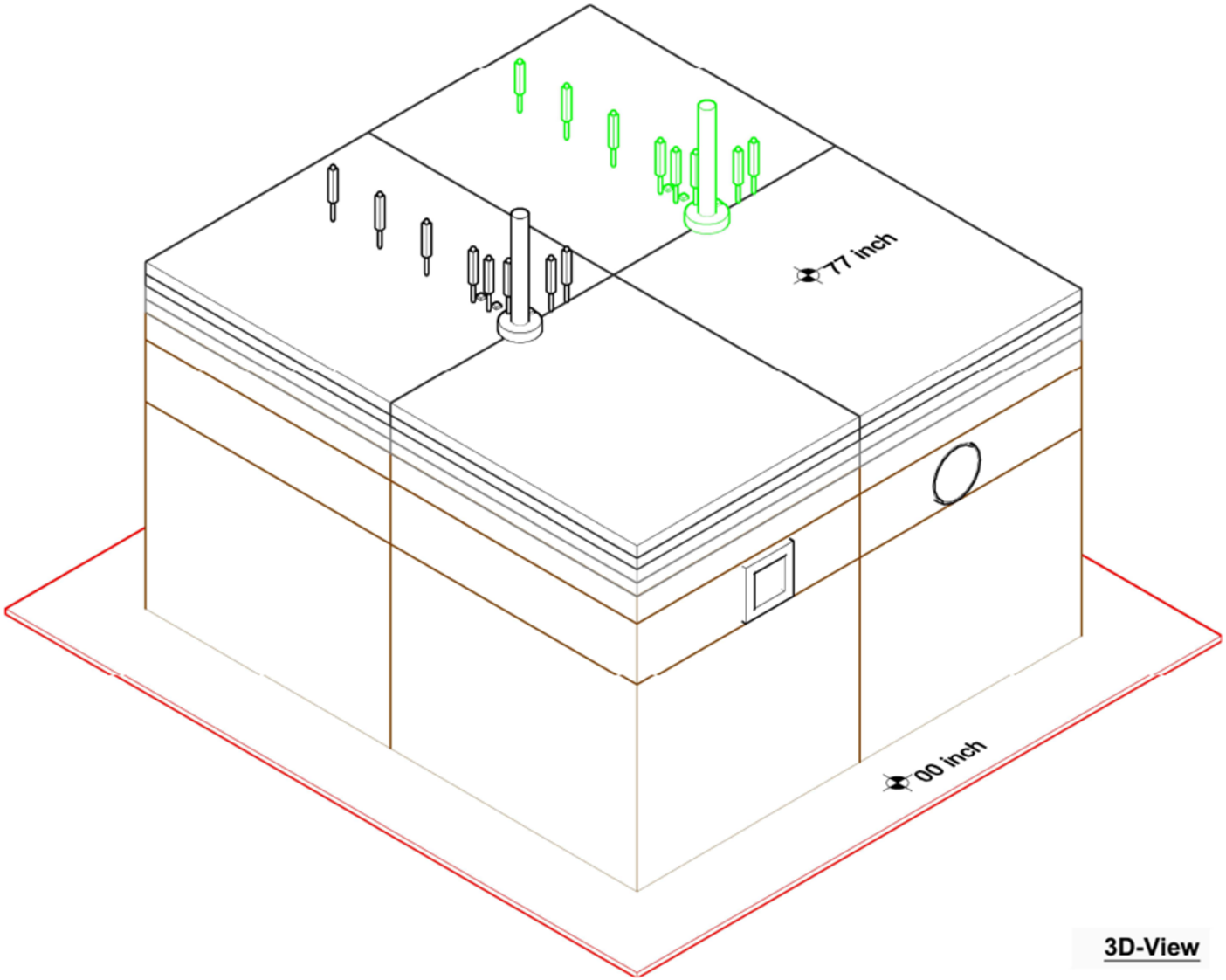

Figure 72. Illustration. Three-dimensional view of large-scale-box instrumentations in experiment No. 5 (elevation of 77 inches).

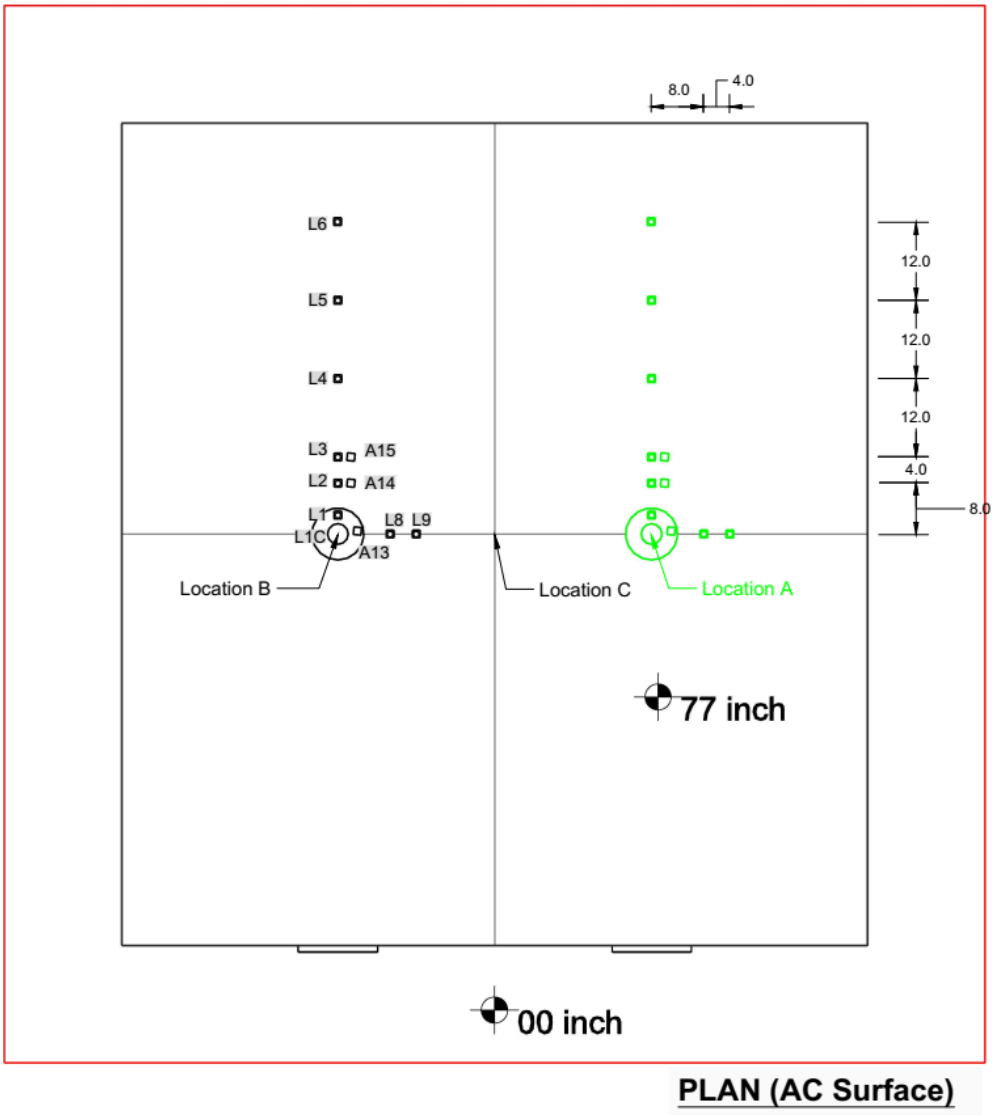

Note: All dimensions are in inches.
L = LVDT; A = ACC.

Figure 73. Illustration. Plan view of large-scale-box instrumentations in experiment No. 5 (elevation of 77 inches).

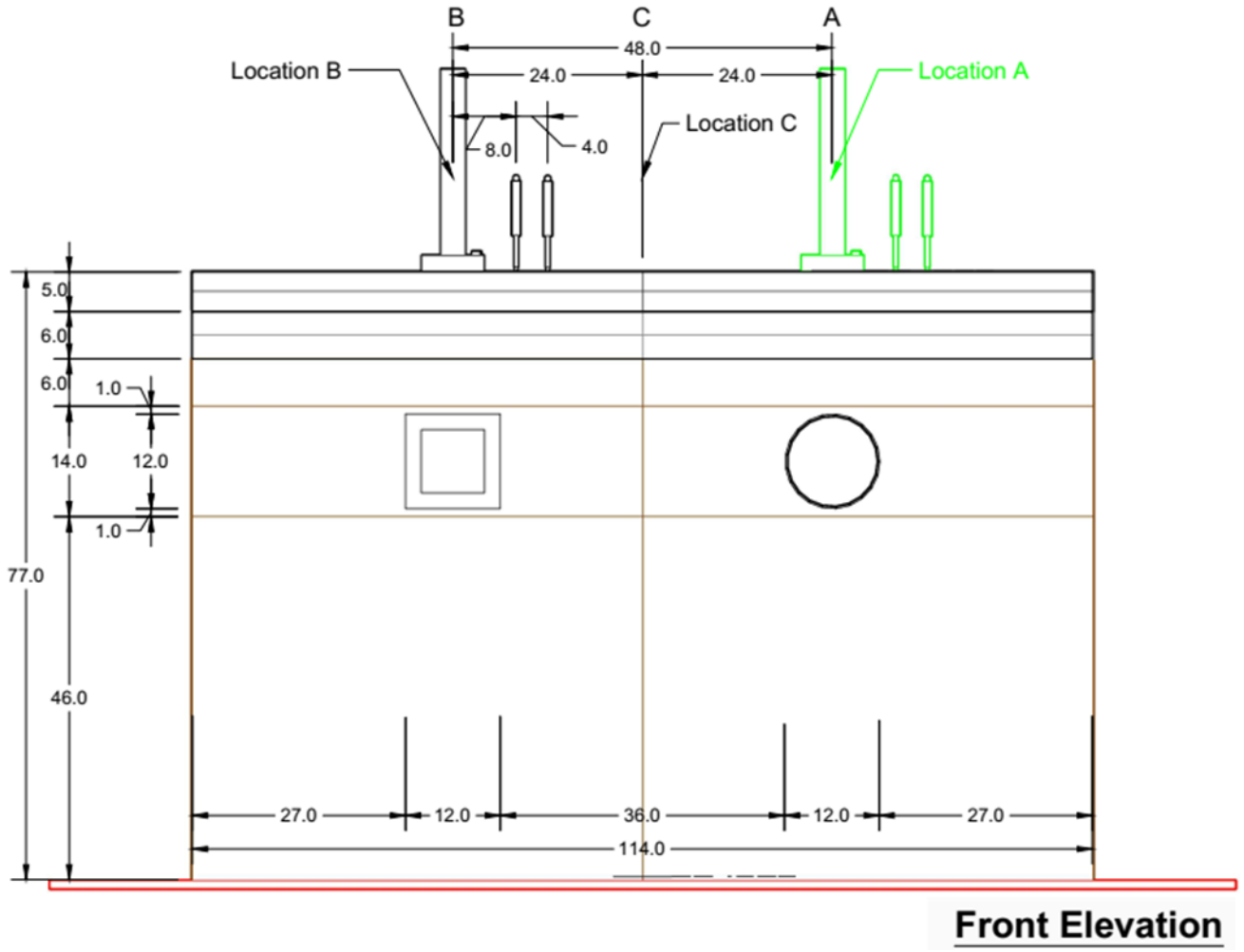

Note: All dimensions are in inches.

Figure 74. Illustration. Elevation of large-scale-box instrumentations in experiment No. 5 (elevation of 77 inches).

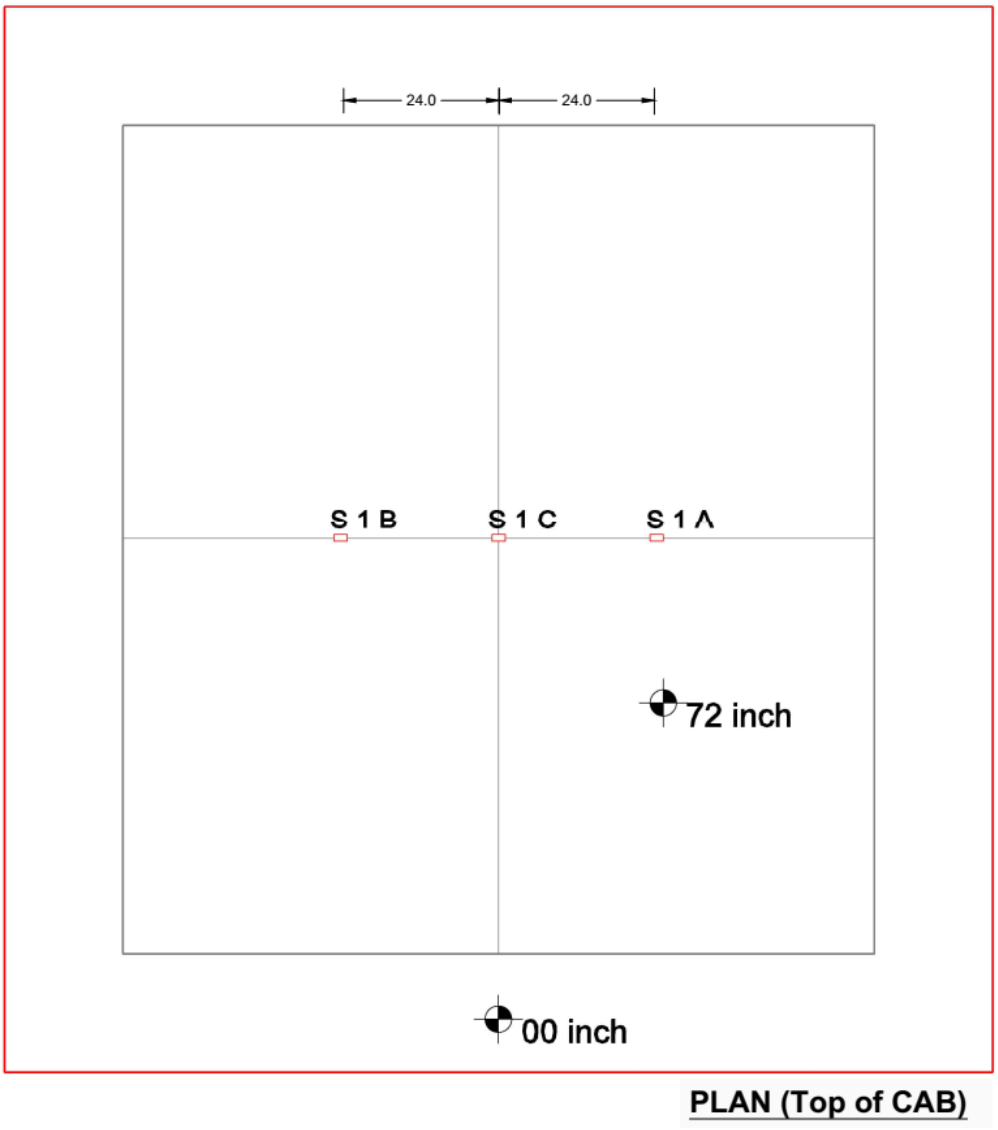

Note: All dimensions are in inches.
S = strain gauge.

Figure 75. Illustration. Plan view of large-scale-box instrumentations in experiment No. 5 (elevation of 72 inches).

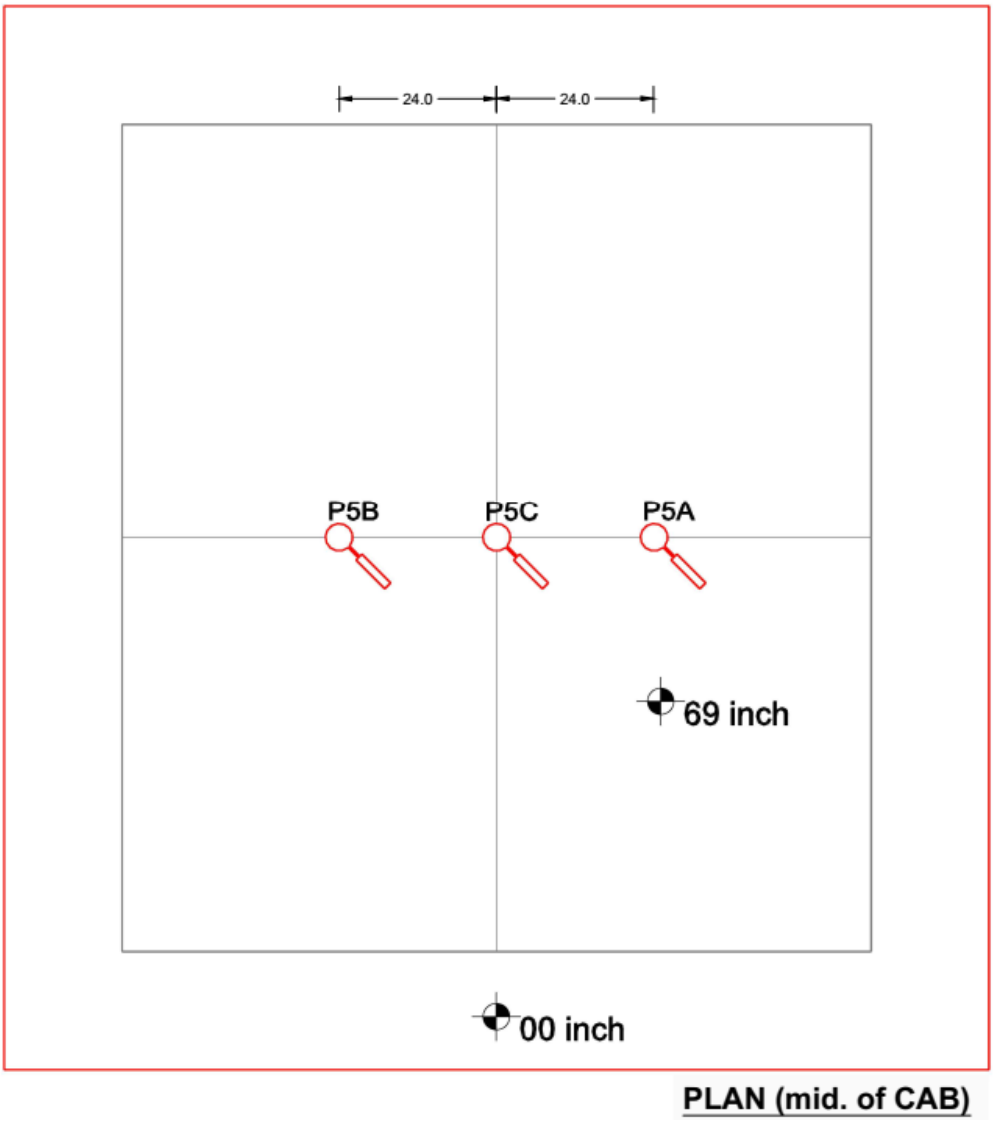

Note: All dimensions are in inches.
P = TEPC.

Figure 76. Illustration. Plan view of large-scale-box instrumentations in experiment No. 5 (elevation of 69 inches).

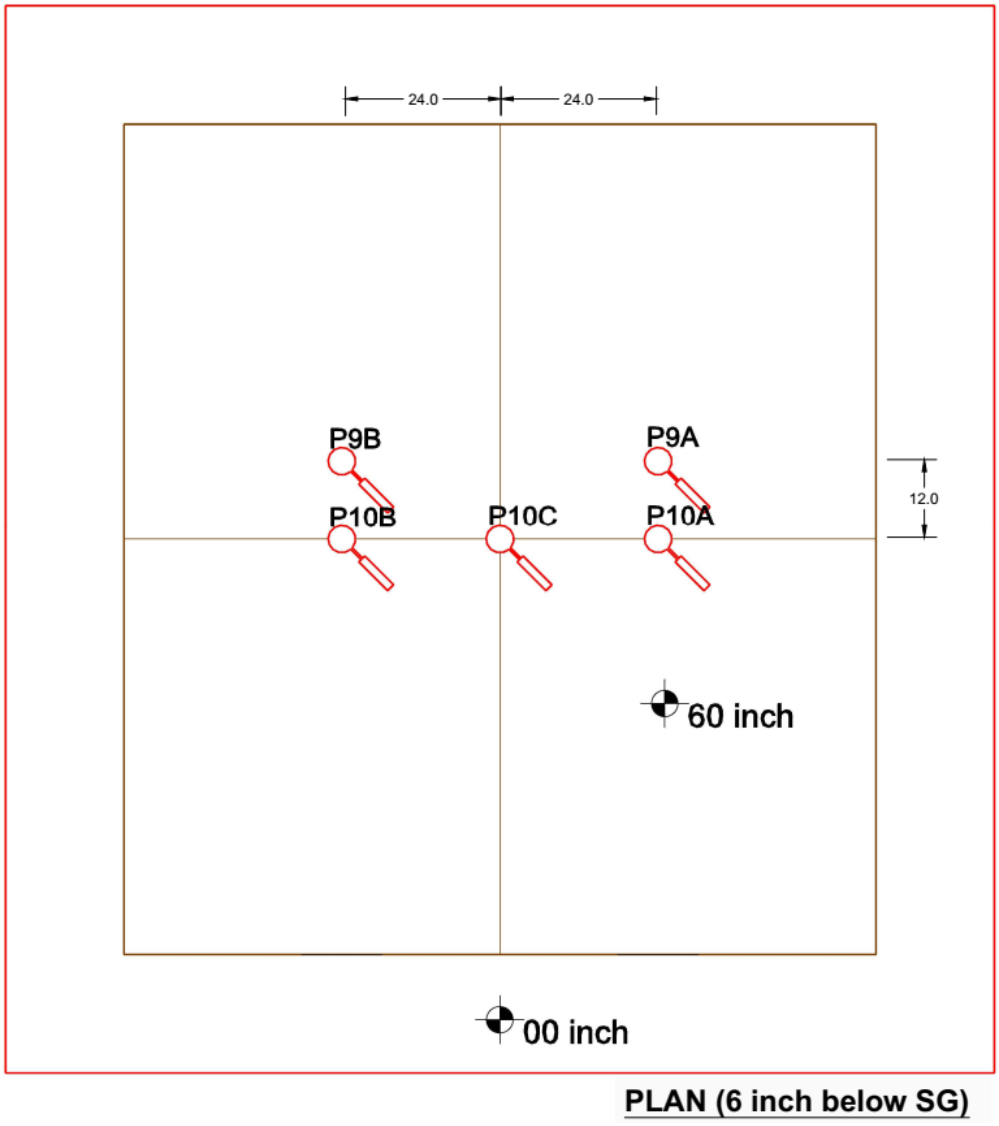

Note: All dimensions are in inches.
P = TEPC.

Figure 77. Illustration. Plan view of large-scale-box instrumentations in experiment No. 5 (elevation of 60 inches).

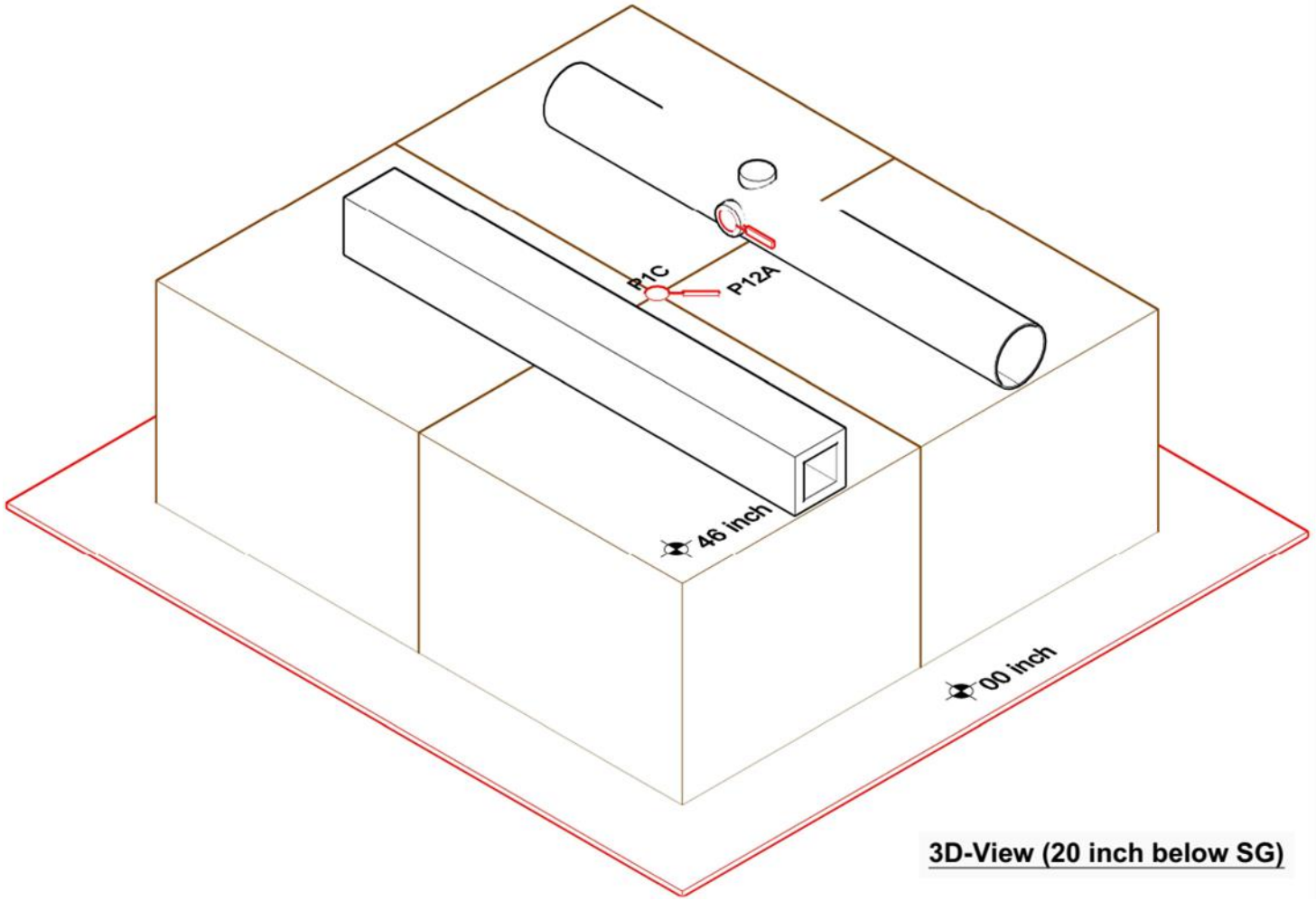

P = TEPC.

Figure 78. Illustration. Three-dimensional view of large-scale-box instrumentations in experiment No. 5 (elevation of 46 inches).

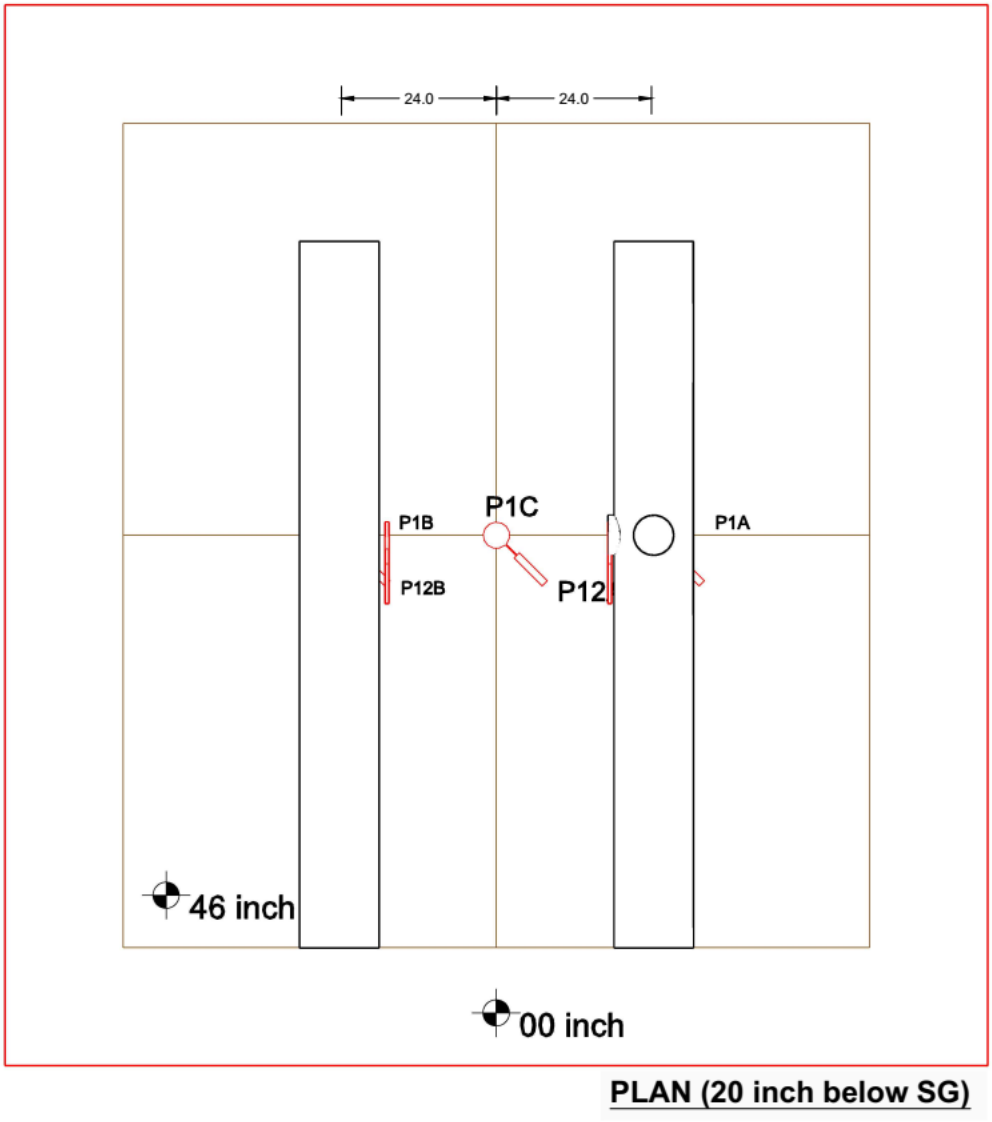

Note: All dimensions are in inches.
P = TEPC.

Figure 79. Illustration. Plan view of large-scale-box instrumentations in experiment No. 5 (elevation of 46 inches).

In order to maximize the benefits and utilization of the research from experiment No. 5, a pipe-selection criterion was adopted. This criterion allowed the pipe to act elastically at lower load levels and yield or indicate failure (or distress) at higher load levels. An iterative process was carried out using different combinations of standard steel-pipe diameters and wall thicknesses. After several trials, a 12-inch-(outer) diameter pipe with 0.125-inch wall thickness was selected. Although only standard steel pipes were used in the analysis, not all of the pipe sizes were readily available from the suppliers, including the one selected for this experiment. Therefore, a special order had to be made to get the desired pipe size. A 9-ft section of the pipe was used in the experiment to reduce the boundary effect and is shown in figure 80.

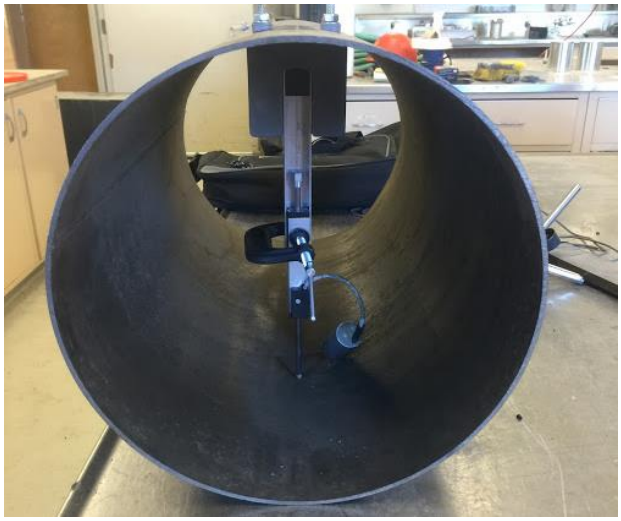

Figure 80. Photo. Short section of the flexible steel pipe with an LVDT attached inside the pipe (LVDT fixture designed and produced in-house using three-dimensional printing).

Selection of Rigid Buried Structure

Rigid buried structures are designed to resist wall stresses resulting from internal and external loads. These structures, commonly referred to as culverts, are typically made of concrete or clay and come in square, rectangular, or circular cross sections. A criterion similar to the one used for selecting the appropriate flexible pipe was adopted for the culvert selection and design. The procedure used the same stresses, assessed from 3D-Move Analysis software, resulting from the five load levels (between 9,000 and 27,000 lb).[(26)] SAP2000®, a finite element program, was then used to assess the stresses induced in the culvert walls.[(27)] Readily available sections were checked first to judge if failure could be reached at the higher load levels. However, it was concluded that these sections were too thick and would not experience any significant failure. Consequently, it was decided to build a section with a wall thickness that could endure failure at higher load levels. A square cross section was selected since it was easier to construct. The selected size was 12 by 12 inches (outer dimensions) to be consistent with the steel pipe size. A SAP2000® analysis yielded an all-around wall thickness of 1 inch.[(27)] This wall thickness was selected so that the box culvert would experience some damage at higher load levels. The analysis assumed a concrete strength of 4,000 psi.

After designing the culvert cross section, a contractor was hired for the construction. The research team faced several challenges. For example, this culvert was not heavily reinforced, so offsite fabrication of a 9-ft-long section posed a risk of damaging it during transportation and installation. Also, since the culvert was monolithic, removing the inside falsework from the culvert posed another risk of damage. After several iterations, the research team decided to construct the culvert on site and inside the large-scale box at its testing location. The research team also decided to use wood for the outside falsework and foam, which can be easily removed without damaging the culvert walls or its top cover, as a support falsework for the inside of the culvert. To ensure a uniform cross section without any voids, it was decided to use SCC. Figure 81 shows a picture of the box culvert after construction.

Figure 81. Photo. Cast-in-place monolithic rigid box culvert in the large-scale box.

Loading Protocol and Instrumentations

Figure 72 shows a schematic of the test setup and points of surface load application. The experiment was divided into two phases. In the first phase, the surface load was applied directly on top of the flexible pipe, while in phase two, the surface load was applied directly on top of the rigid culvert. The responses of both buried structures were monitored during both phases of loading to see the effect of offset loads. The loading protocol was similar to the one used in previous experiments for comparative purposes. The five dynamic load levels (9,000; 12,000; 16,000; 21,000; and 27,000 lb) were applied in each phase. The incremental dynamic load had a pulse duration of 0.1 s followed by a rest period of 0.9 s. Table 15 provides a summary of the loading protocol for experiment No. 5. All loads were applied on the loading plate positioned directly at the top of the AC layer but at the aforementioned locations. Both buried structures were appropriately instrumented for fully capturing their responses.

At the end of the dynamic-load tests for both phases, the pavement structure was allowed to recover for 30 min. An increasing static load was then applied up to failure with a constant loading rate of 0.4 inch/min. The static load was applied on the loading plate positioned directly at the top of the AC layer and at the centerline of each of the buried utilities.

Table 15. Loading protocol for experiment No. 5 (full pavement with buried utilities).

Load Type	Target Load Amplitude (lb)	Loading Cycles or Loading Rate	Load Plate Diameter (Inch)	Rest Period Between Load Levels (min)
Dynamic load (0.1-s loading plus 0.9-s rest period)	9,000	25 cycles	11.9 (FWD loading plate)	2
Dynamic load (0.1-s loading plus 0.9-s rest period)	12,000	25 cycles	11.9 (FWD loading plate)	2
Dynamic load (0.1-s loading plus 0.9-s rest period)	16,000	25 cycles	11.9 (FWD loading plate)	2
Dynamic load (0.1-s loading plus 0.9-s rest period)	21,000	25 cycles	11.9 (FWD loading plate)	2
Dynamic load (0.1-s loading plus 0.9-s rest period)	27,000	25 cycles	11.9 (FWD loading plate)	2
Static load	Up to failure	0.4 inch/min	11.9 (steel plate)	Constant loading rate

The instrumentation for the pavement structure consisted of 13 4-inch TEPCs placed at 4 locations: in the middle of the CAB, 6 and 20 inches below the SG surface to measure vertical pressure, and on the inner sides of the utilities to measure horizontal pressure. The vertical pressure cells were located directly under the center of the loading plate and laterally at each of the depth levels at various locations. At the first level (the middle of the CAB), there were three sensors directly under the center of the loading plate at the three loading locations (A, B, and C) as shown in figure 73 and figure 74. At the second level (6 inches below the SG surface), there were five sensors. At the bottom level (20 inches below the SG surface), there were three sensors directly under the center of the three loading locations. More details on the TEPCs can be inferred from figure 76 through figure 79 and table 16. As noted, the sensors were installed after compacting the SG and CAB to the level of the instruments, the pressure cells were then placed carefully on a leveled surface created by a thin layer of compacted, fine material, to ensure full contact with the cell and to facilitate a better bearing surface. After placement of the sensor, additional material was placed carefully on top of the cell and compacted by hand using a steel tamper plate.

LVDT sensors were installed inside the buried utilities to monitor the internal deflections. Four sensors were installed inside the steel pipe at two locations using a three-dimensional-printed special mounting piece. Two LVDTs were placed along the centerline of the pipe perpendicular to each other to measure the vertical and horizontal deflections, and two LVDTs were installed 12 inches off the centerline as shown in figure 82. Similarly, another four LVDTs were installed inside the concrete box culvert at two locations: along the centerline of the culvert and 12 inches off the centerline as shown in figure 83. In addition, a high-resolution digital camera was installed inside the steel pipe to get video feed of the deflections inside the pipe during the tests.

Table 16. Details of the instrumentation plan for experiment No. 5 (full pavement with buried utilities).

No.	Tag	Sensor Name	Capacity	Specification	Radius (Inch)	Angle (°)	Depth (Inch)	X (Inch)	Y (Inch)	Z (Inch)	ID/SN	No. of Channels	Notes
1	L1C	LVDT1C	1 inch	TR-0025	0	0	0	0	0	77	—	1	Center LVDT
2	L1	LVDT01	4 inch	TR-0100	0	0	0	0	0	77	—	1	LVDT
3	L2	LVDT02	4 inch	TR-0100	8	90	0	0	−8.0	77	—	1	LVDT
4	L3	LVDT03	4 inch	TR-0100	12	90	0	0	−12.0	77	—	1	LVDT
5	L4	LVDT04	4 inch	TR-0100	24	90	0	0	−24.0	77	—	1	LVDT
6	L5	LVDT05	4 inch	TR-0100	36	90	0	0	−36.0	77	—	1	LVDT
7	L6	LVDT06	4 inch	TR-0100	48	90	0	0	−48.0	77	—	1	LVDT
8	L8	LVDT08	4 inch	TR-0100	8	0	0	−8.0	0	77	—	1	LVDT
9	L9	LVDT09	4 inch	TR-0100	12	0	0	−12.0	0	77	—	1	LVDT
10	P1A	P01A	36 psi	4-inch cell	24	0	31	−24.0	0	46	1330827	1	Pressure cell (vertical)
11	P1B	P01B	36 psi	4-inch cell	24	180	31	24.0	0	46	1330825	1	Pressure cell (vertical)
12	P1C	P01C	87 psi	4-inch cell	0	0	31	0	0	46	1404682	1	Pressure cell (vertical)
13	P5A	P05A	36 psi	4-inch cell	24	0	8	−24.0	0	69	1533652	1	Pressure cell (vertical)
14	P5B	P05B	362 psi	4-inch cell	24	180	8	24.0	0	69	1533653	1	Pressure cell (vertical)
15	P5C	P05C	362 psi	4-inch cell	0	0	8	0	0	69	1330822	1	Pressure cell (vertical)
16	P9A	P09A	87 psi	4-inch cell	26.8	26.6	17	−24.0	−12.0	60	1404681	1	Pressure cell (vertical)
17	P9B	P09B	145 psi	4-inch cell	26.8	153.4	17	24.0	−12.0	60	1427205	1	Pressure cell (vertical)
18	P10A	P10A	87 psi	4-inch cell	24	0	17	−24.0	0	60	1427206	1	Pressure cell (vertical)
19	P10B	P10B	145 psi	4-inch cell	24	180	17	24.0	0	60	1533651	1	Pressure cell (vertical)
20	P10C	P10C	87 psi	4-inch cell	0	0	17	0	0	60	1427204	1	Pressure cell (vertical)
21	P12A	P12A	36 psi	4-inch cell	18	0	24	−18.0	0	53	1330824	1	Pressure cell (horizontal)
22	P12B	P12B	36 psi	4-inch cell	18	180	24	18.0	0	53	1330826	1	Pressure cell (horizontal)
23	A13	ACC13	±5 g	3-axis	0	0	0	0	0	77	—	1	ACC
24	A14	ACC14	±5 g	3-axis	12	90	0	0	−12.0	77	—	1	ACC
25	A15	ACC15	±5 g	3-axis	24	90	0	0	−24.0	77	—	1	ACC
26	A16	ACC16	±5 g	3-axis	—	—	—	—	—	—	—	1	Frame ACC
27	—	LCST01	—	—	—	—	—	—	—	—	—	1	Applied load-string pod
28	—	LC01	—	—	—	—	—	—	—	—	—	1	Applied load-load cell
29	S1A	S1A	—	—	24	0	5	−24.0	0	72	—	1	AC strain gauge
30	S1B	S1B	—	—	24	180	5	24.0	0	72	—	1	AC strain gauge
31	S1C	S1C	—	—	0	0	5	0	0	72	—	1	AC strain gauge

—Not applicable.

Figure 82. Photo. Four LVDTs installed inside the buried steel pipe at the centerline of the pipe and 12 inches off the center of the pipe.

Figure 83. Photo. Four LVDTs installed inside the buried concrete box culvert at the centerline of the pipe and 12 inches off the center of the box culvert.

Surface LVDTs were also installed to measure surface deflections at various radial distances (0, 8, 12, 24, 36, and 48 inches). The moving tip of the surface LVDT rested on top of the AC layer. In addition to the LVDT(s), rosette strain gauges were bonded to the outer surface of the buried steel pipe, underneath the pressure cells, to measure the strains induced in the buried steel pipe from surface loading. The installation was done after the steel pipe was in place to ensure accurate placement. The rosette strain gauges were located along the centerline, on the top, and on the side of the steel pipe. All gauges were installed according to specifications. Once the locations were selected, the pipe was smoothed out using an ultrafine sandpaper then cleaned with fast evaporating acetone. Using a cyanoacrylate adhesive, the three-element rosette strain gauges were attached and allowed to dry.

AC strain gauges were also placed at the bottom of the AC layer to capture the strains of the pavement under the dynamic and static loading. The strain gauge installation process was similar

to the procedure described in section 2.8.3. Figure 84 and figure 85 show pictures of the final product of experiment No. 5 after placement of the all pavement layers and instruments at loading locations A (top of steel pipe) and C (top of box culvert).

Figure 84. Photo. Completed large-scale-box test setup for experiment No. 5—loading location A (top of steel pipe).

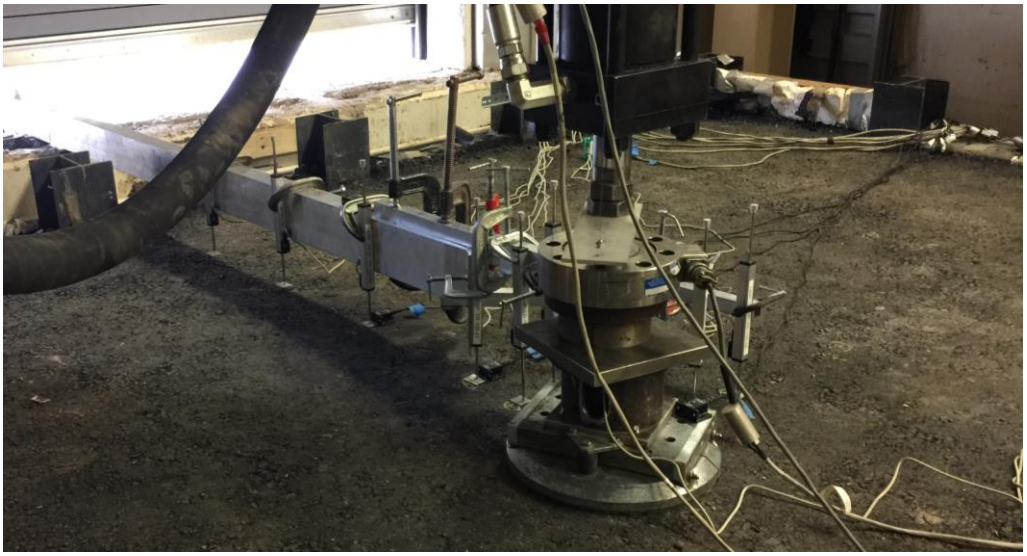

Figure 85. Photo. Completed large-scale-box test setup for experiment No. 5—loading location C (top of box culvert).

CHAPTER 3. PRESENTATION OF EXPERIMENTAL DATA

In this chapter, the results of preprocessed recordings measured by the load cell, LVDTs, and TEPCs during experiments No. 1, No. 2, and No. 3 are presented. The synthesis and discussion of the measurements for experiment No. 4 (i.e., sloping edge experiment) and experiment No. 5 (i.e., buried utilities experiment) are presented in detail in Volume VII: Appendix F and Volume VIII: Appendix G, respectively.[6,7]

3.1. PREPROCESSING OF INSTRUMENTS' MEASUREMENTS

As mentioned earlier, the laboratory-testing program for the experiments included a series of instruments. LVDTs, TEPCs, and ACCs that measure vertical surface displacements, vertical stresses, and accelerations (often multicomponent) at the installed locations were employed. Acceleration measurements were not used in the current study so that the analyses of ACCs are not presented.

The following preprocessing steps were undertaken for all recordings to identify and separate the appropriate load-induced response signals from the recorded data:

1. Selection of the five representative consecutive cycles of loading. These cycles are selected after the application of the pulse load has been repeated many times (up to about 25) thus allowing for the steady-state condition to develop.

2. Removal of the noise (subtracting the average of the recorded measurements prior to the application of impulse load from the all measurements).

3. Removal of the initial offset (zero offset).

Typical measured recordings by load call, LVDTs, and TEPCs along with the preprocessed recordings are illustrated in figure 86 through figure 88.

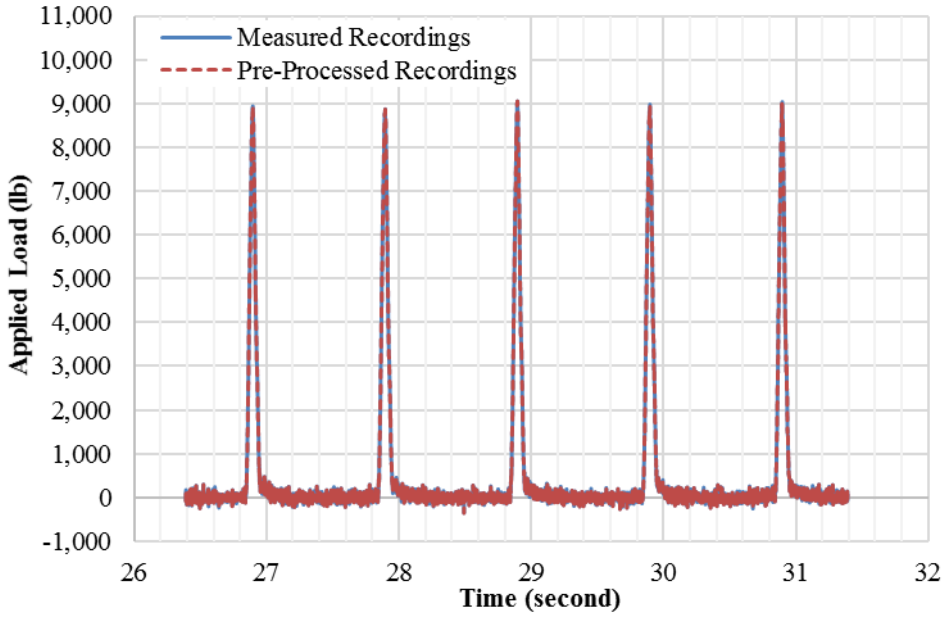

Figure 86. Graph. Measured and preprocessed recordings by load cell in experiment No. 3 at target load level of 9,000 lb.

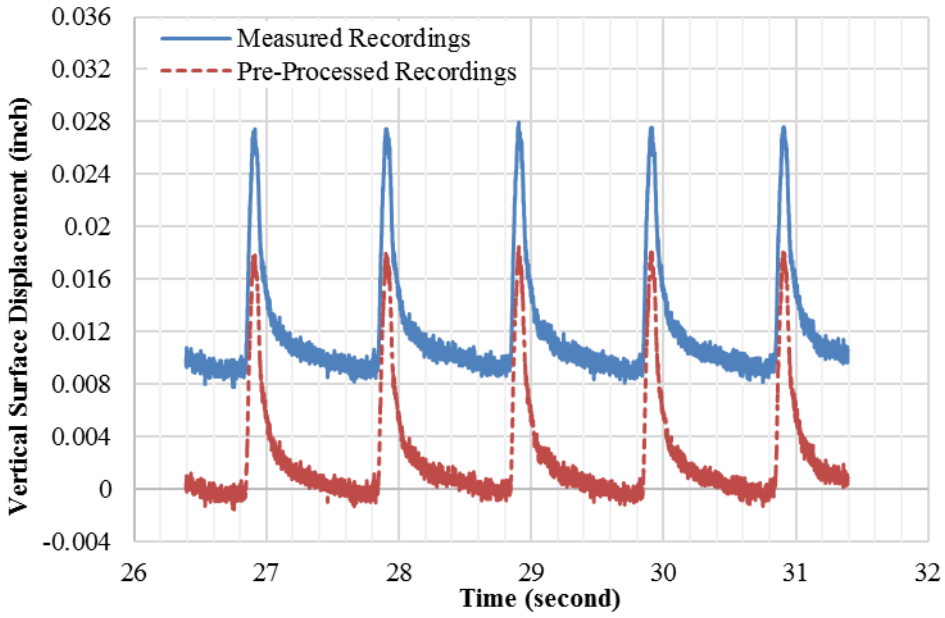

Figure 87. Graph. Measured and preprocessed recordings by LVDT1 in experiment No. 3 at target load level of 9,000 lb.

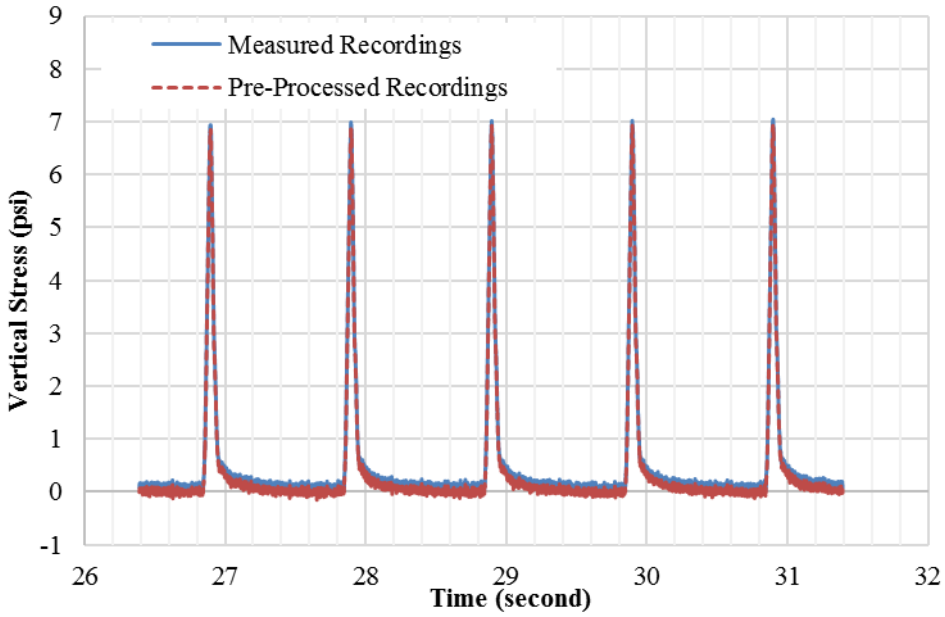

Figure 88. Graph. Measured and preprocessed recordings by TEPC10 in experiment No. 3 at target load level of 9,000 lb.

3.2. PRESENTATION OF PREPROCESSED DATA

In this section, the results of preprocessed recordings measured by the load cell, LVDTs, and TEPCs for experiments No. 1, No. 2, and No. 3 are presented.

3.2.1. Experiment No. 1 (SG Layer Only)

Figure 89 and figure 90 as well as table 17 show the maximum vertical surface displacements from LVDT measurements averaged from five cycles at different load levels. It should be noted that LVDT measurements at the center of the FWD plate (LVDT1) and 8 inches away from the center (LVDT2) are only presented since a high noise to signal ratio at the locations of other LVDTs (i.e., LVDT3, LVDT4, LVDT5, LVDT6, and LVDT7) was observed in this experiment. The vertical stress measurements by TEPC1 and TEPC5 are also summarized in figure 91 and figure 92 and table 17. No clear signals of load-induced vertical stresses were captured by the other TEPCs.

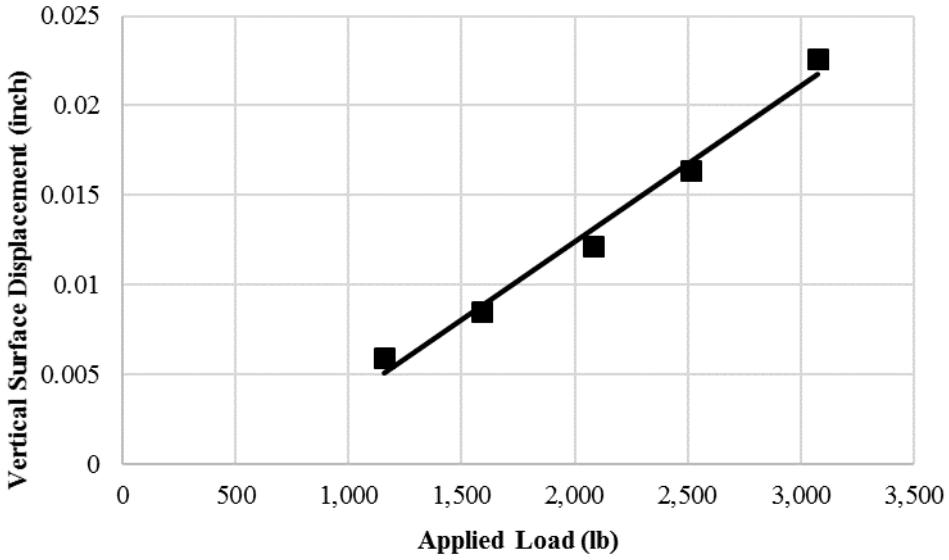

Figure 89. Graph. Vertical surface displacements measured by LVDT1 in experiment No. 1 at different load levels.

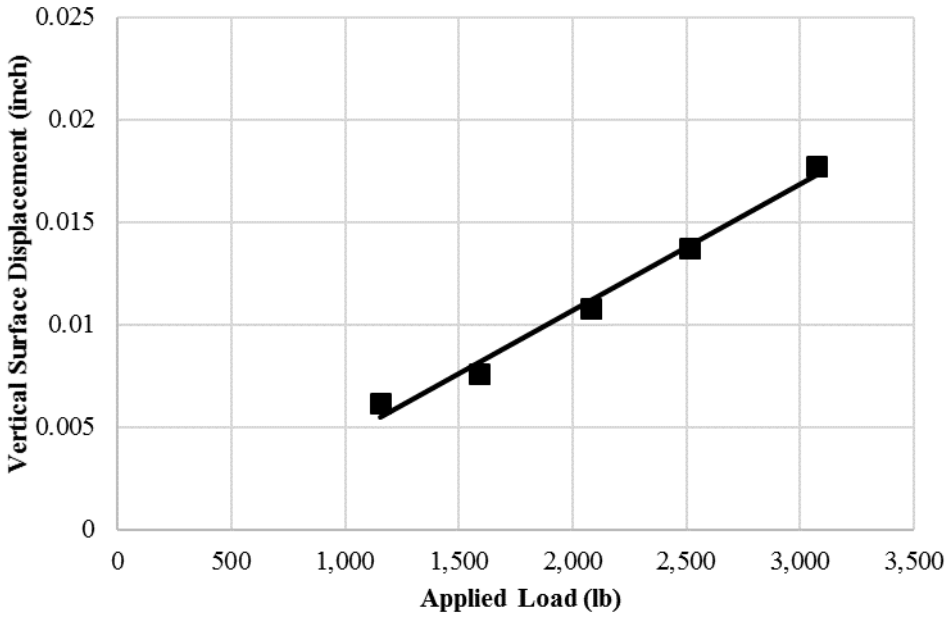

Figure 90. Graph. Vertical surface displacements measured by LVDT2 in experiment No. 1 at different load levels.

Table 17. Vertical surface displacement and vertical stress measurements in experiment No. 1 at different load levels.

Target Load Level (lb)	Average Applied Load (lb)	LVDT1 Vertical Surface Displacements (Inch)	LVDT2 Vertical Surface Displacements (Inch)	TEPC1 Vertical Stress (psi)	TEPC5 Vertical Stress (psi)
1,000	1,154	0.00592	0.00510	1.1	7.1
1,500	1,589	0.00850	0.00759	1.6	9.4
2,000	2,079	0.01218	0.01076	2.0	11.9
2,500	2,514	0.01639	0.01371	2.5	14.6
3,000	3,072	0.02262	0.01771	3.2	18.6

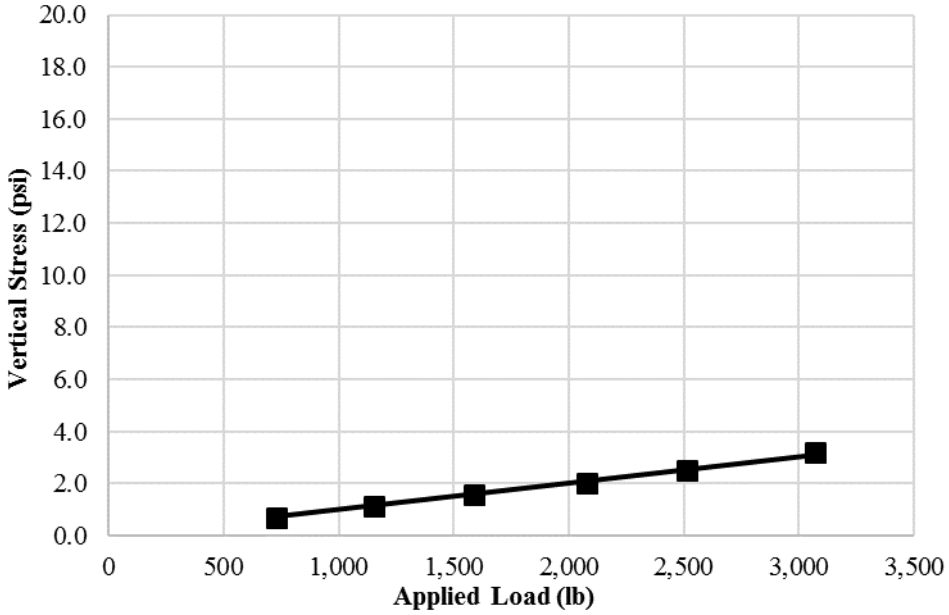

Figure 91. Graph. Vertical stress measured by TEPC1 in experiment No. 1 at different load levels.

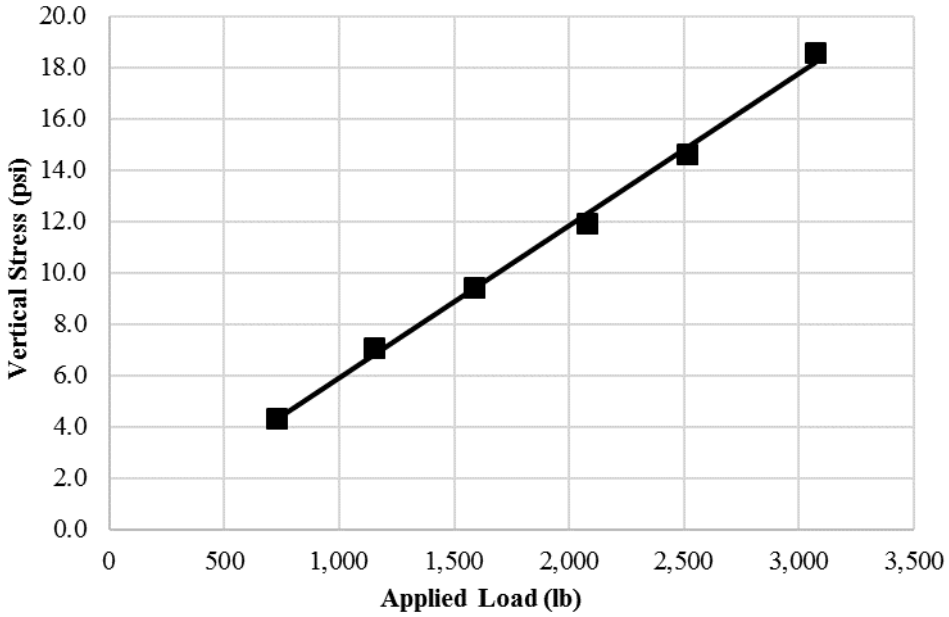

Figure 92. Graph. Vertical stress measured by TEPC5 in experiment No. 1 at different load levels.

3.2.2. Experiment No. 2 (SG and CAB Layers)

In experiment No. 2, vertical surface displacements at the location of LVDT1 (center of FWD plate), LVDT2 (8 inches away from the center), and LVDT3 (12 inches away from the center) were measurable by the LVDTs, while high noise-to-signal ratio at the location of other LVDTs (LVDT4, LVDT5, LVDT6, and LVDT7) was recorded. The results of LVDT measurements in experiment No. 2 are presented in figure 93 through figure 95 and table 18. The results of preprocessed measured stresses by TEPC1, TEPC6, TEPC9, and TEPC10 that are possibly within the zone of influence are also shown in figure 96 through figure 99 and table 18.

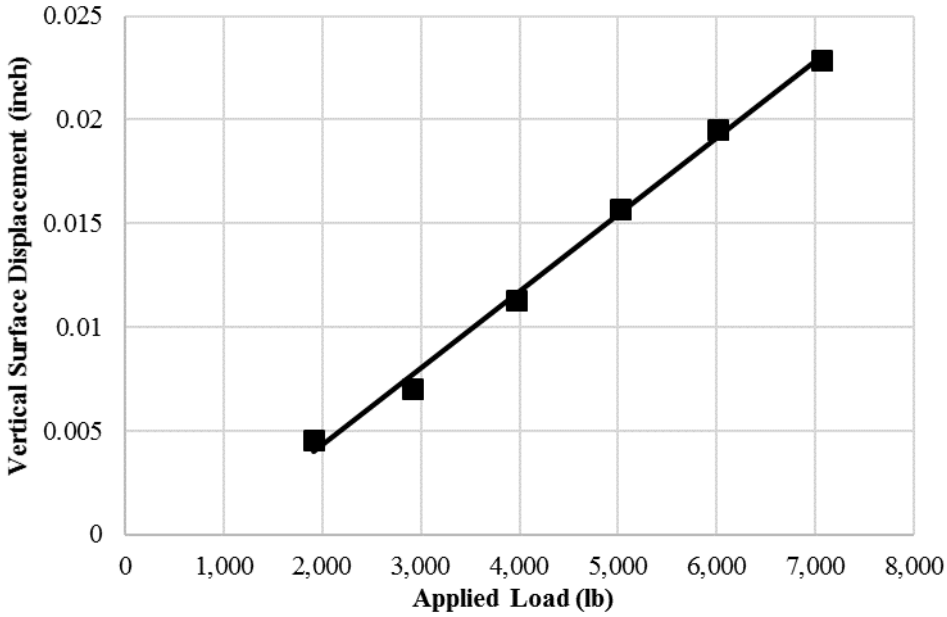

Figure 93. Graph. Vertical surface displacements measured by LVDT1 in experiment No. 2 at different load levels.

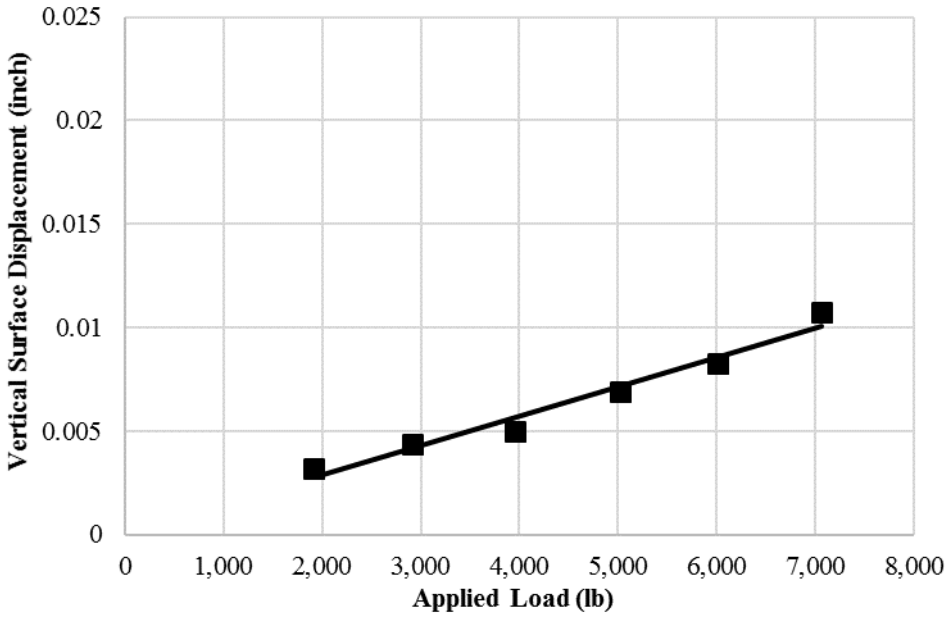

Figure 94. Graph. Vertical surface displacements measured by LVDT2 in experiment No. 2 at different load levels.

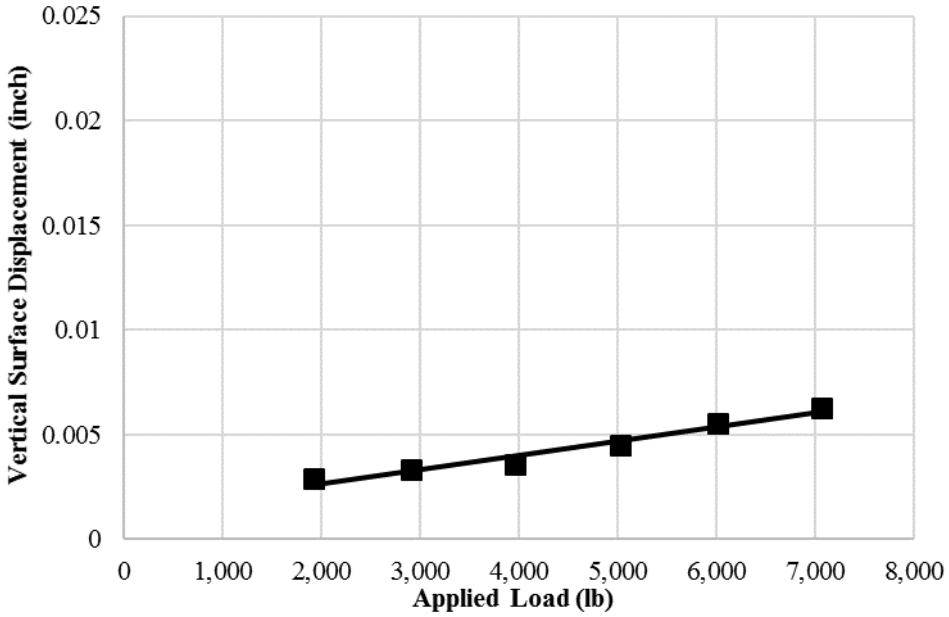

Figure 95. Graph. Vertical surface displacements measured by LVDT3 in experiment No. 2 at different load levels.

Table 18. Vertical surface displacement and vertical stress measurements in experiment No. 2 at different load levels.

Target Load Level (lb)	Average Applied Load (lb)	LVDT1 Vertical Surface Displace-ments (Inch)	LVDT2 Vertical Surface Displace-ments (Inch)	LVDT3 Vertical Surface Displace-ments (Inch)	TEPC1 Vertical Stress (psi)	TEPC6 Vertical Stress (psi)	TEPC9 Vertical Stress (psi)	TEPC10 Vertical Stress (psi)
2,000	1,916	0.00454	0.00319	0.00292	1.2	0.25	1.5	4.1
3,000	2,908	0.00700	0.00435	0.00330	1.9	0.36	2.4	6.6
4,000	3,960	0.01128	0.00497	0.00357	2.7	0.46	3.2	8.9
5,000	5,018	0.01572	0.00688	0.00449	3.6	0.57	4.0	11.1
6,000	6,014	0.01956	0.00824	0.00555	4.4	0.65	4.7	13.2
7,000	7,061	0.02287	0.01075	0.00624	5.3	0.75	5.5	15.0

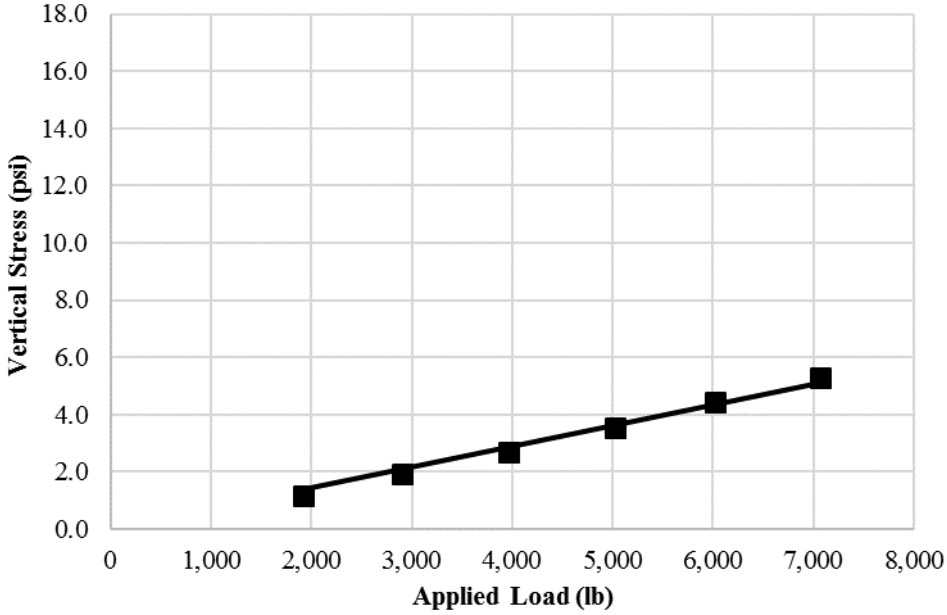

Figure 96. Graph. Vertical stress measured by TEPC1 in experiment No. 2 at different load levels.

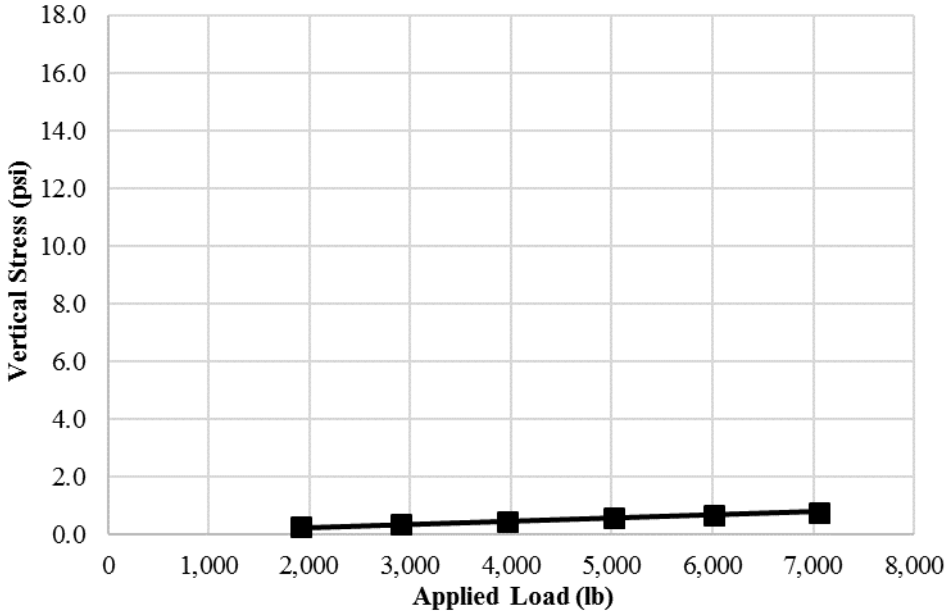

Figure 97. Graph. Vertical stress measured by TEPC2 in experiment No. 2 at different load levels.

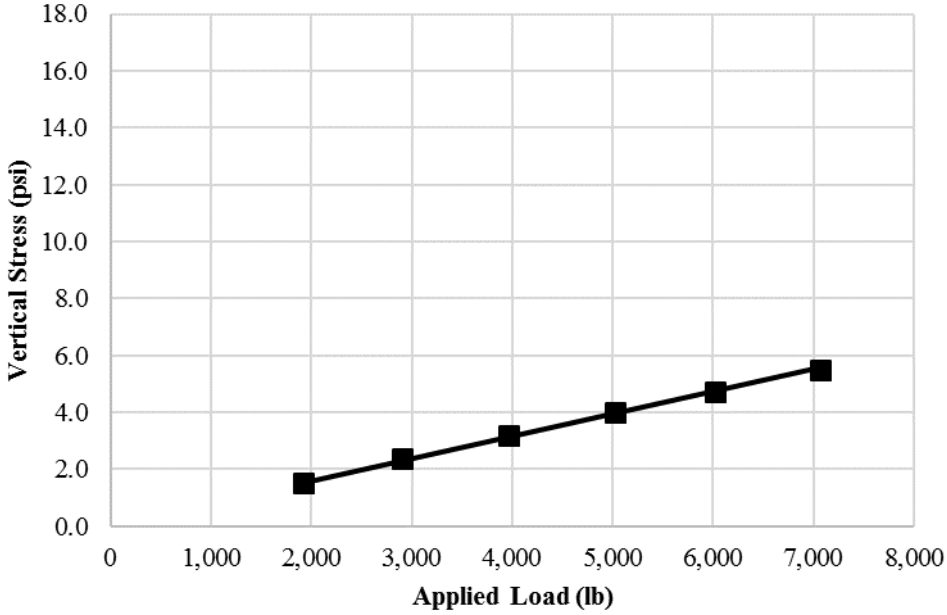

Figure 98. Graph. Vertical stress measured by TEPC9 in experiment No. 2 at different load levels.

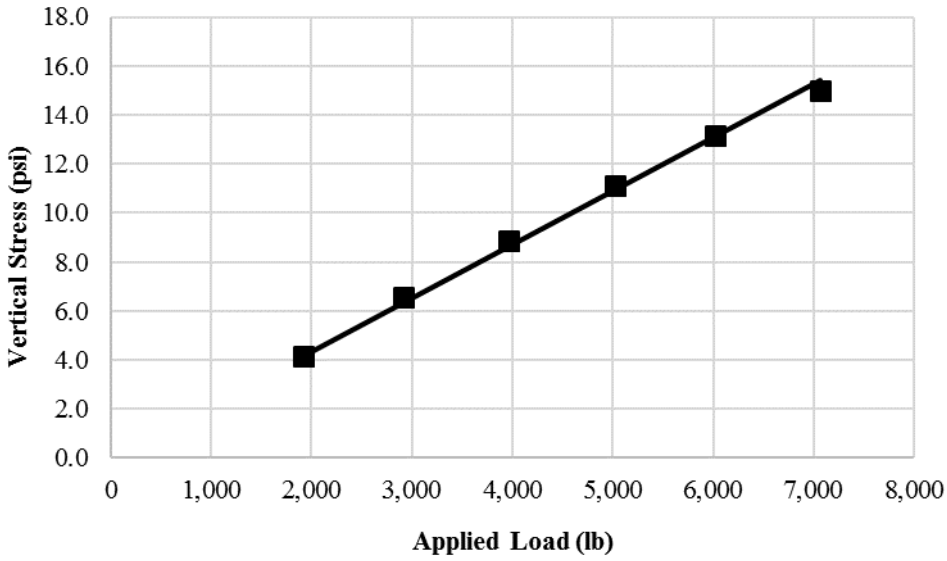

Figure 99. Graph. Vertical stress measured by TEPC10 in experiment No. 2 at different load levels.

3.2.3. Experiment No. 3 (Full Pavement)

The vertical surface displacements measured by the surface LVDTs are presented in figure 100 through figure 106 and table 19. In addition, the results of measured stresses by different TEPCs are shown in figure 107 through figure 112 and table 20.

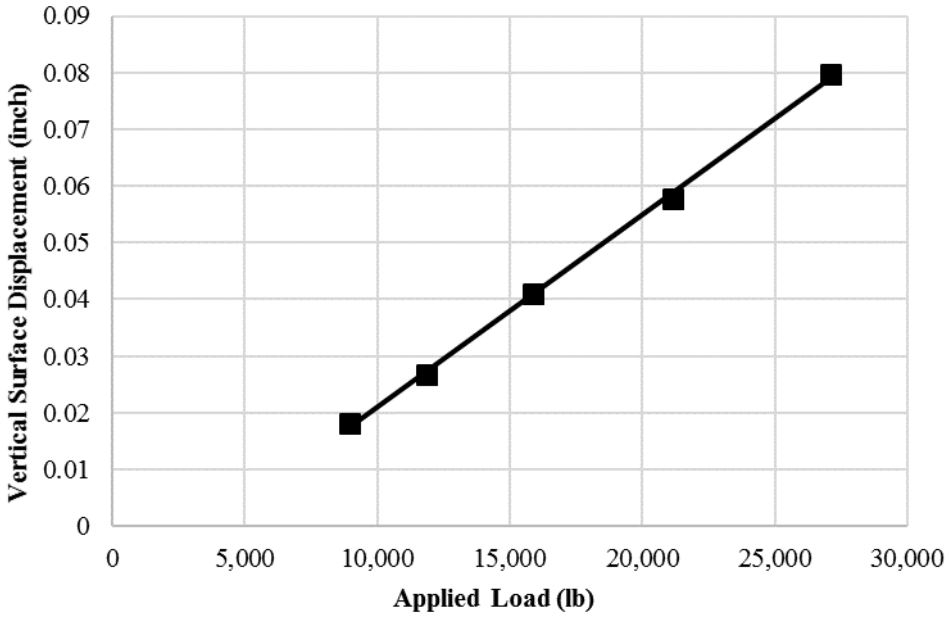

Figure 100. Graph. Vertical surface displacements measured by LVDT1 in experiment No. 3 at different load levels.

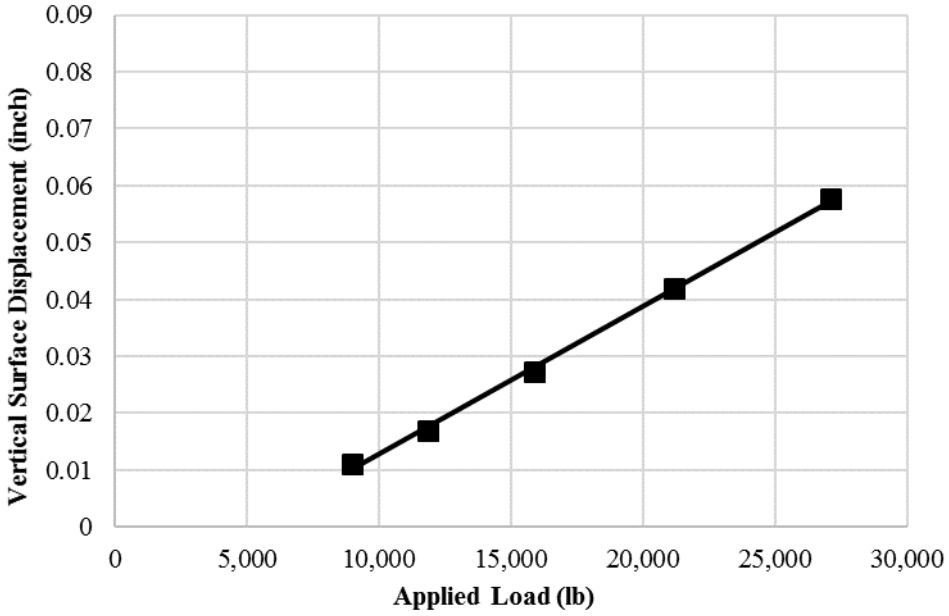

Figure 101. Graph. Vertical surface displacements measured by LVDT2 in experiment No. 3 at different load levels.

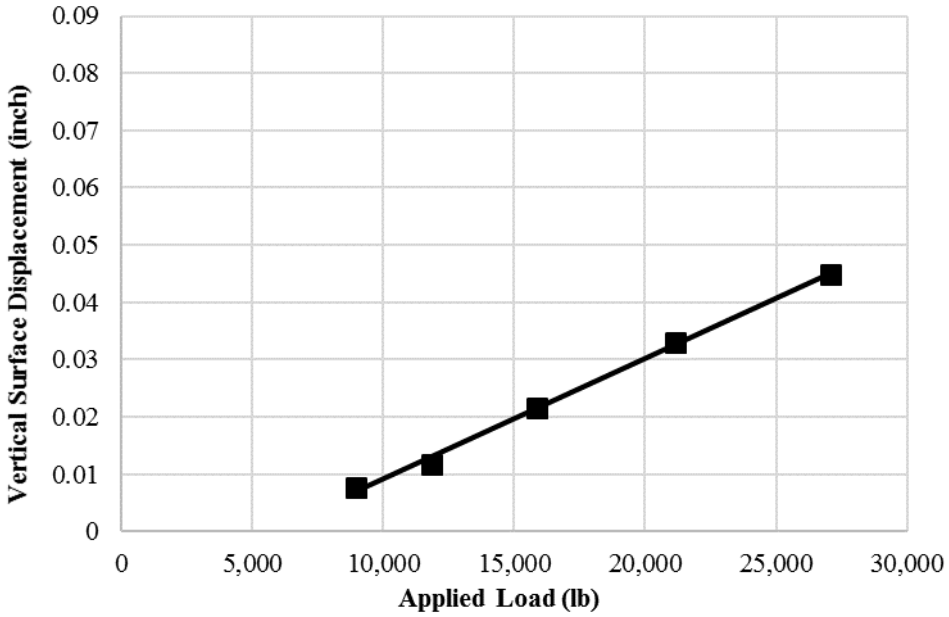

Figure 102. Graph. Vertical surface displacements measured by LVDT3 in experiment No. 3 at different load levels.

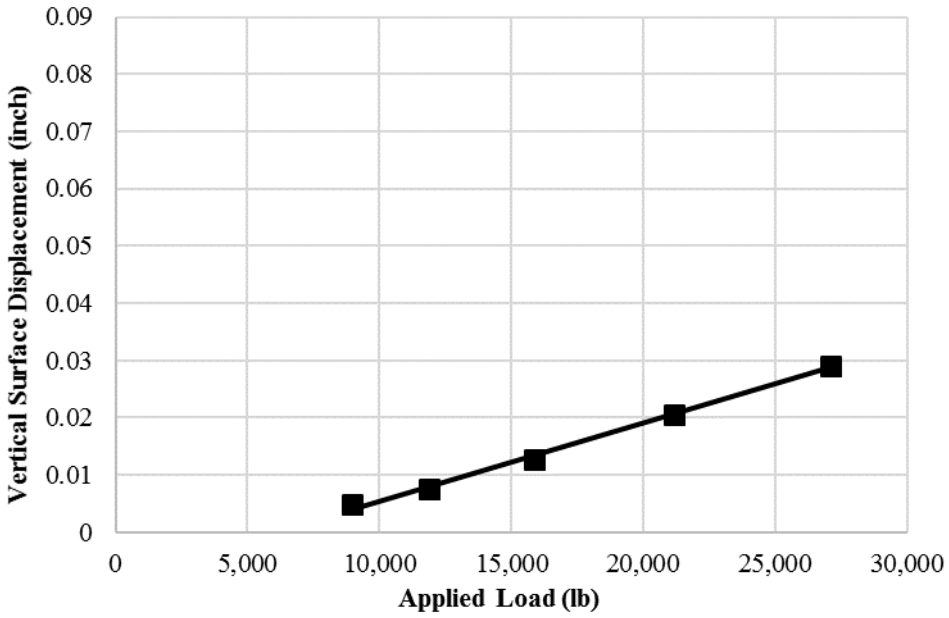

Figure 103. Graph. Vertical surface displacements measured by LVDT4 in experiment No. 3 at different load levels.

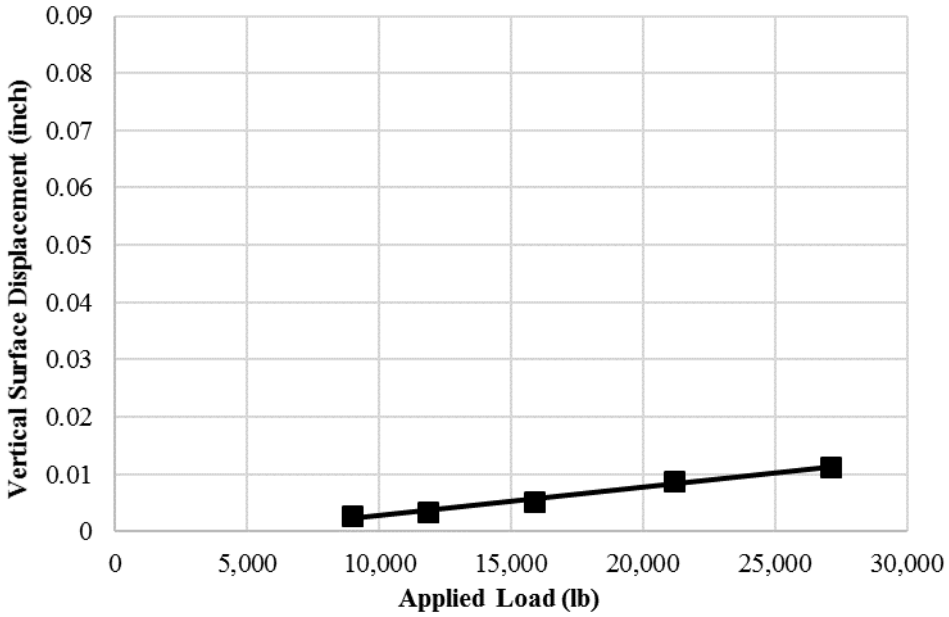

Figure 104. Graph. Vertical surface displacements measured by LVDT5 in experiment No. 3 at different load levels.

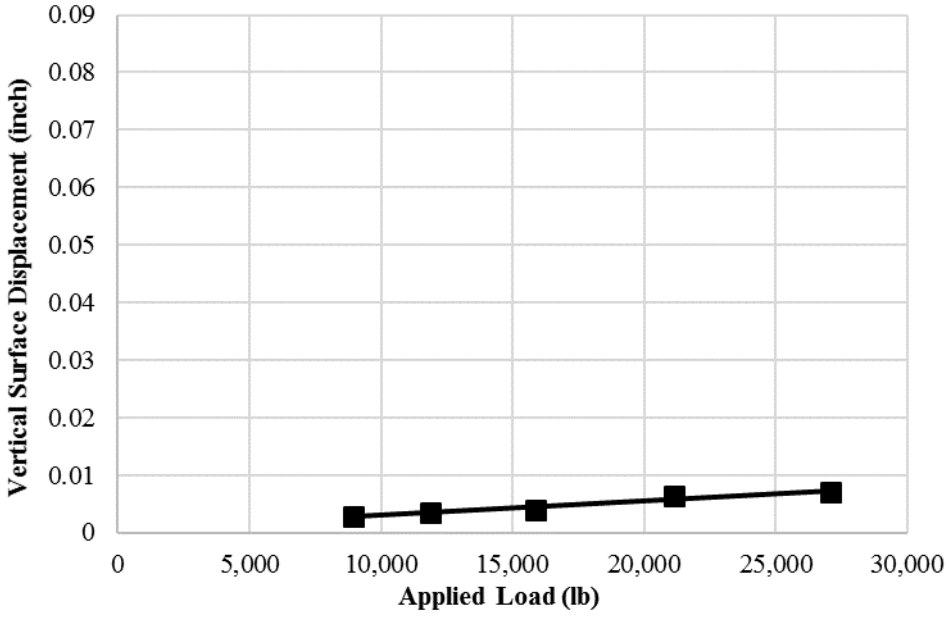

Figure 105. Graph. Vertical surface displacements measured by LVDT6 in experiment No. 3 at different load levels.

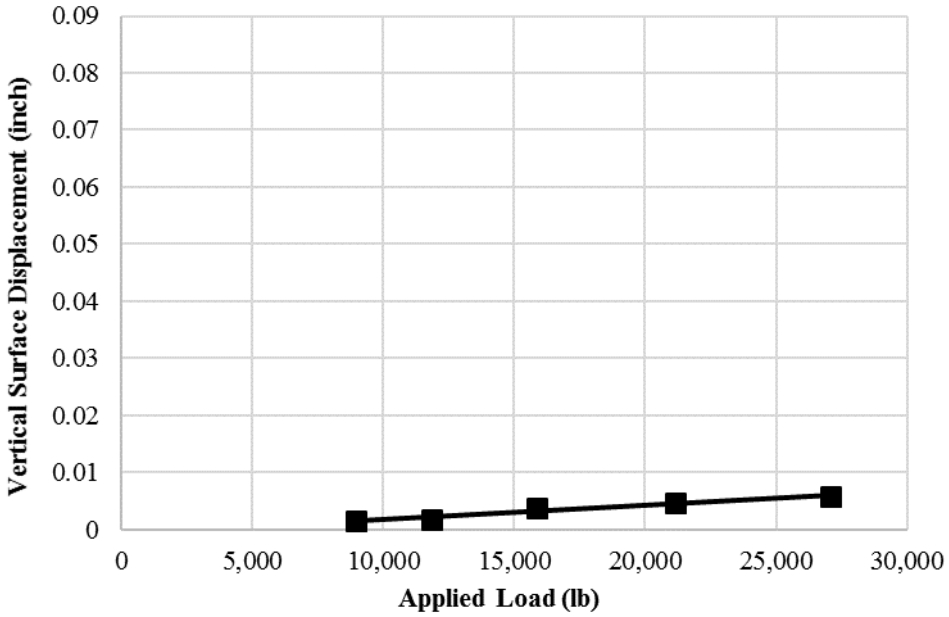

Figure 106. Graph. Vertical surface displacements measured by LVDT7 in experiment No. 3 at different load levels.

Table 19. Vertical surface displacement measurements in experiment No. 3 at different load levels.

Target Load Level (lb)	Aver-age Applied Load (lb)	LVDT1 Vertical Surface Displace-ments (Inch)	LVDT2 Vertical Surface Displace-ments (Inch)	LVDT3 Vertical Surface Displace-ments (Inch)	LVDT4 Vertical Surface Displace-ments (Inch)	LVDT5 Vertical Surface Displace-ments (Inch)	LVDT6 Vertical Surface Displace-ments (Inch)	LVDT7 Vertical Surface Displace-ments (Inch)
9,000	8,971	0.01811	0.01117	0.00773	0.00475	0.00280	0.00281	0.00140
12,000	11,857	0.02683	0.01687	0.01179	0.00755	0.00342	0.00349	0.00171
16,000	15,860	0.04099	0.02729	0.02162	0.01274	0.00536	0.00392	0.00382
21,000	21,146	0.05772	0.04192	0.03305	0.02048	0.00880	0.00628	0.00458
27,000	27,087	0.07976	0.05763	0.04482	0.02908	0.01124	0.00697	0.00577

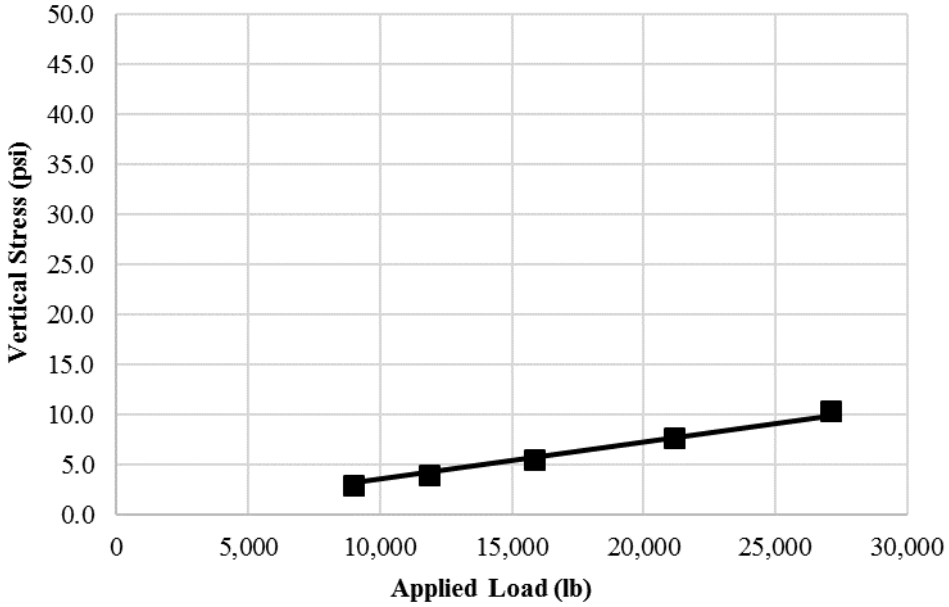

Figure 107. Graph. Vertical stress measured by TEPC1 in experiment No. 3 at different load levels.

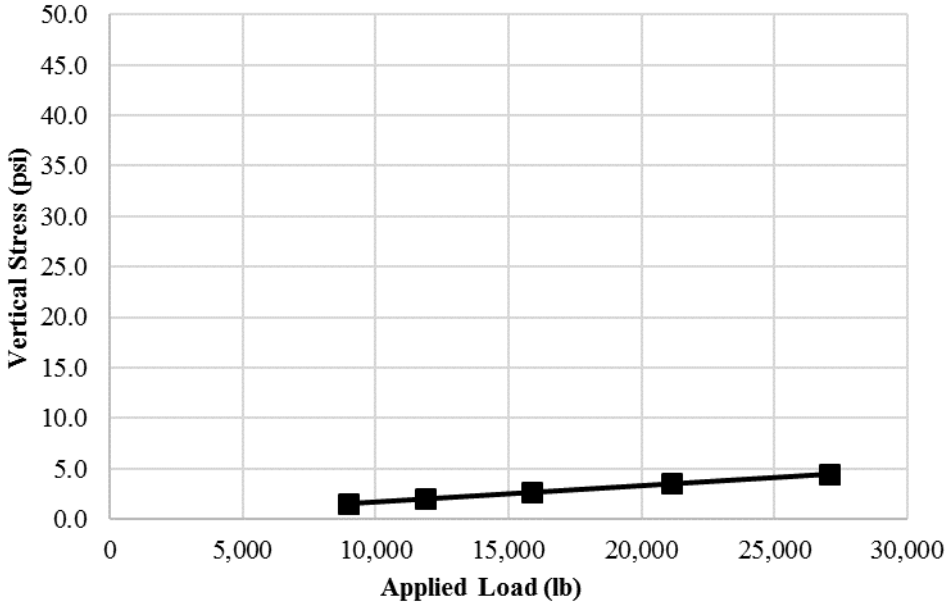

Figure 108. Graph. Vertical stress measured by TEPC3 in experiment No. 3 at different load levels.

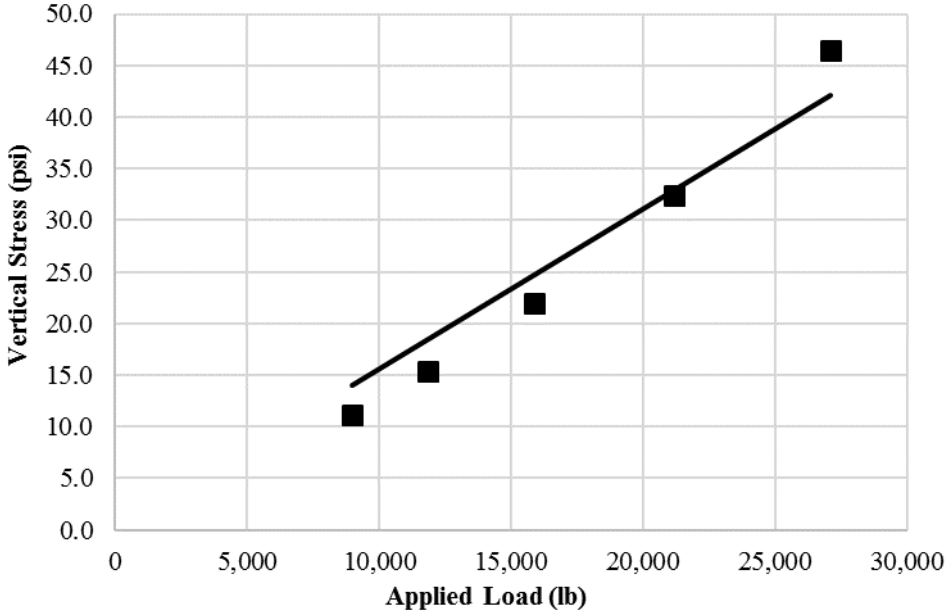

Figure 109. Graph. Vertical stress measured by TEPC5 in experiment No. 3 at different load levels.

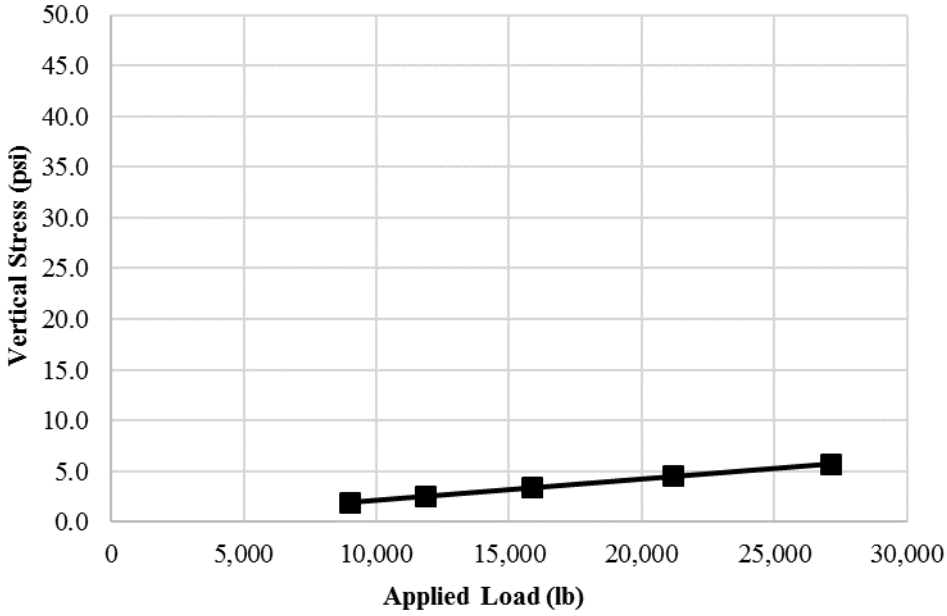

Figure 110. Graph. Vertical stress measured by TEPC6 in experiment No. 3 at different load levels.

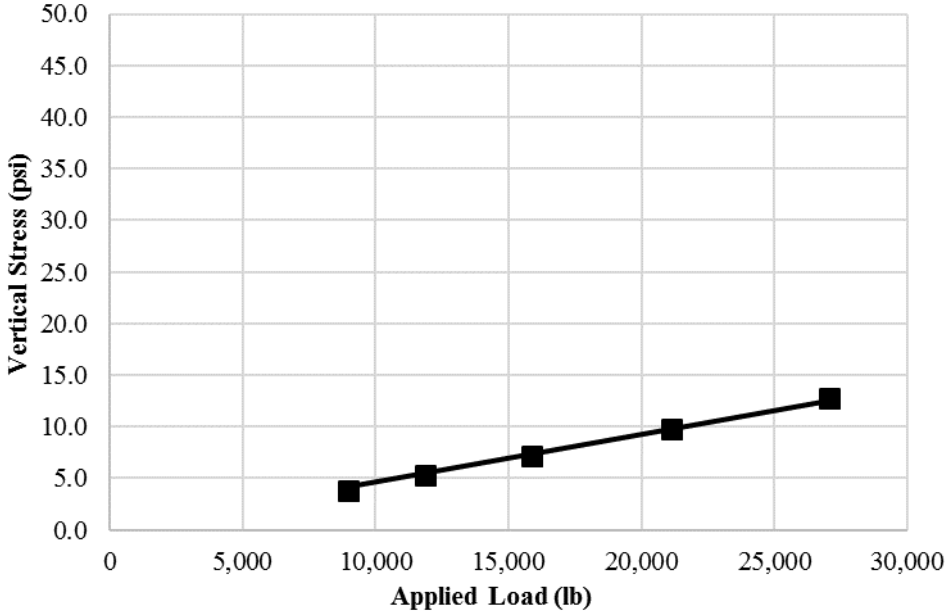

Figure 111. Graph. Vertical stress measured by TEPC9 in experiment No. 3 at different load levels.

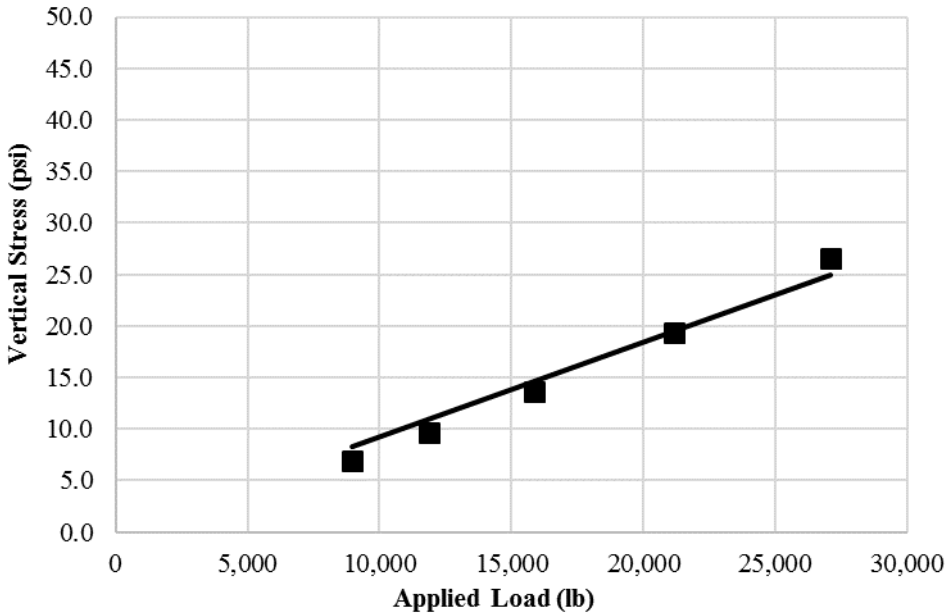

Figure 112. Graph. Vertical stress measured by TEPC10 in experiment No. 3 at different load levels.

Table 20. Vertical stress measurements in experiment No. 3 at different load levels.

Target Load Level (lb)	Average Applied Load (lb)	TEPC1 Vertical Stress (psi)	TEPC3 Vertical Stress (psi)	TEPC5 Vertical Stress (psi)	TEPC6 Vertical Stress (psi)	TEPC9 Vertical Stress (psi)	TEPC10 Vertical Stress (psi)
9,000	8,971	2.9	1.5	11.1	1.9	3.9	6.9
12,000	11,857	4.0	2.0	15.3	2.5	5.2	9.6
16,000	15,860	5.6	2.7	22.0	3.4	7.1	13.7
21,000	21,146	7.7	3.6	32.4	4.6	9.8	19.3
27,000	27,087	10.4	4.4	46.5	5.7	12.7	26.5

CHAPTER 4. OVERALL SUMMARY

In order to verify and calibrate multiple theoretical approaches as part of the FHWA project, Analysis Procedures for Evaluating Superheavy Load Movement on Flexible Pavements, a comprehensive experimental program was designed and conducted. This experimental program included five different large-scale experiments aiming to achieve the following objectives:

- Verify the soil-strength parameters (c and ϕ) as estimated by the proposed FWD-based methodology developed in this project.
- Verify the applicability of the proposed bearing capacity approach for SHL-vehicle loading.
- Investigate the influence of a sloped shoulder on edge shear failure under FWD-type and slower loading.
- Assess the influence of loading on flexible and rigid buried utilities.

In this report, the properties of the SG, CAB, and AC materials used in the experiments are elaborated on first. As part of the verification of the developed FWD-based methodology for estimating shear strength parameters of SG layer, triaxial compression tests were conducted to measure ϕ and c of the SG material used in the large-scale box.

This report also describes the large-scale box in detail, experiment preparation, instrumentation plans, and loading protocols for each of the five completed experiments. Note that the experiment instrumentation plans and loading protocols were designed to provide the required information for the calibration and verification purposes.

Finally, preprocessing steps to identify and separate the appropriate load-induced response signals from the recorded data followed by the results of preprocessed recordings measured by the load cell, LVDTs, and TEPCs during experiments No. 1, No. 2, and No. 3 are presented. It should be noted that the analyzed measurements for experiment No. 4 (i.e., sloping edge experiment) and experiment No. 5 (i.e., buried utilities experiment) are presented in detail in Volume VII: Appendix F and Volume VIII: Appendix G, respectively.[6,7]

REFERENCES

1. Hajj, E.Y., Siddharthan, R.V., Nabizadeh, H., Elfass, S., Nimeri, M., Kazemi, S.F., Batioja-Alvrez, D.D., and Piratheepan, M. (2018). *Analysis Procedures for Evaluating Superheavy Load Movement on Flexible Pavements, Volume I: Final Report*, Report No. FHWA-HRT-18-049, Federal Highway Administration, Washington, DC.

2. Nimeri, M., Nabizadeh, H., Hajj, E.Y., Siddharthan, R.V., and Elfass, S. (2018). *Analysis Procedures for Evaluating Superheavy Load Movement on Flexible Pavements, Volume III: Appendix B, Superheavy Load Configurations and Nucleus of Analysis Vehicle*, Report No. FHWA-HRT-18-051, Federal Highway Administration, Washington, DC.

3. Nabizadeh, H., Hajj, E.Y., Siddharthan, R.V., and Elfass, S. (2018). *Analysis Procedures for Evaluating Superheavy Load Movement on Flexible Pavements, Volume IV: Appendix C, Material Characterization for Superheavy Load Movement Analysis*, Report No. FHWA-HRT-18-052, Federal Highway Administration, Washington, DC.

4. Nabizadeh, H., Hajj, E.Y., Siddharthan, R.V., Nimeri, M., Elfass, S., and Piratheepan, M. (2018). *Analysis Procedures for Evaluating Superheavy Load Movement on Flexible Pavements, Volume V: Appendix D, Estimation of Subgrade Shear Strength Parameters Using Falling Weigh Deflectometer*, FHWA-HRT-18-053, Federal Highway Administration, Washington, DC.

5. Nabizadeh, H., Nimeri, M., Hajj, E.Y., Siddharthan, R.V., Elfass, S., and Piratheepan, M. (2018). *Analysis Procedures for Evaluating Superheavy Load Movement on Flexible Pavements, Volume VI: Appendix E, Ultimate and Service Limit Analyses*, Report No. FHWA-HRT-18-054, Federal Highway Administration, Washington, DC.

6. Nabizadeh, H., Siddharthan, R.V., Elfass, S., and Hajj, E.Y. (2018). *Analysis Procedures for Evaluating Superheavy Load Movement on Flexible Pavements, Volume VII: Appendix F, Failure Analysis of Sloped Pavement Shoulders*, Report No. FHWA-HRT-18-055, Federal Highway Administration, Washington, DC.

7. Nabizadeh, H., Elfass, S., Hajj, E.Y., Siddharthan, R.V., Nimeri, M., and Piratheepan, M. (2018). *Analysis Procedures for Evaluating Superheavy Load Movement on Flexible Pavements, Volume VIII: Appendix G, Risk Analysis of Buried Utilities Under Superheavy Load Vehicle Movements*, Report No. FHWA-HRT-18-056, Federal Highway Administration, Washington, DC.

8. Batioja-Alvarez, D.D., Hajj, E.Y., and Siddharthan, R.V. (2018). *Analysis Procedures for Evaluating Superheavy Load Movement on Flexible Pavements, Volume IX: Appendix H, Analysis of Cost Allocation Associated with Pavement Damage Under a Superheavy Load Vehicle Movement*, Report No. FHWA-HRT-18-057, Federal Highway Administration, Washington, DC.

9. Kazemi, S.F., Nabizadeh, H., Nimeri, M., Batioja-Alvarez, D.D., Hajj, E.Y., Siddharthan, R.V., and Hand, A.J.T. (2018). *Analysis Procedures for Evaluating Superheavy Load Movement on Flexible Pavements, Volume X: Appendix I, Analysis Package for Superheavy Load Vehicle Movement on Flexible Pavement (SuperPACK)*, Report No. FHWA-HRT-18-058, Federal Highway Administration, Washington, DC.

10. AASHTO T 11-05. (2005). *Standard Method of Test for Materials Finer Than 75-μm (No. 200) Sieve in Mineral Aggregates by Washing*. American Association of State Highway and Transportation Officials, Washington, DC.

11. AASHTO T 27-14. (2014). *Standard Method of Test for Sieve Analysis of Fine and Coarse Aggregates*. American Association of State Highway and Transportation Officials, Washington, DC.

12. AASHTO T 89-13. (2013). *Standard Method of Test for Determining the Liquid Limit of Soils*. American Association of State Highway and Transportation Officials, Washington, DC.

13. AASHTO T 90-16. (2016). *Standard Method of Test for Determining the Plastic Limit and Plasticity Index of Soils*. American Association of State Highway and Transportation Officials, Washington, DC.

14. AASHTO M 145-91. (2017). *Standard Specification for Classification of Soils and Soil-Aggregate Mixtures for Highway Construction Purposes*. American Association of State Highway and Transportation Officials, Washington, DC.

15. ASTM D2487-11. (2011). "Standard Practice for Classification of Soils for Engineering Purposes (Unified Soil Classification System)." *Book of Standards, 04.08*, ASTM International, West Conshohocken, PA.

16. AASHTO T 307-99. (2017). *Standard Method of Test for Determining the Resilient Modulus of Soils and Aggregate Materials*. American Association of State Highway and Transportation Officials, Washington, DC.

17. AASHTO T 99-17. (2017). *Standard Method of Test for Moisture-Density Relations of Soils Using a 2.5-kg (5.5-lb) Rammer and a 305-mm (12-in.) Drop*. American Association of State Highway and Transportation Officials, Washington, DC.

18. ASTM D7181-11. (2011). "Standard Test Method for Consolidated Drained Triaxial Compression Test for Soils." *Book of Standards, 04.09*, ASTM International, West Conshohocken, PA.

19. Nevada Department of Transportation. (2014). *Standard Specifications for Road and Bridge Construction*, Nevada Department of Transportation, Carson City, NV. Available online: https://www.nevadadot.com/home/showdocument?id=6916, last accessed July 6, 2018.

20. AASHTO T 2-91. (2015). *Standard Method of Test for Sampling of Aggregates*. American Association of State Highway and Transportation Officials, Washington, DC.

21. AASHTO T 248-14. (2014). *Standard Method of Test for Reducing Samples of Aggregate to Testing Size*. American Association of State Highway and Transportation Officials, Washington, DC.

22. AASHTO T 180-17. (2017). *Standard Method of Test for Moisture-Density Relations of Soils Using a 4.54-kg (10-lb) Rammer and a 457-mm (18-in.) Drop*. American Association of State Highway and Transportation Officials, Washington, DC.

23. AASHTO T 209-12. (2012). *Standard Method of Test for Theoretical Maximum Specific Gravity (Gmm) and Density of Hot-Mix Asphalt (HMA)*. American Association of State Highway and Transportation Officials, Washington, DC.

24. ASTM C39/C39M-17b. (2017). "Standard Test Method for Compressive Strength of Cylindrical Concrete Specimens." *Book of Standards, 04.02,* ASTM International, West Conshohocken, PA.

25. ASTM D1196/ D1196M-12 (2016). "Standard Test Method for Nonrepetitive Static Plate Load Tests of Soils and Flexible Pavement Components, for Use in Evaluation and Design of Airport and Highway Pavements," *Book of Standards, 04.03,* ASTM International, West Conshohocken, PA.

26. 3D-Move Analysis software V2.1. (2013). Developed by University of Nevada, Reno, NV. Available online: http://www.arc.unr.edu/Software.html#3DMove, last accessed September 19, 2017.

27. SAP2000® V18. (2016). Structural Software for Analysis and Design, Walnut Creek, CA.

HRDI-20/11-18(WEB)E